UNIVERSITY OF CALIFORNIA
RIVERSIDE

Biological Assembly and Synthesis of Inorganic Nanostructures

A Dissertation submitted in partial satisfaction
of the requirements for the degree of

Doctor of Philosophy

in

Chemical and Environmental Engineering

by

Joun Lee

December 2009

Dissertation Committee:
Dr. Nosang Vincent Myung, Chairperson
Dr. Wilfred Chen
Dr. Ashok Mulchandani
Dr. Chris Dames

The Dissertation of Joun Lee is approved:

_____

_____

_____

_____

Committee Chairperson

University of California, Riverside

To my parents

ACKNOWLEDGEMENTS

First and foremost I would like to express my gratitude to my advisors, Prof. Nosang V. Myung, Prof. Wilfred Chen and Prof. Ashok Mulchandani for their invaluable teachings on my research and also on the vision of life. I appreciate Prof. Wu, Prof. Wyman, Prof. Chris Dames, Prof. Marc Deshusses, Prof. Bongyoung Yoo, Dr. Yongwoo Rheem, Dr. Jaehong Lim, Dr. Kawai Tam for their great encouragements, supports and help. I am grateful to Adra Baca, Shawn O'Malley, Julie Farjardo, Shrisudersan Jayaraman and Ruchi Yongthonsun who I met in Corning Inc. for lightening up my life during the important period of time in my PhD program.

I would like to thank my labmates, Dr. Syed Mubeen Jawahar Hussaini, Dr. Ting Zhang, Dr. Feng Xiao, Dr. Mangesh Bangar, Dr. Carlos, Dr. Min Lai, Sandra Hernandez, Nicha Charpurayoon, Paul Chonghyun Chang, Hyunsung Jung, Fang Liu and Divya Sivaraman for all the help and supports I've received throughout my PhD program, and for the numbers of special moments we've shared for the past four years.

I would like to show my deep gratitude to Helen and Francis Park for their love and support. And lastly, I would like to show appreciation to my parents for their invaluable love which I will have to repay for the rest of my life.

And rest in peace, Jennie Yan Liu.

ABSTRACT OF THE DISSERTATION

Biological Assembly and Synthesis of Inorganic Nanostructures

by

Joun Lee

Doctor of Philosophy, Graduate Program in Chemical and Environmental Engineering
University of California, Riverside, December 2009
Dr. Nosang V. Myung, Chairperson

Science technologies have been in pursuit of smaller, faster and more efficient devices and enormous efforts made by myriad numbers of scientists have provided us with electronics in reduced volumes with improved performances. Miniaturization of electronic circuits down to micrometer scale has been well-developed as industrial processes and it is easy to witness electronic products containing integrated circuits consisted of microstructures in our everyday life. However, miniaturization of circuit components down to nanometer scale has revealed new challenges not only for difficult handling of diminutive structures but also for unusual physical properties of nanomaterials.

Countless numbers of conventional chemical and physical studies have been dedicated to exploit the benefit of the unique properties of nanostructures by developing efficient techniques for controlled synthesis and assembly of nanostructures. However,

environmental concerns of using toxic solvent systems and high energy-consuming processes, and pursuit of highly selective molecular interactions for highly precise assemblies have averted the eyes of scientists to biological materials. Biorecognition properties of biological materials are attractive for achieving programmed self-assembly of nanostructures and biomolecules with metal-reducing ability are very inviting for developments of environmentally-acceptable synthesis processes.

In the light of above discussion, this thesis takes the advantages of biological approaches to assemble and synthesize inorganic nanostructures in a controlled manner. DNA was used for the assembly processes due to their facilities of sequence programming and chemical modifications. Spatially controlled assembly of multi-segmented Au/Pd/Au nanowires across gold electrodes has been demonstrated using thiolated DNA strands functionalized on the gold surface of nanowires and electrodes. Electron transport properties of DNA-assisted assembled nanowires were demonstrated showing negligible blocking effect by DNA layers hybridized between nanowires and electrodes. The assembled Au/Pd/Au nanowire was used for hydrogen sensing manifesting the applicability of DNA-assisted assembly to build functional nanodevices.

Amino acids are essential as building blocks for proteins and for metabolisms. Recently, amino acids have been given another important role as a reducing and capping agent for the synthesis of gold nanostructures. Amino acid-mediated synthesis of gold nanostructures has been demonstrated showing the capability of biological approaches to synthesize single crystalline gold nanostructures in 0-D, 1-D and 2-D dimensions by manipulating the reaction environment. Structural changes of gold nanostructures due to

the speciation of gold complexes were systematically demonstrated by altering solvent conditions. The effect of the side chains of amino acids on the structural features of gold nanostructures was systematically demonstrated. Distinguished electron transport properties were observed for single crystalline nanoribbons showing resistivity lower by an order of magnitude than polycrystalline counterparts. Rapid reversible room temperature H_2S gas sensor was fabricated using AC aligned gold nanoparticle arrays.

TABLE OF CONTENTS

Chapter 3: Glycine-mediated Synthesis of Gold Nanostructures

Chapter 4: Amino acid - Mediated Synthesis of Gold Nanostructures

LIST OF TABLES

LIST OF FIGURES

Chapter 1: Biological Assembly and Synthesis of Gold Nanostructures

1.1 Nanomaterials and Nanostructures: An Overview

Nanotechnology is a term that includes various fields of study dealing with nanomaterials and nanostructures. Nanomaterials and nanostructures are described as the materials and architectures with at least one dimension falling in the nanometer range. Typical nanomaterials and nanostructures of different dimensions are listed in table 1.1. The interest in nanomaterials and nanostructures has elevated as part of the pursuit of miniaturization of electronic devices. However unique physical properties of nanomaterials have distinctively differentiated those from materials larger than micrometer ranges and showed that the creation of nanomaterials was not just about continuation of miniaturization.

Table 1.1 Examples of typical nanomaterials and nanostructures.

Dimension	Structures	Material	Size (approx.)
0-D	Nanoparticles Nanocrystals Nanocubes Quantum dots	Metals, semiconductors, metal oxides, carbon	Diam. <100nm
1-D	Nanowires Nanotubes Nanoribbons	Metals, semiconductors, metal oxides, carbon	Diam. <200nm
2-D	Nanoplatelets Nanosheet	Metals, carbon	Thickness <100nm
	Thin film		Thickness <1000nm

The unique properties of nanomaterials are due to the significant large ratio of surface atoms to the total number of atoms, which increases the role of surface for various

physical and chemical properties. Nanomaterials have lower melting points than bulk materials as large as 1000°C because of the significant role of surface energy in thermal stability [1]. An inert material at bulk scale, such as gold, exhibits excellent catalytic properties at low temperatures when the size of material is reduced to nanometer scale [2]. Moreover, electrical and optical properties of nanomaterials also considerably differ from their bulk counterparts. Electrical and optical properties of nanomaterials are often explained by the quantum confinement effect which describes the phenomenological results by electrons trapped in small dimensions. The behavior of electrons remains free when the confining dimension is larger compared to the wavelength of valence electrons that maintains the bandgap of the structure at its original energy due to continuous energy state. However, as the confining dimension reaches a certain limit at nanometer scale, the energy spectrum turns discrete thereby the bandgap becomes size dependent. Thus, as the sizes of nanoparticles become smaller, a blue shift can be observed in optical illumination. Electrons are confined in all three dimensions in zero-dimensional (0-D) nanomaterials such as nanoparticles and quantum dots. One-dimensional (1-D) nanomaterials such as nanowires and nanoribbons confine electrons in two dimensions, and two-dimensional (2-D) nanomaterials such as thin films and nanoplatelets confine electrons in one dimension. Most of the properties of nanomaterials described previously are dependent on the shape of nanomaterials as well as size. Electrical properties of nanomaterials are especially difficult to be explained without the definition of structural shape. However, in general, electron scattering by surfaces and grain boundaries of

nanomaterials become significant contributions to the resistivity, thereby augmenting resistivity values of nanomaterials above those of bulk materials.

Such unique properties of nanomaterials and nanostructures have been studied extensively and applied for the development of various kinds of nanodevices with improved performance. The key challenge that the current technologies have faced for the fabrication of nanodevices is the creation and arrangement of nanomaterials with precise controllability because the small dimensions that make these structures interesting also impart a new degree of difficulty in maneuverability. For the reason, a number of techniques have been developed to efficiently synthesize nanomaterials with controlled shape and size, and precisely assemble nanomaterials on specifically desired location. In this chapter, reviews on biological approaches for assembly of 1-D nanostructures and synthesis of nanostructures are summarized with brief introduction of conventional efforts towards controlled synthesis and assembly of nanomaterials.

1.2 Assembly of 1-D Nanostructures

1.2.1 Introduction

As the size of electronic devices have become smaller, the need for developing novel techniques to precisely and efficiently synthesize and assemble 1-D nanostructures has grown to encompass electronic, optical and sensor devices in nanometer scales. One-dimensional nanostructures play critical roles in various kinds of devices as electronic interconnects, waveguides and transducers. One-dimensional nanostructures have high surface-to-volume ratios, which enables much more sensitive changes on electron transport properties than those of thin films. An array of 1-D nanostructure provides unparalleled precision for nanoscale waveguides and polarizers, while also comprising the wires that address functional elements in nanodevices. To create diminutive nanodevices, rational positioning of 1-D nanostructures on programmed sites is critical in exploiting nanostructures and improving manufacturability of nanodevice. Conventional fabrication processes of nanostructures which often include both synthesis and assembly processes can be divided into two major categories, top-down and bottom-up approaches. Top-down approaches start with patterns made on a large scale and reduce its lateral dimensions before forming nanostructures. Top-down techniques is broadly composed of photolithographic methods and non-photolithographic methods. Photolithography is a mature technique that has been used for manufacturing microelectronic chips. It has accurate control on positioning patterns on specific locations; however, it has faced difficulties scaling down to sub-100nm scales due to the limitations of optical diffraction and the opacity of the materials used for making lenses or supports of photomasks. Non-

lithographic methods, such as electron-beam lithography, dip-pen lithography, scanning tunneling microscope lithography, soft lithography, can overcome the scale limitations of photolithography and scale down to 20~30nm. Recently, inkjet printing of nanomaterials has also been developed for accurate placement of nanocrystals on substrates[3-6]. However the construction of arbitrary three-dimensional objects is very challenging for these top-down approaches [7,8].

Bottom-up techniques begin with atoms or molecules to build up nanostructures, in some cases through smart use of self-organization. Bottom-up approaches are best suited for assembly and establishing short-range order at nanoscale dimensions, while top-down approaches are good for producing structures with long-range order and for making macroscopic connections. Bottom-up techniques are attractive because they are amenable to achieving assemblies of diminutive nanostructures. However precise control of the assembled structure is still a hurdle since the manipulation of nanostructure positioning is difficult at such small scales. Although there have been a number of efforts to develop physical and chemical techniques to assemble nanostructures, spatial control of such small structures is still difficult to be realized by physical or chemical approaches. Thus the interest in biomolecules, which have self-recognition properties which can realize selective "automatic positioning" of nanostructures by their natural features (ref) and along with its environmentally benign properties, has considerably emerged as a potential candidate for assembly of nanostructures. The feature of self recognition may provide more intricate control on nanostructure assemblages even on a scale that artificial features created by physical and chemical forces cannot reach. As a reflection of these interests in

bio-facilitated nanostructure organization, conventional chemical and physical approaches to assemble nanostructures were overviewed and biological assembly techniques with its experimental progresses were reviewed in detail

1.2.2 Conventional Assembly Techniques

A number of research activities have arranged nanowires in an ordered manner with different levels of hierarchy by use of microfluidics, Langmuir Blodgett films, focused laser beam, electric field and magnetic field. Recently, in situ and top-down lithographic approaches for the synthesis of 1-D nanostructures have also been demonstrated to fabricate nanowire-based devices.

Microfluidic alignment is one of the first techniques that successfully demonstrated the long range of ordered nanowire networks utilizing shear forces created by fluidic movements. Use of continuous flow, evaporating droplet, dip coating and blown bubble has been demonstrated as efficient techniques to align nanowires in large scale. Flow assembly was demonstrated by use of continuous flow of liquid in a microchannel, poly (dimethylsiloxane) (PDMS) mold, on a flat substrate[9]. The movement of meniscus due to the evaporation of a droplet was capable of aligning nanowires in uniform directionality[10] and the same principle was applied in larger sale using dip coating method[11]. A blown bubble from nanowire/epoxy suspension transferred nanowires in uniform directionality on a large surface of silicon wafers and plastic sheets with curvature[12].

Langmuir Blodgett (LB) technique is a proven and robust technique for assembling large arrays of nanowires[13]. LB technique utilizes the arrangements of amphiphilic

molecules interacting with air at air-water interface. Functionalization of the nanowire surfaces with amphiphilic molecules which are usually composed of a hydrophilic head and a hydrophobic tail enables arrangements of nanowires to the water-air interface because of the favorable partition of hydrophobic tail to air and hydrophilic head to water. According to the level of pressure applied to the surfaces, which changes the directional capillary forces and van der Waals forces on the surfaces, the nanowires would be aligned isotropically side-by-side, forming nano-rafts. Transfer of aligned nanowires on the surface of water onto a substrate creates parallel arrays of nanowire in large scale.

A method to achieve fine manipulation of a single nanowire in fluid environment has been studied by the use of optical trapping. Optical manipulation of inorganic material uses a focused laser beam to trap, transfer and assemble individual nanowires[14]. Individual nanowires can be aligned in fluid environment by picking up, moving and positioning nanowires using a single-beam optical trap. Nanowires trapped in the optical trap can be assembled on a substrate with high precision with the single laser. Optical manipulation has great potential for fabricating a single nanowire device with high precision however the concurrent operating of tens or hundreds of lasers is required to achieve the alignment.

Use of alternating electrical field to polarize and assemble nanostructures between pre determined pads was first demonstrated by Mallouk and coworkers[15]. The alignment of nanowires within an electric field, which creates dielectrophoretic force on the nanowire

in the direction of the electric field, is dependent on its polarization within the surrounding dielectric medium. The induced dipoles align the nanowires parallel to the electric field while the localized coulombic attractive forces are simultaneously created between adjacent nanowires by the induced dipoles, resulting in the formation of chained or branched interactions among the nanowires. Pre-aligned nanowires positioned on the top of electrodes experience an enhanced electric field, thereby forming branched structures by attracting other nanowires in solution along the radial direction. Selective alignment of nanowires directed to microwells was also demonstrated by Keating's group by creating programmed and spatially confined electric field[16].

In a similar principle to electric field-assisted alignment, magnetic field has great potential to create nanowire arrays with controlled directionality. Magnetically polarized nanowires can be manipulated with external magnetic fields, ferromagnetic substrates and neighboring magnetic nanowires. Magnetic interactions as a meaning of nanowire manipulation were first investigated by Tanase and coworkers[17]. They demonstrated the proportional increase in the velocity of the end-to-end nanowire alignment according to the increase of attractive forces and according to the decrease of the viscous drag in solution. They have later demonstrated an entrapment of a multi-segmented Pt/Ni/Pt nanowire between two Ni pads by an exposure of the system to a 10G magnetic field. Myung's group demonstrated individually addressable magnetic alignment of multi-segmented Ni/Bi/Ni and Ni/Au/Ni nanowires by applying a low external magnetic field of 200 Oe. They also demonstrated the angular manipulation from 45° to 135° on Ni

electrodes and the high-density arrays achieved with multiple alignments of a dilute suspension [18,19].

Controlled growth of a single nanowire between microfabricated electrodes was electrochemically demonstrated by Myung's group as an effort to fabricate single-nanowire-based nanodevices[20]. Lithographically patterned nanowire electrodeposition (LPNE) can create inorganic nanoribbons with extremely high surface to volume ratio in controlled shape and sizes which is an ideal technique if the morphology of electrodeposited nanoribbon can be improved[21].

Physical or chemical strategies for the nanowire alignment introduced above have received considerable attention. However, lack of spatial manipulation and individual addressability of nanowires, limited material selection and high investment costs have restricted the application of these methods. To overcome the limitations of previous assembly techniques, biomaterials have been in the limelight due to their biospecific recognition properties, low costs of synthesis, and facility to functionalize on inorganic materials.

1.2.3 Biological Assembly Techniques

As the scale of device systems has decreased down to nanometer ranges, conventional fabrication processes have faced technical difficulties to precisely assemble 1-D nanostructures on programmed sites while achieving fast assembly rates. As discussed previously, conventional techniques can provide precise positioning of 1-D nanostructures or fast rate of assembly; however, none of the conventional techniques can

satisfy both of the prerequisites. Thus, to achieve a fast programmable assembly for the fabrication processes of nanometer scale device systems, biorecognition systems has been recognized as having great potential to realize “rapid automatic positioning” of 1-D nanostructures. Biomolecules with biorecognition properties have specific non-covalent interaction, such as hydrogen bonds, electrostatic bonds, Van der Waals forces and hydrophobic bonds, between a pair of complementary bioconjugates which is enabled by the shape of proteins or the sequence of nucleic acids for selective binding. Binding reactions of bioconjugates are by their nature reversible since the reaction occurs via non-covalent bonds, which is also addressed as one of the advantages of using biological approaches. Here, various kinds of methodologies for biological assembly are summarized based on the enabling biomaterial.

1.2.3.1 Deoxyribonucleic acid (DNA) Hybridization

DNA has been one of the most frequently used biomaterials for assembling various kinds of nanostructures because of its highly selective biorecognition properties and the relatively easier, cheaper methodologies to synthesize and modify DNA. Assembly of nanowires on a planar gold surface with a DNA biorecognition system was first demonstrated by Jeremiah and coworkers[22]. They used a pair of complementary single stranded DNAs (ssDNA) modified with thiol tags to functionalize gold surfaces of nanowires and substrates with DNA. Functionalization and hybridization efficiencies were systematically demonstrated by varying the features of DNA strands and experimental conditions, which ascribe the improvement of oriented ssDNA adsorption to gold-thiol linkages and the increase in hybridization efficiency to longer ssDNA with

repeat base sequences and to a mercaptohexanol (MCH) treatment that prevents interactions between adsorbed ssDNA and gold surfaces. Site-specific functionalization of ssDNA on nanowires was also demonstrated for controlled end-to-end assembly of nanowires. Localized DNA-functionalization on the tips of gold nanowires and on the gold segments of Au/Pt/Au multi-segmented nanowires was confirmed by hybridizing rhodamine labeled complementary ssDNA that fluoresced only at the tips and the gold segments.

Stoermer and Keating demonstrated a similar study for DNA-directed assembly of nanowires on a glass substrate instead of gold surface [23]. In this study, avidin-biotin linkages were used to functionalize ssDNA to the surface of glass substrates and nanowires. For the functionalization of ssDNA on glass substrates, NeutrAvidin was silanized on the surface of glass substrate and provided linkages for ssDNA modified with biotin. Similarly, electrochemically grown Au and Au/Ag/Au nanowires were coated with NeutrAvidin and then functionalized with complementary ssDNA through avidin/biotin interaction. The authors elucidated competitive attachments of nanowires with different base pairs and concluded that 5.6% of nanowires were attached on glass substrates via non-specific binding which was similar to those for attachments on gold. Successful use of glass substrates for DNA-directed assembly shows possibilities of constructing circuitry directly on oxidized silicon wafers without any top-down techniques.

Hazani and coworkers demonstrated self assembly of single walled carbon nanotubes (SWNT) via DNA hybridization and electrically characterized the assembled SWNTs[24]. SWNTs were aligned across two gold electrodes by hybridization of complementary ssDNA functionalized on gold electrodes and SWNTs. Compared to non-complementary alignment of SWNTs, the currents flowing through SWNTs, which were aligned via complementary DNA hybridization, increased more than an order of magnitude. This study corroborates double-stranded DNA (dsDNA) control over the electron transport properties of SWNT-based device. Extensive studies on SWNT-based field effect transistors (FET) also verified the feasibility of DNA-mediated assembly for SWNT alignment[25]. So far, functionalization processes of ssDNA on carbon nanotubes have been demonstrated in two different ways: wrapping of ssDNA on SWNT[26,27] and conjugation of carboxyl groups on SWNT to amine groups on ssDNA via carbodiimide mediated amidations[24,28].

1.2.3.2 Antibody/Antigen, Avidin/Biotin and Protein Interaction

Other than DNA hybridization, antibody/antigen and avidin/biotin interaction have also been used to demonstrate end-to-end assembly of nanowires. End-to-end assemblies of nanowires were reported by Tan's and Searson's group using anti-mouse/mouse antibody (IgG)[29] and avidin/biotin[30] as linker molecules to form nanowire chains. Tan's group utilized preferential micellar binding of cetyltrimethylammonium bromide (CTAB) on {100} longitudinal side surface of gold nanorods, thereby controlled thioctic acid (TA) attachments on the tips of nanorods which was connected to anti-mouse IgG through carbodiimide mediated amidations. Anti-mouse IgG modified nanorods were

able to form nanowires chains by employing mouse IgG in the solution. Similarly, Searson's group used palmitic acid to passivate the surface of nickel segments, which selectively binds to native oxide on nickel allowing Biotin and Avidin to be functionalized only on the tips of Au/Ni/Au nanowires. Based on their results, the length of nanowire chain increased as a function of time in a mixture of biotin-terminated and avidin-terminated nanowires.

Wang and coworkers demonstrated assembly of cadmium telluride nanowires using bovine serum albumin (BSA)/anti-BSA IgG and avidin/biotin as connectors to bridge nanowires. They found that crossbar and side-to-end connections were dominant assembly fashions. Oppositely, utilizing the fact that the histidine tags bind tightly onto Ni surfaces, selective functionalization of elastin-like-polypeptides (ELP) on Ni segments of Ni/Au/Ni multi-segmented nanowires and on a specific area on Ni electrodes was demonstrated by Wang and coworkers[31]. Successful site-specific assembly of Ni/Au/Ni nanowires on a Ni electrode with controlled directionality was also shown by an applied magnetic field.

1.2.4 Experimental Progress in Biological Assembly Techniques

The studies on biological assembly of 1-D nanostructures have been inspired by the techniques developed for biological assembly of 0-D nanostructures. Staring from a confirmation of the feasibility of DNA as a linker by studying the assembly of gold nanowires on gold surfaces[22], biological assembly of nanowires have been developed in a way to accomplish crossover and end-to-side and end-to-end assembly of 1-D

nanostructures for automatic assembly of circuitry in various complexity. Generally, biological assembly protocol consists of three processes: functionalization of 1-D nanostructures with biomolecules, functionalization of complementary biomolecules on substrates and hybridization of 1-D nanostructures on substrates. To accomplish programmed self assembly of 1-D nanostructures into nanodevices, precise control over the process of biofunctionalizing 1-D nanostructures and substrates is critical. There have been three different ways to site-specifically functionalize nanowires using 1) preferential molecular bindings on the circumferential surface leaving only the tips of nanowires available for biofunctionalization[29], 2) pre-functionalization on the tips of electrochemically-grown nanowires embedded in an alumina template before dissolving alumina[22], and 3) multi-segmented nanowires, which contain two segments for selective binding to the modified functional group on biomolecules[22,32].

Biofunctionalization processes have been demonstrated on gold and glass substrates[22] using thiol-modified ssDNA and NeutrAvidin[23], respectively. Site-specific functionalization on substrates would be ideal to assemble many different elements on a single substrate. However, in the case of 1-D nanostructure alignment to create interconnects, the studies on DNA-directed assembly of SWNTs showed successful alignment of SWNT across two gold electrodes, which were entirely functionalized with ssDNA implicating another way of controlling self assembly by using appropriate configuration of substrates. The hybridization process has generally been carried out in a freestanding solution containing two components functionalized with complementary biomolecules. Although selective binding of nanowires via interactions of

complementary biomolecules have been demonstrated in a few studies[22,23], the directionality of assembled nanowires is not typically addressed. One isolated report by Wang and coworkers employed magnetic field assistance to control the directionality of nickel nanowires during the process of assembly[31]. Application of a magnetic field to the suspension of ELP functionalized nickel nanowires allowed the nanowires to be assembled in a single direction across two nickel electrodes.

So far, DNA has been predominantly used to demonstrate biological assembly of various kinds of nanostructures including 1-D nanostructures. Although the techniques using antigen/antibody, avidin/biotin or bioengineered polypeptides promise assembly with high spatial manipulation, there have been concerns about achieving self-addressable assembly and the poor conductivity of biomaterials placed between nanostructures. DNA has high biospecific recognition behavior due to its base-pairing and this property provides further potential for simultaneous assembly of contrasting nanowires by designing different base sequences for each nanowire composition. The problem of the insulating nature of the crossover points should be seriously considered when contemplating the prospects of biological assembly of electronic circuits. The tunneling barrier can be reduced when DNA oligomers are used as nanowire connectors, resulting in a smaller effective separation between them as compared to proteins[24,33]. In fact, the improvements of electron transport properties have been reported for SWNTs assembled through DNA hybridization[26]; however the effect of a layer of dsDNA in a crossover junction of low-resistance inorganic nanowires has not been demonstrated yet.

There are still several protracted challenges that have hindered maturation of programmed biological assembly of 1-D nanostructures. Efficient spatial and directional control of the assembled 1-D nanostructures has to be presented to truly realize an “automatic assembly” of nanodevices. Additionally, the effect of biomolecules on electron transport properties and the functionality of biologically assembled 1-D nanostructures as nanodevices must be validated for further applications of biological assembly techniques to fabricate nanodevices with increased complexity.

1.3 Synthesis of Gold Nanomaterials

1.3.1 Introduction

The first scientific approach to synthesize nanomaterials was reported by Faraday in 1857. He synthesized colloidal gold by reduction of gold chloride using phosphorus and investigated optical properties of colloidal gold prepared as thin film and as aqueous suspension[34]. In spite of the early discovery of colloidal gold, in which the size of nanoparticles was less than 100nm, limitations in observation techniques have postponed extensive studies until the microscopic technologies improved to visualize nanoscale materials. Therefore, interests on the synthesis of nanomaterials have dramatically increased in the past decades because of the development of various new techniques for characterization and manipulation available for nanomaterials.

Since the first chemical approaches made by Faraday to develop colloidal gold, chemical and physical approaches have led nanotechnology in developments of synthesis techniques to create gold nanomaterials in controlled shape and size with desired features. Current studies in nanotechnology categorize fabrication techniques for nanomaterials into top-down and bottom-up approaches. Top-down approaches predominately utilize photolithography to transfer pre-designed patterns onto substrate followed by deposition of inorganic materials. Gold is one of the most frequently used materials to fabricate lithographical patterns for use as electrodes. Even though, state-of-the-art lithographic patterning methods are able to pattern sub-100 nm features using UV light sources, they require clean environments with very complex and expensive equipments with high-energy consumption. Alternative top down methods, such as

electron-beam lithography, dip-pen lithography, scanning tunneling microscope lithography, soft lithography, can overcome the scale limitations of photolithography and scale down to 20~30nm. However, the structures prepared by top down approaches lack precise control over morphological features and contain significantly amount of impurities and structural defects. Moreover, when the target size of the structure falls into a few nanometer range, the tools currently available for top-down approaches have not been established.

Bottom-up approaches are typical wet chemical synthetic techniques, which have been used in industries for more than a century. Typical synthesis methods build gold nanostructures by homogeneous or heterogeneous growth of crystals in liquid phase for large-scale productions of well-defined nanostructures. Bottom-up approaches can provide structures with more pristine compositions and higher crystallinity at lower cost of operations than top-down approaches. The syntheses of gold nanomaterials have been successfully demonstrated by chemical, hydrothermal, and photochemical syntheses using chemical reducing agents, and UV lights as electron sources to reduce gold ions. Electrochemical synthesis has also been widely studied to create thin films on conductive surface and nanowires grown in templates. Employment of sonic and micro waves in chemical synthesis process has been studied to create gold nanomaterials with improved uniformity. Regardless of the advantages of chemical approaches for the synthesis of gold nanomaterials, environmental concerns on the toxic solvent systems and high temperature operating conditions have increased the need of alternative non-toxic synthesis methods with lower energy consumption and minimal equipment costs.

Biological approaches to synthesize gold nanomaterials have received significant attention recently due to non-toxic solvent systems with reactions occurring at ambient conditions. In the same manner as chemical methods, biological synthesis has been employed to successfully create gold nanostructures with a barrage of geometries. Many studies have biosynthesized gold nanostructures using a single biological entity and manipulation of a few reaction conditions to vary shape. Here, synthetic methods for gold nanomaterials are summarized, with respect to particle structure, based on detailed analysis of experimental conditions.

1.3.2 Conventional Synthesis Techniques

Methodologies to synthesize various kinds of gold nanostructures have been widely studied and developed for electrochemical and chemical means. Electrochemical techniques are widely used to create thin films on conductive substrates and to synthesize nanowires through a template such as porous aluminum oxide membranes[35-37]. Electrochemical techniques are capable of creating gold nanostructures with controlled shapes, sizes, and purity. However, templates with well-defined porous structures are essential for electrochemical synthesis and preparation of working electrodes would not be facile with soft templates. Wet chemical syntheses of gold nanostructures have been studied in myriads of ways to create various kinds of 0-, 1-, and 2-D nanostructures.

The solvent system of wet chemical synthesis is generally consisted of three components: reducing agent, capping agent and assistance of physical force. The reducing agent is an electron donor, which oxidizes and provides electrons to reduce gold

ions. Sodium borohydride[38], sodium citrate[39], hydrazine[40,41], amines[42-45], alcohols[46] and polymers[47] have been used for reduction of gold ions in various kinds of methods. A few studies demonstrated methods using UV-irradiation[48], γ-irradiation[49,50] and heat[51,52] for reduction of gold ions instead of chemical reducing agents.

Capping agents bind to specific orientations of nanocrystals and direct the growth of crystals into certain orientations where the capping agent is not adsorbed, thereby determining the structure of products. Alkanethiols[38,53], alkylamines[42-45,54] and polymers[47,55,56] have been used as capping agents in many studies. Many studies reported use of separate reducing and capping agent for the synthesis process, however single chemicals that can perform both tasks of reducing and capping agent have been reported frequently in the case of amines[42-45] and polymers[47]. Surfactants are also reported as effective materials to control the shape of gold nanostructures during the synthesis process[40,51].

Assistance of physical forces can be described as an additional variable that significantly affects the synthesis process. So far, use of sonicwave[57,58], microwave[59,60], and UV-irradiation[61,62] have been reported as an effective outsource to improve the morphology and monodispersity of synthesized gold nanostructures. Such physical assistance changes the reduction chemistry in the solvent system, consequently redirecting the reduction process to generate morphological changes in the products. The addition of seeds to promote controlled growth of gold nanostructures is also a well known technique to synthesize uniform structures.

So far, numerous kinds of gold nanostructures have been synthesized through chemical approaches by many different combinations of reducing, capping agents and physical assistance methods. Zero-dimensional gold nanostructures are the most widely studied structures since the history of colloidal gold synthesis has been the longest amongst any kinds of nanomaterials. The gold nanostructures that have been synthesized by chemical synthetic techniques can be listed as 0-D nanostructures, such as spherical nanoparticles, faceted nanoparticles, nanocubes and nanorings, 1-D gold nanostructures, such as nanowires[63-66], nanoribbons[67,68] and nanotubes[69], and 2-D gold nanostructures which are mostly in shape of nanoplatelets[70,71]. Amongst such diversity in structure, interestingly, the studies on gold nanowires and nanoribbons often report the crystallinity of synthesized structures as single crystalline grown along {111} orientation, especially in the case of nanoribbons. Similarly, chemically synthesized gold nanoplatelets are hexagonal and triangular with single crystalline structures oriented along {111} planes. Recently, such single crystalline nanostructures have been recognized for its improved electrical properties in nanometer scales compared to polycrystalline nanostructures[66]. However, increasing environmental concerns on toxic and high-energy-consuming synthesis methodologies promoted development of environmentally acceptable synthetic techniques, which can create various kinds of nanostructures in the same fashion as chemical approaches. Biological materials have been studied as one of the best candidates for environmentally acceptable synthetic techniques and the capability of biological materials as reducing and capping agent to synthesize various kinds of gold nanostructures has been ascribed in a number of studies. Therefore, an overview on the

biological approaches to synthesize gold nanostructures has been presented with respect to nanostructure dimensionality.

1.3.3 Biological Synthesis Techniques

1.3.3.1 Zero Dimensional Nanostructures– Nanoparticles

Biosynthesis of gold nanoparticles has been studied most frequently among the various kinds of nanostructures. The largest entities that has been used for the synthesis of gold nanoparticles are plants. The studies on *Alfalfa*[72] and *Sesbania drummondii*[73] have demonstrated *in vitro* growth of seedlings in media containing gold chloride. Transmission electron microscopic analysis on the roots and shoots of the plants showed gold nanoparticles smaller than 20nm loaded inside the cells, which is attributed to intracellular reduction of gold. Extracellular synthesis of spherical nanoparticles was demonstrated by using ground stems of *Avena sativa*[74], extracts of the leaves of lemongrass (*Cymbopagon flexuosus*)[75], and *Aloe vera*[76] whereas decahedral, icosahedral and rod-shaped nanoparticles were synthesized by using the extract of *Pelagonium graveolens*[77] incubated with gold chloride solutions. The extracts of alga (*Chlorella vulgaris*[78]) and marine alga (*Sargassum wightii*[79], *Sargassum sp.*[80]) in gold chloride solutions also showed the capability of gold reduction into spherical nanoparticles under ambient conditions.

Various kinds of fungus and bacteria have been used for the synthesis of gold nanoparticles. The use of fungus (*Verticillium sp*[81].) and bacteria (*Shewanella algae*[82], *Rhodococcus sp.*[83]) for intracellular synthesis of gold nanoparticles lead to extracellular

synthesis demonstrating the role of biomass for bioreduction. Gold nanoparticles prepared by extracellular synthesis of fungus (*Colletotrichum sp.*[77], *Trichothecium sp.*[84], *Fusarium oxysporum*[85], and *Aspergillius niger*[86]) exhibited a variety of shapes, such as triangular, hexagonal and spherical shape of gold nanoparticles, whereas spherical nanoparticles were dominant products in the intracellular synthesis using *Trichothecium sp.*[84] and *Verticillium sp.*[81]. Bacteria, *Escherichia coli*[87], incubated in gold chloride solution exhibited triangular, hexagonal and spherical nanoparticles on the surface of themselves whereas spherical nanoparticles were synthesized by cell free extracts of bacteria, *Rhodopseudomonas capsulata*[88] and *Pseudomonas aeruginosa*[89]. The study on extracellular synthesis of nanoparticles by *Rhodopseudomonas capsulata*[90] proposed an enzymatic metal reduction process by NADH-dependant reductase as a mechanism of bioreduction.

The research using biological elemental units, such as proteins, peptides and amino acids, have been carried out in a parallel approach to the trend of studies using larger bioorganisms to develop environmentally acceptable methods to synthesize gold nanoparticles. The reducing capability of proteins[91], peptides[92] and amino acids[93-96] were confirmed in a few studies where spherical nanoparticles were synthesized after incubation in gold chloride solutions. Among twenty amino acids, arginine, aspartate, lysine, tyrosine and tryptophan have been reported to synthesize gold nanoparticles.

Successful demonstration of intracellular and extracellular synthesis of gold nanoparticles corroborates the role of biomaterials as a reducing and capping agent in the

synthesis process. It has been observed that spherical nanoparticles were synthesized by intracellular bioreduction. Extracellular synthesis processes observed both spherical and faceted nanoparticles. Various kinds of bioorganisms were used to synthesize gold nanoparticles. However the use of biological compounds such as proteins, peptides and amino acids were also capable of synthesizing gold nanoparticles.

Table 1.2 Experimental conditions for biological synthesis of 0-D gold nanostructures.

Biological entity		Gold salt	pH	Temp	Use of physical force	Shape	Size	Ref
Plant	Lemongrass (Cymbopagon flexuosus)	$HAuCl_4$	-	RT	-	Nanoparticles	-	97
	Avena sativa	$KAuCl_4$	2 ~6	-	Agitation	Nanoparticles	-	98
	Alfalfa	$KAuCl_4$	5.8	RT (25/18C)	-	Nanoparticles	2~20nm	99
	Sesbania drummondii	$KAuCl_4$	4.8	25~28	-	Nanoparticles	6~20nm	100
	Aloe vera	$HAuCl_4$	-	RT	-	Spherical nanoparticles Aggregated nanoparticles	- -	101
	Pelagonium graveolens	$HAuCl_4$	-	25~27	Shaking at 200rpm	Decahedral, icosahedral and rod-shaped nanoparticles	20~40nm	102
Alga	Chlorella vulgaris	$HAuCl_4$	-	RT	-	Spherical nanoparticles	-	103
Marine alga (seaweed)	Sargassum wightii	$HAuCl_4$	-	RT	Stirring	Spherical nanoparticles	8~12nm	104
	Sargassum sp.	$HAuCl_4$	1~13	RT~250	Vigorous stirring	Particles	-	105

Table 1.2 Experimental conditions for biological synthesis of 0-D gold nanostructures (continue).

Biological entity		Gold salt	pH	Temp	Use of physical force	Shape	Size	Ref
Mushroom	Volvariella volvacea	$HAuCl_4$	-	RT~80	-	Spherical nanoparticles Dendrite/fractal structured nanoparticles	~25nm	106
Fungus	Colletotrichum sp	$HAuCl_4$	-	25~27	Shaking at 200rpm	Spherical nanoparticles	8~40nm	107
	Trichothecium sp.	$HAuCl_4$	-	27	- Shaking at 200rpm	Trianglular and hexagonal, spherical and rod-shaped nanoparticles Spherical nanoparticles	5~200nm 10~25nm	108
	Verticillium sp.	$HAuCl_4$	-	28	Shaking at 200rpm	Spherical (a few triangular and hexagonal) nanoparticles	20+8nm	109
	Fusarium oxysporum	$HAuCl_4$	-	-	Extracellular	Spherical and triangular nanoparticles	8~40nm	110
	Aspergillius niger	$HAuCl_4$	3~10	4~100	Shaking at 120rpm and stirring	Spherical, triangular nanoparticles and nanoagglomerates	-	111
Bacteria	cell free extract of R. Capsulata	$HAuCl_4$	6	30	-	Nanoparticle	10~20nm	112
	Escherichia coli	$HAuCl_4$	-	RT	-	triangular, hexagonal and spherical nanoparticles	25+8nm	113
	Rhodopseudomonas capsulata	$HAuCl_4$	4~7	RT	-	Nanoparticles	10~20nm	114
	Shewanella algae	$HAuCl_4$ / bicabonate buffer (H_2-CO_2)	7	25	Anaerobic condition	Nanoparticles	10~20nm	115
	Pseudomonas aeruginosa	$HAuCl_4$	-	37	-	Nanoparticles	15~30nm	116

Table 1.2 Experimental conditions for biological synthesis of 0-D gold nanostructures (continue).

Biological entity		Gold salt	pH	Temp	Use of physical force	Shape	Size	Ref
Protein		$AuCl_3$	Acidic	RT	-	Nanoparticles (faceted)	-	[117]
Peptide		$HAuCl_4$ in HEPES buffer	7.2		-	Nanoparticle	11.4~13.8nm	[118]
Amino acid	Tryptophan	$HAuCl_4$	-	RT	Mild stirring	Spherical nanoparticles	60+5	[119]
	Lysine						6+2	
	Arginine						10+5	
	Tyrosine					Spherical and rod-shaped nanoparticles	-	
	Aspartate	$HAuCl_4$	-	RT	-	Nanoparticles	-	[120]
	L-tyrosine	$KAuBr_4$	10.7	RT	-	Spherical nanoparticles	0.7~1.5, 5~40nm	[121]
	Glycyl-L-tyrosine						5~30nm	
	L-arginine					Anisotropic nanoparticles	~50nm	
	Aspartate	$HAuCl_4$	-	100	Boiling	Spherical nanoparticles	24+3nm	[122]

1.3.3.2 One Dimensional Nanostructures – Nanoribbons/Nanowires

Unlike the extensive studies on biosyntheses of 0-D and 2-D gold nanostructures which have been studied for the past decade, much less reports have been made on biosynthesis of 1D gold nanostructures due to a very recent development with methods. Biosynthesis of gold nanowires was first reported by two groups almost simultaneously using cell free extract of bacteria, *R. Capsulata*[88], and amino acid, aspartate[94], as a reducing agent. Both of the methods have incubated the mixture of $HAuCl_4$ and biomaterials near ambient conditions without any additives. TEM analysis on the synthesized nanowires showed that the nanowires synthesized from both of the biomaterials were polycrystalline. Bonding regions of neighboring nanoparticles in the nanowires were also observed in common which supports the mechanism of nanoparticles fusing into one another in a specific orientation and forming nanowires. Proteins existing in the cell free extract of *R. Capsulata*[88] was assumed to have reducing and capping ability of gold which might be the reason of having similar structures synthesized by using aspartate, one of the constituents of proteins. In fact, Polavarapu and coworkers have demonstrated the role of amino acid as a capping agent by adding glutamate in a nanoparticle synthesis process using sodium borohydride as a reducing agent[123]. In the presence of significant amounts of glutamate, nanoparticles synthesized in the beginning of the reaction formed chains of nanoparticles in which the particles were fusing into one another to become continuous wires.

Tan and coworkers, who have demonstrated shape controlled synthesis of gold nanostructures using aspartate, observed nanowires and nanoribbons presented in the

same network. However, in contrast to the polycrystalline nature of the nanowire, nanoribbons were single crystalline grown along {111} faces with a rectangular cross-section. A careful HRTEM observation on the indentation of a nanoribbon indicated crystal growth by oriented attachments, attributing the formation of single crystalline nanoribbon to fusion of nanocrystals into high crystallinity[94]. Gold nanoribbons synthesized by using cysteine[124] also showed the same feature of having single crystallinity along {111} planes with indented structures on the side of the nanoribbons. The same sequence of formation starting from nanoparticles, nanoparticle chains to nanoribbons was observed by a time dependent studies on the synthesis process.

The results presented in the previous studies share a few common features. Firstly, the biomolecules can function not only as a reducing agent but also as a capping agent for shape-directing gold nanoparticles into a chain structure. Secondly, nanowires are formed as a result of oriented attachments of nanoparticles and the fusion of nanocrystals in the nanowires results in the formation of nanoribbons. Lastly, nanowires with circular cross-section appear to be polycrystalline due to distorted orientations and incomplete fusion of attached nanoparticles; however nanoribbons with rectangular cross-section are single crystalline with {111} oriented planes indicating complete fusion of nanocrystals into a single orientation.

Table 1.3 Experimental conditions for biological synthesis of 1-D gold nanostructures

Biological entity		Gold salt	pH	Temp	Use of physical force	Shape	Size	Crystallinity	Orientation	Ref
Bacteria	R. Capsulata	$HAuCl_4$	6	30	-	Nanoparticle	10~20nm	-	-	112
						Nanowire	Diameter 50~60nm	Poly	-	
Amino acid	Aspartate	$HAuCl_4$	-	RT	-	Nanowire	-	Poly	-	120
						Nanoribbon	-	Single	{111}	
	Cysteine	$HAuCl_4$	-	RT	Stirring for 30min	Nanoribbons	Width 20~45nm	Single	{111}	124

1.3.3.3 Two Dimensional Nanostructures – Nanoplatelets

A few research groups have reported gold nanoplatelets synthesized as a result of bioreduction. The first observation of gold nanoplatelets in a biosynthesis process was made by Brown and coworkers using proteins with specific polypeptide sequences secreted by *Escherichia coli*[91]. They have showed the results of crystal formation with varied pH, sequence of polypeptides and specific binding properties of proteins on {111} planes. Based on the results, they elucidated the formation of thermodynamically unfavored hexagonal crystals with one pair of large (111) faces is due to the proteins biasing the growth of crystal allowing a continuous accretion onto energetically favorable faces rather than the hindrance of growth on {111} planes due to the bindings of proteins on {111} planes. Gold nanoplatelets were generally synthesized as a mixture of nanoplatelets and nanoparticles. The products consisted of less than 4% of nanoplatelets and the rest of the structures were spherical nanoparticle.

Sastry's group has significantly increased the yield of nanoplatelets up to 45% in their products by using the extracts of leaves from lemongrass (*Cymbopagon flexuosus*)[75], Tamarind[125] and *Aloe vera*[76]. Similarly to Brown's results, synthesized nanoplatelets were single crystalline with disregard to the shapes and sizes of platelets, and they were face centered cubic (fcc) structures grown along {111} planes. Detailed time dependent studies on the formation of nanoplatelet showed the growth of nanoplatelets started from aggregates of nanoparticles sintering into rudimentary triangular structures, triangular platelet with corrugated edges and single crystalline platelet with sharp edges. Characterizations on the extracts of leaves and synthesized gold nanoplatelets by Fourier

transform infrared spectroscopy (FTIR) have confirmed the existence of aldehydic or ketonic components in the extract of lemongrass[75] and *aloe vera*[76] which were assumed as the possible reason of bioreduction. However, the same approaches on Tamarind extract showed an existence of tartaric acid but no aldehydic or ketonic components[125]. IV characteristics were studied for the nanoplatelets synthesized by using lemon grass and tamarind, and a vapor sensing application for organic solvents such as acetone, benzene and methanol was demonstrated with nanoplatelets prepared by the extract of tamarind leaves.

Lee and coworkers have studied various kinds of biological entities such as algae, seaweeds, fungus and amino acids for the synthesis of gold nanoplatelets. Efforts were made to develop a biosynthesis process to achieve high yield of single crystalline gold nanoplatelets. In the process using seaweed (*Sargassum sp.*)[80], the optimization of reaction conditions allowed the yield of gold nanoplatelets to increase up to 90%. In this study, they have implicated proteins as the active species involved with the bioreduction process. More detailed studies on the effect of protein were demonstrated in a biosynthesis process using alga, *Chlorella vulgaris*[78]. A protein, which was named as the gold shape-directing protein (GSP), was identified to have a role as a reducing and capping agent. GSP was isolated from the extract of *Chlorella vulgaris* by reversed-phase high performance liquid chromatography (RP-HPLC) and then confirmed to synthesize single crystalline gold nanoplatelets in high yield (~90%) by itself. They have explicated the nanoplatelet formation with surface wrapping mechanism by GSP in which GSP wraps on the surface of triangular-shaped seeds and directs the growths of layers on the

edges of the structures. Enzymatic process was also reported to play a role as bioreductant to form gold nanoplatelets in a biosynthesis process using fungus, *Aspergillius niger*[86]. Interestingly, spiral nanoplatelets in hexagonal geometry were synthesized as well as regular nanoplatelets. The nanoplatelets synthesized by *Sargassum sp.*, *Chlorella vulgaris* and *Aspergillius niger* were single crystalline with {111} oriented planes including spiral nanoplatelet structures.

In the mean time, biosynthesis of gold nanoplatelets was also demonstrated by additional species of bacteria, (*Rhodopseudomonas capsulate*)[90], mushroom (*Volvariella volvacea*)[126], and chitosan[127]. The results of biosynthesis using *Rhodopseudomonas capsulate* has shown another possible mechanism of enzymatic bioreduction by NADH-dependent reductase. In the study on *Volvariella volvacea*, binding of amine groups on gold nanoparticles was found by FTIR analysis indicating protein binding on gold surfaces through amine groups. In these three methods, hexagonal, triangular and truncated triangular nanoplatelets were synthesized and were single crystalline oriented along {111} faces.

Amino acids, elemental constituents for peptides and proteins, were used for nanoplatelet synthesis by Dong and coworkers[93]. Among twenty amino acids, aspartate was the only amino acid reported to synthesize gold nanoplatelet structures. For shape controlled synthesis of gold nanostructures, Lee and coworkers have demonstrated extensive studies using aspartate as reducing and capping agent and showed the synthesis

of various kinds of gold nanostructures. They reasoned the formation of nanoplatelets to a specific adsorption of aspartate on {111} planes.

So far, the studies on biosynthesis of gold nanoplatelets have observed the same kind of single crystalline nanoplatelets in hexagonal, triangular and truncated triangular geometries with {111} oriented planes. Many hypotheses were made to elucidate the mechanism of nanoplatelet formation by enzymes, proteins and amino acids. However, the process of nanoplatelets formation within the same features by various kinds of different biomaterials still remains indeterminate.

Table 1.4 Experimental conditions for biological synthesis of 2-D gold nanostructures

Biological entity		Gold salt	pH	Temp	Use of physical force	Shape	Size	Crystallinity	Orientation	Ref
Plant	Lemongrass (Cymbopagon flexuosus)	$HAuCl_4$	-	RT	-	Hexagonal, truncated triangular and triangular nanoplatelets	8~18nm	Single	{111}	[97]
	Aloe vera	$HAuCl_4$	-	RT	-	Nanotriangles	Height 2.7~7.9nm	Single	{111}	[101]
Alga	Chlorella vulgaris	$HAuCl_4$	-	RT	-	Hexagonal, truncated triangular and triangular nanoplatelets	Height 9~20nm, width 0.02~2.2um	Single	{111}	[103]
Seaweed	Sargassum sp.	$HAuCl_4$	1~13	RT~250	Vigorous stirring	Hexagonal, truncated triangular and triangular nanoplatelets	-	Single	{111}	[105]
fungus	Aspergillius niger	$HAuCl_4$	3~10	4~100	Stirring	Hexagonal, truncated triangular and triangular nanoplatelets & Spiral nanoplates	thickness ~20nm / width 100 ~ 300nm	Single	{111}	[111]
Bacteria	Rhodopseudomonas capsulata	$HAuCl_4$	4~7	RT	-	Truncated triangular and triangular nanoplatelets / nanoparticles	50~400nm / 10~50nm	-	{111}	[114]
Chitosan	Polysaccharide chitosan	$HAuCl_4$	-	40~100	-	Hexagonal, truncated triangular and triangular nanoplatelets	-	Single	{111}	[128]
	Protein	$AuCl_3$	Acidic	RT	-	Truncated triangular nanoplatelets	-	Single	{111}	[117]
Amino acid	Aspartate	$HAuCl_4$	-	RT	Mild stirring	Hexagonal nanoplatelets	30nm/a few micron	-	{111}	[119]
	Aspartate	$HAuCl_4$	-	RT	-	Hexagonal, truncated triangular and triangular nanoplatelets	-	Single	{111}	[120]

1.3.4 Experimental Progress in Biological Synthesis Techniques

Starting from the synthesis of spherical nanoparticles by use of proteins[91], biosyntheses of various kinds of gold nanostructures have been developed by a number of studies. Brown and coworkers have first demonstrated biosynthesis of gold nanoparticles and nanoplatelets using proteins secreted by *Escherichia coli* and proposed a growth mechanism for the formation of thermodynamically unfavored hexagon nanoplatelets[91]. Extracellular and intracellular synthesis of gold nanoparticles have been extensively studied using plants[72-74], fruits[128], algae[79], fungi[77,81,84,85,129], bacteria[82,87,89,90,129], actinomycetes[83,130], peptides[92] and amino acids[95,96,131,132] to demonstrate the use of biomaterials for reduction and stabilization of gold.

Dong's group was able to synthesize gold nanoparticles and single crystalline nanoplatelets using amino acids[93]. Among natural L-amino acids, aspartate showed capability of reducing and shape-directing gold crystal to form nanoplatelets whereas arginine, lysine, tryptophan, and tyrosine showed capability of reducing gold ions to form spherical nanoparticles. Sastry and coworkers were able to demonstrate separate synthesis of nanoparticles and nanoplatelets by using different fraction of lemongrass leaf extracts separated by column chromatography[75].

More studies on biosynthesis using leaves[76,125], mushroom[126], algae[78], seaweed[80], fungi[86], bacteria[88,90], chitosan[127] and amino acids[93,94,124] showed the versatility of biomaterials for the synthesis of gold nanostructures including nanoplatelets, nanoribbons, nanowires and nanoparticles, and proposed a few possible mechanisms of

bioreduction and platelet formation. The synthetic chemistry of gold nanoparticles using plant, algae, fungus and bacteria has considerable complexity presenting challenges to investigating the mechanism of bioreduction due to various kinds of biological elements, such as cell walls, proteins and enzymes, existing in living bioorganisms. In fact, Xie and coworkers have made efforts to narrow down the reason of bioreduction to a single element existing in algal extract and found that proteins existing in the algal extract had ability to reduce gold ions and shape-direct the growth of nanoplatelets. However, employing amino acids to the synthesis process of gold nanostructures not only eliminated various factors in the biomass or extracts of biomaterials but also reduced efforts to find complicated sequences of specific peptides[93,95,96,124]. Shape-controlled synthesis of gold nanostructures using aspartate showed that the shape of gold nanostructures is more dependent on the reaction environment rather than on the kind of biomaterials[94].

Biosynthesis processes of gold nanostructures in previous studies show similarities in the reaction conditions and resulting products. In common, the reaction solutions consisted of aqueous gold chloride and a fraction of biological entities. The reaction condition was mostly in ambient condition except a few studies showing the effect of temperature and pH. Gold nanoplatelets share very similar features of shape (hexagon, triangular) and crystallinity (single, {111} oriented plane) in all the studies that have been reported for biosynthesis and also for chemical synthesis. Even though only few reports are available for biosynthesis of 1D gold nanostructures, the same features for nanowires (polycrystalline) and nanoribbons (single crystalline, {111} oriented) and growth

mechanism could be found in the reported studies[88,94,124]. A clear reason for observing such similar gold nanostructures in many studies has not been demonstrated yet. However, systematic approaches to analyze and clarify common phenomenon of the biosynthetic processes should lead closer to the core of controlled synthesis of gold nanostructures.

1.4 Research Objectives

In light of the above discussion, the overall objective of the dissertation is to contribute toward improving fabrication processes of devices consisted of nanometer scale components by developing efficient and non-toxic methodologies for the assembly and synthesis of inorganic nanostructures via biological approaches.

The specific objectives of my work include:

1) Development of a highly selective assembly process of 1-D nanostructures via base-sequence-specific DNA hybridization for fabrication of nanowire-based devices.
2) Development of a simple and non-toxic synthesis process by use of amino acids to create gold nanomaterials of controlled shapes and investigate the effects of variables on the synthesis processes to understand the mechanism of shape-controlled synthesis of gold nanomaterials.
3) Investigate the chemical, physical and electrical properties and validate the efficacy of biologically assembled and synthesized nanomaterials as functional elements in gas sensing devices.

1.5 Dissertation Organization

Chapter 1 introduces conventional and biological approaches for the assembly and synthesis of nanostructures with experimental progresses from the starting point of those techniques to present. Chapter 2 presents DNA-assisted assembly of multi-segmented

nanowires with characterization of the electron transport properties of the assembled nanowires and application of the structures for gas sensing. Chapter 3 and 4 demonstrate amino acid-mediated synthesis of gold nanostructures. Chapter 3 is devoted to understanding the effect of variables on the synthesis process of gold nanostructures using glycine. Chemical, physical and electrical characterization of synthesized gold nanostructures, transient kinetics, electrochemical analysis of solvent system and application of gold nanostructures for gas sensing have also been demonstrated in chapter 3. Chapter 4 elucidates the effect of side chains of amino acids on the formation of different kinds of gold nanostructures.

1.6. References

(1) Kim, E. H.; Lee, B. J. *Metals and Materials International* **2009**, *15*, 531-537.
(2) Fierascu, R. C.; Dumitriu, I.; Ion, R. M., 2009; p 737-740.
(3) Xia, Y. N.; Whitesides, G. M. *Annual Review of Materials Science* **1998**, *28*, 153-184.
(4) Saitou, N. *International Journal of the Japan Society for Precision Engineering* **1996**, *30*, 107-111.
(5) John, N. S.; Kulkarni, G. U., 2007; p 977-981.
(6) Perez-Murano, F.; Abadal, G.; Barniol, N.; Aymerich, X. Proceedings of 1997 Electron Devices Conference (EDC), Barcelona, Spain, 1997; p 343-347.
(7) Xia, Y. N.; Whitesides, G. M. *Annual Review of Materials Science* **1998**, *28*, 153-184.
(8) Zhang, X.; Sun, C.; Fang, N. *Journal of Nanoparticle Research* **2004**, *6*, 125-130.
(9) Huang, Y.; Duan, X. F.; Wei, Q. Q.; Lieber, C. M. *Science* **2001**, *291*, 630-633.
(10) Deegan, R. D.; Bakajin, O.; Dupont, T. F.; Huber, G.; Nagel, S. R.; Witten, T. A. *Physical Review E* **2000**, *62*, 756-765.
(11) Huang, J. X.; Fan, R.; Connor, S.; Yang, P. D. *Angewandte Chemie-International Edition* **2007**, *46*, 2414-2417.
(12) Yu, G.; Cao, A.; Lieber, C. M. *Nat Nano* **2007**, *2*, 372-377.
(13) Whang, D.; Jin, S.; Wu, Y.; Lieber, C. M. *Nano Letters* **2003**, *3*, 1255-1259.
(14) Pauzauskie, P. J.; Radenovic, A.; Trepagnier, E.; Shroff, H.; Yang, P.; Liphardt, J. *Nat Mater* **2006**, *5*, 97-101.
(15) Smith, P. A.; Nordquist, C. D.; Jackson, T. N.; Mayer, T. S.; Martin, B. R.; Mbindyo, J.; Mallouk, T. E. *Applied Physics Letters* **2000**, *77*, 1399-1401.
(16) Morrow, T. J.; Li, M. W.; Kim, J.; Mayer, T. S.; Keating, C. D. *Science* **2009**, *323*, 352-352.
(17) Tanase, M.; Silevitch, D. M.; Hultgren, A.; Bauer, L. A.; Searson, P. C.; Meyer, G. J.; Reich, D. H., 2002; p 8549-8551.
(18) Bangar, M. A.; Hangarter, C. M.; Yoo, B.; Rheem, Y.; Chen, W.; Mulchandani, A.; Myung, N. V. *Electroanalysis* **2009**, *21*, 61-67.
(19) Hangarter, C. M.; Rheem, Y.; Yoo, B.; Yang, E. H.; Myung, N. V. *Nanotechnology* **2007**, *18*, 7.
(20) Bangar, M. A.; Ramanathan, K.; Yun, M.; Lee, C.; Hangarter, C.; Myung, N. V. *Chemistry of Materials* **2004**, *16*, 4955-4959.
(21) Menke, E. J.; Thompson, M. A.; Xiang, C.; Yang, L. C.; Penner, R. M. *Nature Materials* **2006**, *5*, 914-919.
(22) Mbindyo, J. K. N.; Reiss, B. D.; Martin, B. R.; Keating, C. D.; Natan, M. J.; Mallouk, T. E. *Advanced Materials* **2001**, *13*, 249-+.
(23) Stoermer, R. L.; Keating, C. D. *Proceedings of the SPIE - The International Society for Optical Engineering* **2004**, *5588*, 51-58.
(24) Hazani, M.; Hennrich, F.; Kappes, M.; Naaman, R.; Peled, D.; Sidorov, V.; Shvarts, D. *Chemical Physics Letters* **2004**, *391*, 389-392.
(25) Hazani, M.; Shvarts, D.; Peled, D.; Sidorov, V.; Naaman, R. *Applied Physics Letters* **2004**, *85*, 5025-5027.
(26) Chen, Y.; Liu, H. P.; Ye, T.; Kim, J.; Mao, C. D. *Journal of the American Chemical Society* **2007**, *129*, 8696-+.

(27) Zheng, M.; Jagota, A.; Strano, M. S.; Santos, A. P.; Barone, P.; Chou, S. G.; Diner, B. A.; Dresselhaus, M. S.; McLean, R. S.; Onoa, G. B.; Samsonidze, G. G.; Semke, E. D.; Usrey, M.; Walls, D. J. *Science* **2003**, *302*, 1545-1548.
(28) Wang, X.; Liu, F.; Andavan, G. T. S.; Jing, X. Y.; Singh, K.; Yazdanpanah, V. R.; Bruque, N.; Pandey, R. R.; Lake, R.; Ozkan, M.; Wang, K. L.; Ozkan, C. S. *Small* **2006**, *2*, 1356-1365.
(29) Chang, J. Y.; Wu, H. M.; Chen, H.; Ling, Y. C.; Tan, W. H. *Chemical Communications* **2005**, 1092-1094.
(30) Chen, M.; Guo, L.; Ravi, R.; Searson, P. C. *Journal of Physical Chemistry B* **2006**, *110*, 211-217.
(31) Wang, A. A.; Lee, J.; Jenikova, G.; Mulchandani, A.; Myung, N. V.; Chen, W. *Nanotechnology* **2006**, *17*, 3375-3379.
(32) Salem, A. K.; Chen, M.; Hayden, J.; Leong, K. W.; Searson, P. C. *Nano Letters* **2004**, *4*, 1163-1165.
(33) Wang, Y.; Tang, Z.; Tan, S.; Kotov, N. A. *Nano Letters* **2005**, *5*, 243-248.
(34) Faraday, M. *Philos. Trans.* **1857**, *147*, 145-181.
(35) Routkevitch, D.; Bigioni, T.; Moskovits, M.; Xu, J. M. *Journal of Physical Chemistry* **1996**, *100*, 14037-14047.
(36) Qingmin, Z.; Yan, L.; Dongsheng, X.; Zhennan, G. *Journal of Materials Science Letters* **2001**, *20*, 925-927.
(37) Wang, Z.; Su, Y. K.; Li, H. L. *Applied Physics a-Materials Science & Processing* **2002**, *74*, 563-565.
(38) Brust, M.; Walker, M.; Bethell, D.; Schiffrin, D. J.; Whyman, R. *Journal of the Chemical Society-Chemical Communications* **1994**, 801-802.
(39) Turkevich, J.; Stevenson, P. C.; Hillier, J. *Discussions of the Faraday Society* **1951**, 55-&.
(40) Wang, C. G.; Wang, T. T.; Ma, Z. F.; Su, Z. M. *Nanotechnology* **2005**, *16*, 2555-2560.
(41) Chiang, C. L. *Journal of Colloid and Interface Science* **2001**, *239*, 334-341.
(42) Subramaniam, C.; Tom, R. T.; Pradeep, T. *Journal of Nanoparticle Research* **2005**, *7*, 209-217.
(43) Leff, D. V.; Brandt, L.; Heath, J. R. *Langmuir* **1996**, *12*, 4723-4730.
(44) Hiramatsu, H.; Osterloh, F. E. *Chemistry of Materials* **2004**, *16*, 2509-2511.
(45) Aslam, M.; Fu, L.; Su, M.; Vijayamohanan, K.; Dravid, V. P. *Journal of Materials Chemistry* **2004**, *14*, 1795-1797.
(46) Ayyappan, S.; Gopalan, R. S.; Subbanna, G. N.; Rao, C. N. R. *Journal of Materials Research* **1997**, *12*, 398-401.
(47) Hoppe, C. E.; Lazzari, M.; Pardinas-Blanco, I.; Lopez-Quintela, M. A. *Langmuir* **2006**, *22*, 7027-7034.
(48) Sau, T. K.; Pal, A.; Jana, N. R.; Wang, Z. L.; Pal, T. *Journal of Nanoparticle Research* **2001**, *3*, 257-261.
(49) Gachard, E.; Remita, H.; Khatouri, J.; Keita, B.; Nadjo, L.; Belloni, J. *New Journal of Chemistry* **1998**, *22*, 1257-1265.
(50) Henglein, A.; Meisel, D. *Langmuir* **1998**, *14*, 7392-7396.
(51) Huang, Y. Z.; Wang, W. Z.; Liang, H. Y.; Xu, H. X. *Crystal Growth & Design* **2009**, *9*, 858-862.
(52) Gao, S. Y.; Zhang, S. X.; Jiang, K.; Yang, S. X.; Lu, W. W. *Current Nanoscience* **2008**, *4*, 145-150.

(53) Sarathy, K. V.; Raina, G.; Yadav, R. T.; Kulkarni, G. U.; Rao, C. N. R. *Journal of Physical Chemistry B* **1997**, *101*, 9876-9880.
(54) Heath, J. R.; Knobler, C. M.; Leff, D. V. *Journal of Physical Chemistry B* **1997**, *101*, 189-197.
(55) Corbierre, M. K.; Cameron, N. S.; Sutton, M.; Mochrie, S. G. J.; Lurio, L. B.; Ruhm, A.; Lennox, R. B. *Journal of the American Chemical Society* **2001**, *123*, 10411-10412.
(56) Selvan, S. T.; Spatz, J. P.; Klok, H. A.; Moller, M. *Advanced Materials* **1998**, *10*, 132-+.
(57) Chen, W.; Cai, W. P.; Zhang, L.; Wang, G. Z.; Zhang, L. D. *Journal of Colloid and Interface Science* **2001**, *238*, 291-295.
(58) Nagata, Y.; Mizukoshi, Y.; Okitsu, K.; Maeda, Y. *Radiation Research* **1996**, *146*, 333-338.
(59) Wang, J.; Wang, Z. X. *Materials Letters* **2007**, *61*, 4149-4151.
(60) Tsuji, M.; Miyamae, N.; Hashimoto, M.; Nishio, M.; Hikino, S.; Ishigami, N.; Tanaka, I. *Colloids and Surfaces a-Physicochemical and Engineering Aspects* **2007**, *302*, 587-598.
(61) Kim, F.; Song, J. H.; Yang, P. *Journal of the American Chemical Society* **2002**, *124*, 14316-14317.
(62) Niidome, Y.; Nishioka, K.; Kawasaki, H.; Yamada, S. *Chemical Communications* **2003**, 2376-2377.
(63) Kim, F.; Sohn, K.; Wu, J.; Huang, J. *Journal of the American Chemical Society* **2008**, *130*, 14442-14443.
(64) Wang, L.; Song, Y.; Sun, L.; Guo, C.; Sun, Y.; Li, Z. *Materials Letters* **2008**, *62*, 4124-4126.
(65) Pazos-Pe?rez, N. s.; Baranov, D.; Irsen, S.; Hilgendorff, M.; Liz-Marza?n, L. M.; Giersig, M. *Langmuir* **2008**, *24*, 9855-9860.
(66) Wang, C.; Hu, Y. J.; Lieber, C. M.; Sun, S. H. *Journal of the American Chemical Society* **2008**, *130*, 8902-+.
(67) Swami, A.; Kumar, A.; Selvakannan, P. R.; Mandal, S.; Pasricha, R.; Sastry, M. *Chemistry of Materials* **2003**, *15*, 17-19.
(68) Bakshi, M. S.; Possmayer, F.; Petersen, N. O. *The Journal of Physical Chemistry C* **2008**, *112*, 8259-8265.
(69) Bi, Y. P.; Lu, G. X. *Nanotechnology* **2008**, *19*, 6.
(70) Lee, J. H.; Kamada, K.; Enomoto, N.; Hojo, J. *Crystal Growth & Design* **2008**, *8*, 2638-2645.
(71) Chu, H.-C.; Kuo, C.-H.; Huang, M. H. *Inorganic Chemistry* **2005**, *45*, 808-813.
(72) Gardea-Torresdey, J. L.; Parsons, J. G.; Gomez, E.; Peralta-Videa, J.; Troiani, H. E.; Santiago, P.; Yacaman, M. J. *Nano Letters* **2002**, *2*, 397-401.
(73) Sharma, N. C.; Sahi, S. V.; Nath, S.; Parsons, J. G.; Gardea- Torresde, J. L.; Pal, T. *Environmental Science & Technology* **2007**, *41*, 5137-5142.
(74) Armendariz, V.; Herrera, I.; peralta-videa, J. R.; Jose-yacaman, M.; Troiani, H.; Santiago, P.; Gardea-Torresdey, J. L. *Journal of Nanoparticle Research* **2004**, *6*, 377-382.
(75) Shankar, S. S.; Rai, A.; Ankamwar, B.; Singh, A.; Ahmad, A.; Sastry, M. *Nat Mater* **2004**, *3*, 482-488.
(76) Chandran, S. P.; Minakshi, C.; Renu, P.; Absar, A.; Murali, S. *Biotechnology Progress* **2006**, *22*, 577-583.
(77) Shankar, S. S.; Ahmad, A.; Pasricha, R.; Sastry, M. *Journal of Materials Chemistry* **2003**, *13*, 1822-1826.
(78) Xie, J.; Lee, J. Y.; Wang, D. I. C.; Ting, Y. P. *Small* **2007**, *3*, 672-682.

(79) Singaravelu, G.; Arockiamary, J. S.; Kumar, V. G.; Govindaraju, K. *Colloids and Surfaces B: Biointerfaces* **2007**, *57*, 97-101.
(80) Liu, B.; Xie, J.; Lee, J. Y.; Ting, Y. P.; Chen, J. P. *The Journal of Physical Chemistry B* **2005**, *109*, 15256-15263.
(81) Mukherjee, P.; Ahmad, A.; Mandal, D.; Senapati, S.; Sainkar, S. R.; Khan, M. I.; Ramani, R.; Parischa, R.; Ajayakumar, P. V.; Alam, M.; Sastry, M.; Kumar, R. *Angewandte Chemie International Edition* **2001**, *40*, 3585-3588.
(82) Konishi, Y.; Tsukiyama, T.; Ohno, K.; Saitoh, N.; Nomura, T.; Nagamine, S. *Hydrometallurgy* **2006**, *81*, 24-29.
(83) Ahmad, A.; Senapati, S.; Khan, M. I.; Kumar, R.; Ramani, R.; Srinivas, V.; Sastry, M. *Nanotechnology* **2003**, *14*, 824-828.
(84) Ahmad, A.; Senapati, S.; Khan, M. I.; Kumar, R.; Sastry, M. *Journal of Biomedical Nanotechnology* **2005**, *1*, 47-53.
(85) Mukherjee, P.; Senapati, S.; Mandal, D.; Ahmad, A.; Khan, M. I.; Kumar, R.; Sastry, M. *ChemBioChem* **2002**, *3*, 461-463.
(86) Xie, J.; Lee, J. Y.; Wang; Ting, Y. P. *The Journal of Physical Chemistry C* **2007**, *111*, 16858-16865.
(87) Du, L.; Jiang, H.; Liu, X.; Wang, E. *Electrochemistry Communications* **2007**, *9*, 1165-1170.
(88) He, S.; Zhang, Y.; Guo, Z.; Gu, N. *Biotechnology Progress* **2008**, *24*, 476-480.
(89) Husseiny, M. I.; El-Aziz, M. A.; Badr, Y.; Mahmoud, M. A. *Spectrochimica Acta Part A: Molecular and Biomolecular Spectroscopy* **2007**, *67*, 1003-1006.
(90) He, S.; Guo, Z.; Zhang, Y.; Zhang, S.; Wang, J.; Gu, N. *Materials Letters* **2007**, *61*, 3984-3987.
(91) Brown, S.; Sarikaya, M.; Johnson, E. *Journal of Molecular Biology* **2000**, *299*, 725-735.
(92) Slocik, J. M.; Stone, M. O.; Naik, R. R. *Small* **2005**, *1*, 1048-1052.
(93) Shao, Y.; Jin, Y.; Dong, S. *Chemical Communications* **2004**, 1104-1105.
(94) Tan, Y. N.; Lee, J. Y.; Wang, D. I. C. *The Journal of Physical Chemistry C* **2008**, *112*, 5463-5470.
(95) Bhargava, S. K.; Booth, J. M.; Agrawal, S.; Coloe, P.; Kar, G. *Langmuir* **2005**, *21*, 5949-5956.
(96) Ahmad, A.; Mukherjee, P.; Mandal, D.; Senapati, S.; Khan, M. I.; Kumar, R.; Sastry, M. *Journal of the American Chemical Society* **2002**, *124*, 12108-12109.
(97) Shankar, S. S.; Rai, A.; Ankamwar, B.; Singh, A.; Ahmad, A.; Sastry, M. *Nat Mater* **2004**, *3*, 482-488.
(98) Armendariz, V.; Herrera, I.; peralta-videa, J. R.; Jose-yacaman, M.; Troiani, H.; Santiago, P.; Gardea-Torresdey, J. L. *Journal of Nanoparticle Research* **2004**, *6*, 377-382.
(99) Gardea-Torresdey, J. L.; Parsons, J. G.; Gomez, E.; Peralta-Videa, J.; Troiani, H. E.; Santiago, P.; Yacaman, M. J. *Nano Letters* **2002**, *2*, 397-401.
(100) Sharma, N. C.; Sahi, S. V.; Nath, S.; Parsons, J. G.; Gardea- Torresde, J. L.; Pal, T. *Environmental Science & Technology* **2007**, *41*, 5137-5142.
(101) Chandran, S. P.; Minakshi, C.; Renu, P.; Absar, A.; Murali, S. *Biotechnology Progress* **2006**, *22*, 577-583.
(102) Shankar, S. S.; Absar, A.; Murali, S. *Biotechnology Progress* **2003**, *19*, 1627-1631.
(103) Xie, J.; Lee, J. Y.; Wang, D. I. C.; Ting, Y. P. *Small* **2007**, *3*, 672-682.

(104) Singaravelu, G.; Arockiamary, J. S.; Kumar, V. G.; Govindaraju, K. *Colloids and Surfaces B: Biointerfaces* **2007**, *57*, 97-101.
(105) Liu, B.; Xie, J.; Lee, J. Y.; Ting, Y. P.; Chen, J. P. *The Journal of Physical Chemistry B* **2005**, *109*, 15256-15263.
(106) Philip, D. *Spectrochimica Acta Part a-Molecular and Biomolecular Spectroscopy* **2009**, *73*, 374-381.
(107) Shankar, S. S.; Ahmad, A.; Pasricha, R.; Sastry, M. *Journal of Materials Chemistry* **2003**, *13*, 1822-1826.
(108) Ahmad, A.; Senapati, S.; Khan, M. I.; Kumar, R.; Sastry, M. *Journal of Biomedical Nanotechnology* **2005**, *1*, 47-53.
(109) Priyabrata, M.; Absar, A.; Deendayal, M.; Satyajyoti, S.; Sudhakar, R. S.; Mohammad, I. K.; Ramani, R.; Renu, P.; Ajayakumar, P. V.; Mansoor, A.; Murali, S.; Rajiv, K. *Angewandte Chemie International Edition* **2001**, *40*, 3585-3588.
(110) Priyabrata, M.; Satyajyoti, S.; Deendayal, M.; Absar, A.; Khan, M. I.; Rajiv, K.; Murali, S. *ChemBioChem* **2002**, *3*, 461-463.
(111) Xie, J.; Lee, J. Y.; Wang; Ting, Y. P. *The Journal of Physical Chemistry C* **2007**, *111*, 16858-16865.
(112) Shiying, H.; Yu, Z.; Zhirui, G.; Ning, G. *Biotechnology Progress* **2008**, *24*, 476-480.
(113) Du, L.; Jiang, H.; Liu, X.; Wang, E. *Electrochemistry Communications* **2007**, *9*, 1165-1170.
(114) He, S.; Guo, Z.; Zhang, Y.; Zhang, S.; Wang, J.; Gu, N. *Materials Letters* **2007**, *61*, 3984-3987.
(115) Konishi, Y.; Tsukiyama, T.; Ohno, K.; Saitoh, N.; Nomura, T.; Nagamine, S. *Hydrometallurgy* **2006**, *81*, 24-29.
(116) Husseiny, M. I.; El-Aziz, M. A.; Badr, Y.; Mahmoud, M. A. *Spectrochimica Acta Part A: Molecular and Biomolecular Spectroscopy* **2007**, *67*, 1003-1006.
(117) Brown, S.; Sarikaya, M.; Johnson, E. *Journal of Molecular Biology* **2000**, *299*, 725-735.
(118) Slocik, J. M.; Stone, M. O.; Naik, R. R. *Small* **2005**, *1*, 1048-1052.
(119) Shao, Y.; Jin, Y.; Dong, S. *Chemical Communications* **2004**, 1104-1105.
(120) Tan, Y. N.; Lee, J. Y.; Wang, D. I. C. *The Journal of Physical Chemistry C* **2008**, *112*, 5463-5470.
(121) Bhargava, S. K.; Booth, J. M.; Agrawal, S.; Coloe, P.; Kar, G. *Langmuir* **2005**, *21*, 5949-5956.
(122) Mandal, S.; Selvakannan, P.; Phadtare, S.; Pasricha, R.; Sastry, M. *Journal of Chemical Sciences* **2002**, *114*, 513-520.
(123) Polavarapu, L.; Xu, Q.-H. *Nanotechnology* **2008**, *19*, 075601.
(124) Huang, L.; Zhang, Y.; Guo, Z.; Gu, N. *Chinese Science Bulletin* **2009**, *54*, 1626-1629.
(125) Ankamwar, B.; Chaudhary, M.; Sastry, M. *Synthesis and Reactivity in Inorganic, Metal-Organic, and Nano-Metal Chemistry* **2005**, *35*, 19 - 26.
(126) Philip, D. *Spectrochimica Acta Part a-Molecular and Biomolecular Spectroscopy* **2009**, *73*, 374-381.
(127) Wei, D.; Qian, W.; Shi, Y.; Ding, S.; Xia, Y. *Carbohydrate Research* **2007**, *342*, 2494-2499.
(128) Ankamwar, B.; Damle, C.; Ahmad, A.; Sastry, M. *Journal of Nanoscience and Nanotechnology* **2005**, *5*, 1665-1671.
(129) Gericke, M.; Pinches, A. *Hydrometallurgy* **2006**, *83*, 132-140.

(130) Ahmad, A.; Senapati, S.; Khan, M. I.; Kumar, R.; Sastry, M. *Langmuir* **2003**, *19*, 3550-3553.
(131) Selvakannan, P.; Mandal, S.; Phadtare, S.; Gole, A.; Pasricha, R.; Adyanthaya, S. D.; Sastry, M. *Journal of Colloid and Interface Science* **2004**, *269*, 97-102.
(132) Selvakannan, P. R.; Swami, A.; Srisathiyanarayanan, D.; Shirude, P. S.; Pasricha, R.; Mandale, A. B.; Sastry, M. *Langmuir* **2004**, *20*, 7825-7836.

Chapter 2: DNA-assisted Assembly of Multi-segmented Nanowires

2.1. Introduction

One-dimensional nanostructures including nanowires and nanotubes are becoming increasingly important as building blocks of nano devices, because of their unique electronic, physical, and optical properties that can be precisely controlled by controlling their shapes and sizes[1,2]. However, exploiting the full potential of nanostructures and their characteristics has been limited by the inability to spatially manipulate and address these nano-entities[3]. Efficiently controlled assembly of nanostructures into more complex structures is necessary for realizing applications such as nanoelectronics, spintronics, optoelectronics, sensors, and thermoelectric devices.

There have been several methods for assembling the nanostructures in complex architectures, which include during- and post-growth electric field assisted alignment[4-6], Langmuir-Blodgett methods[7,8], microfluidic techniques[9], and magnetic assembly[10-13]. Biorecognition-directed assembly is an attractive method to assemble nanostructures into functional devices because of the highly specific nature offered by biomolecules such as proteins and deoxyribonucleic acid (DNA). DNA is particularly attractive because the interaction between complementary DNA is very specific and reversible, enabling highly controlled assembly of nanostructures. DNA can be easily synthesized with different lengths, sequences, and functional groups. In addition, the sequence selectivity of DNA hybridization provides a way to create complex structures by incorporating multiple different sequence pairs. These properties in concert with the site-specific DNA

adsorption and the reversibility of the hybridization have been exploited for the assembly of Au nanoparticles functionalized with thiolated single-stranded DNA (ssDNA) onto a pre-patterned surface[14-18]. Selective assembly of gold nanoparticles on a defined gold pattern was demonstrated by passivating the rest of the surface with PEG-silane[19]. Recently, the direct assembly of gold nanowires on complementary surfaces has been reported[20]. It is easy to envision that even multi-segmented nanowires containing gold segments at each end can be selectively assembled using the DNA-assisted assembly method.

In this chapter, we demonstrate a facile way to assemble functional multi-segmented nanowires in a spatially controlled manner using DNA hybridization. This assembly technique was exploited for bridging multi-segmented Au/Pd/Au nanowires across two gold electrodes by the selective DNA hybridization. Measuring temperature dependent electrical property and sensing performance toward hydrogen investigated the properties of the nanowires.

2.2. Experimental Details

2.2.1. Nanowire Fabrication

Nanowires with diameter of approximately 200 nm were synthesized using template-directed electrodeposition. Anodized alumina (Anodisc® 13 from Waterman, Inc. with a nominal pore diameter of 200 nm) was used as a scaffold. A gold layer with a thickness of approximately 500 nm was sputtered on one side of the template to serve as the seed layer. The template was fixed to a glass support with the seed layer face down using double-sided conductive copper tape. The conductive copper tape was also used as a lead to the glass support. The entire sample, except for the middle of the template and the end of the copper tape lead, was masked with an insulator (Microstop, Pyramid Plastics, Inc.).

The Au/Pd/Au multi-segmented nanowires were synthesized by sequential electrodeposition of gold, palladium, and gold under potentiostatic conditions. Adjusting deposition times at fixed deposition potentials controlled the lengths of different segments. Platinum-coated titanium bars and saturated calomel electrodes (SCE) were used as anodes and reference electrodes, respectively, for all deposition. The gold segments were electrodeposited from ready-to-use cyanide-free gold electrolytes (RTU-25, Technic, Inc.) at 60 ^{O}C. The deposition potential was fixed at -0.5 V vs. SCE, which resulted in an average current density of 1.2 mA cm^{-2}. The pH of the electrolyte was maintained at 7.25. The current efficiency of the gold electrodeposition was approximately 100 %. The palladium segments were electrodeposited at room temperature from alkaline chloride electrolytes with ammonium ions as complexing agents. The electrolyte solution had a composition of 0.047 M $Pd(NH_3)_4Cl_2$ and 0.1 M

NH_4Cl at pH of 7.02. The deposition potential was fixed at -0.8 V vs. SCE, which resulted in an average current density of 3.2 mA cm^{-2}. At this deposition potential and temperature, the current efficiency of palladium electrodeposition was approximately 30 %. For all depositions, electrolyte solutions were magnetically agitated using 1 inch stir bar at 200 rpm in 100 ml beaker, and deposition potentials were controlled by a multichannel EG&G PAR VMP2 potentio/galvanostat.

After electrodeposition, the nanowire-embedded template was removed from the substrate followed by mechanical removal of the gold seed layer. The nanowire-embedded template was sonicated in acetone to remove the adhesives smeared by the copper tape. The adhesives on the template surface could hinder the dissolution of the alumina template and also remained in the final nanowire solution as contaminants. The nanowire embedded template was then immersed in 5 M NaOH for 24 hr. at 60 °C for selective removal of template. The suspended nanowires were thoroughly washed with nanopure water for three times. Finally, the nanowires were stored in 1 ml of nanopure water.

2.2.2. Microfabrication of Gold Electrodes

The gold electrodes were microfabricated on silicon substrate using standard lithographic patterning. Using chemical vapor deposition (CVD), one-micron thick SiO_2 film was first deposited on a (100) oriented silicon wafer to insulate the substrate. After photo lithographically defining the electrode area, a Cr adhesion layer and a ~3000 Å-

thick Au layer were e-beam evaporated. Finally, the electrodes were defined using lift-off techniques. The gap distance between electrodes was fixed at 3 µm.

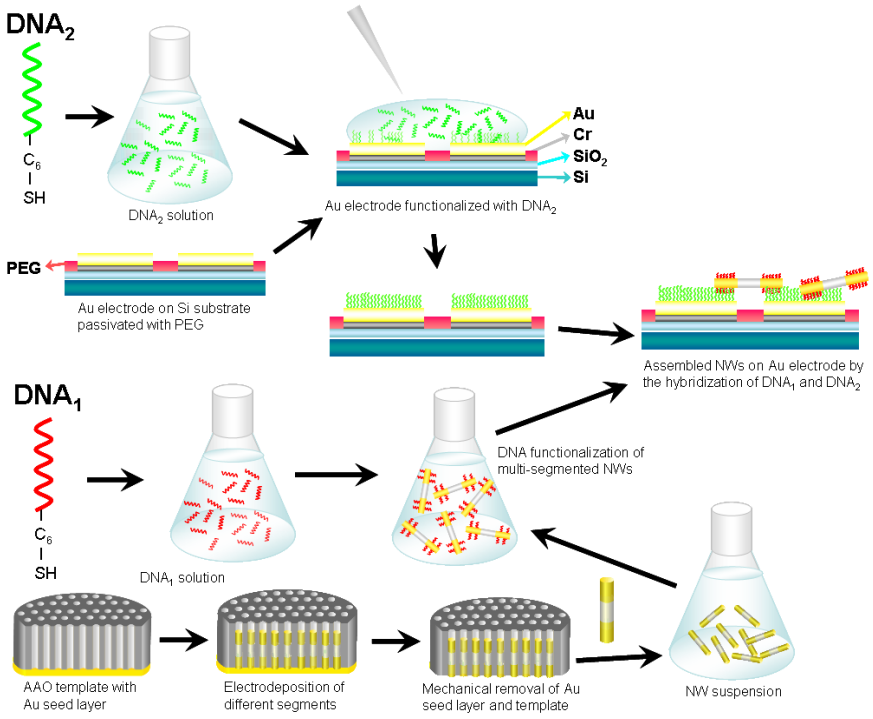

Figure 2.1 Schematic illustration of DNA assisted assembly of nanowires.

The upper part of the schematic illustrates the DNA functionalization of gold electrodes with DNA_2, and the lower part of the schematic illustrates the DNA functionalization of the nanowires with complimentary DNA. After the DNA functionalization, the nanowires are assembled across the gold electrodes.

2.2.3. DNA Functionalization

Figure 1 shows the schematic illustration of DNA functionalization and assembly of mutli-segmented nanowires on microfabricated gold electrodes. The protocols for DNA

functionalization were adopted in part from Papra *et al.* for passivating the silicon dioxide surface with PEG silane, and from Kannan *et al.* for functionalizing the nanowires and gold electrodes with DNAs[19, 21]. The base sequences of the complementary DNAs (i.e. DNA_1 and DNA_2) used for this study were:

DNA_1: 5'- SH-C_6-TTTTTTTTTTTTTTTTTTT AAT ATT GAT AAG GAT

DNA_2: 5'- SH-C_6-TTTTTTTTTTTTTTTTTTT ATC CTT ATC AAT ATT

DNA_1 and DNA_2 were used to functionalize the nanowires and the gold electrode surface, respectively. The first 20 bases from 5' end function as spacers and the rest 15 bases as linkers that hybridize to the complementary base sequences.

The thiolated DNAs (Integrated DNA Technologies) were dissolved in 100μL of a 0.1 M dithiothreitol (DTT) solution, and kept at room temperature for 12 hours in order to reduce the disulfide bonds. The solution was diluted to a final volume 1 mL with nanopure water, and ran through a NAP-10 column (GE Healthcare Bio-Sciences AB) to remove the DTT from the DNA solution. The final volume and the concentration of the DNA solutions after being eluted were approximately, 1.5 mL and 100 μM, respectively. The DNA solutions were kept frozen to prevent the formation of disulfide bonds.

A silicon chip with patterned gold electrodes was first cleaned with Piranha (70 vol % sulfuric acid and 9 vol % hydrogen peroxide in water) for 20 minutes. The chip was then washed three times in nanopure water and dried at 90 °C for 10 minutes. A PEG-toluene solution consisting of 0.2 vol % PEG-silane + 0.08 vol % HCl + 99.97 vol % toluene was

sonicated in medium power for 10 minutes and transferred to a clean glass beaker. The chip was placed in the PEG-toluene solution for 1 hour and washed once in toluene, once in ethanol and finally in nanopure water. 20 μL of DNA_2 solution was added to cover on the gold electrodes for 12 hours. The chip was rinsed with 0.1 vol % Tween-20 followed by nanopure water, and placed in 1mM mercaptohexanol (MCH) for 1 hour. MCH was used to assist the single-stranded DNAs (ssDNA) to stand vertically on the surface. Finally, the chip was washed with nanopure water for 2 minutes.

The nanowires were suspended in 200 μL of a 14.7 mM phosphine ligand solution and incubated for 12 hours on a rotator. 100 μL of DNA_1 solution was added to the nanowire suspension and incubated for another 12 hours. NaCl was added to the solution to a final concentration of 50 mM to aid the oligonucleotides to stand vertically on the nanowire surfaces. After the functionalization, the solution was centrifuged at 14,000 rpm for 10 minutes and the supernatant containing the unreacted ssDNAs was removed. The DNA functionalized nanowires were re-suspended in 500 μL of 10 mM phosphate buffer (PB) and 0.3 M NaCl solution.

2.2.4. DNA Hybridization

The ssDNA-functionalized chip was incubated in a solution of the nanowires conjugated to the complementary oligonucleotides for 12 hours to allow the hybridization between complementary ssDNAs. After the hybridization, the chip was washed for 2 minutes with 0.1 vol % Tween-20 in 10 mM PB and 0.3M NaCl solutions, followed by 10 mM PB and 0.3 M NaCl solution.

2.2.5. Morphology, Electrical Properties and Hydrogen Gas Sensing :

The morphology of Au/Pd/Au nanowires was examined by high resolution optical video microscope (KH-3000, Hirox, Inc.) and scanning electron microscopy (Philips model # XL30-FEG). The crystal structure of Au/Pd/Au nanowires was determined using X-ray diffractometer (D8 Advance Diffractometer by Bruker using Cu K_α radiation). The temperature dependent electrical properties of Au/Pd/Au nanowires were characterized using Physical Property Measurement System (PPMS). The I-V characteristics of Au/Pd/Au nanowires were analyzed using semiconductor parameter analyzer (HP model # 4155A).

The gold electrodes with assembled Au/Pd/Au nanowires were wire-bonded to a chip carrier. 1.3 cm^3 sealed glass chamber with inlet and outlet ports for gas flow-through was positioned over the sensor chip. The circuits were connected to a semiconducting parameter analyzer to continuously monitor the voltage change at a constant current of 200 μA. The electrical resistance of the sensor was determined by applying Ohm's law based on the measured voltages. The gas flow rates of hydrogen and dry air were regulated using mass flow controllers (Alicat Scientific Incorporated, Tucson, AZ). All experiments were conducted at room temperature with hydrogen (purity: 99.998 %) diluted in dry air (purity: 99.998%) at a flow rate of 150 std. cm^3 min^{-1}.

2.3. Results and Discussion

2.3.1 Electrochemically Grown Multi-segmented Nanowires

Figure 2 shows the optical cross-sectional images of Au/Pd/Au nanowires. The lengths of segments were 2.8/2.6/2.6 µm, respectively. Presence of two different metal segments was clearly indicated by the two distinct colors. The length of each segment was designed to match the microgap distance between the two bridging electrodes. Electrodeposition was controlled at a relatively low cathodic potential, which consequently applied low current density (-1.24 mA cm^{-2} for gold, -3.2mA cm^{-2} for palladium), to ensure the length uniformity of nanowires. Figure 2B shows single Au/Pd/Au nanowires well dispersed in nanopure water after the dissolution of alumina template with sodium hydroxide.

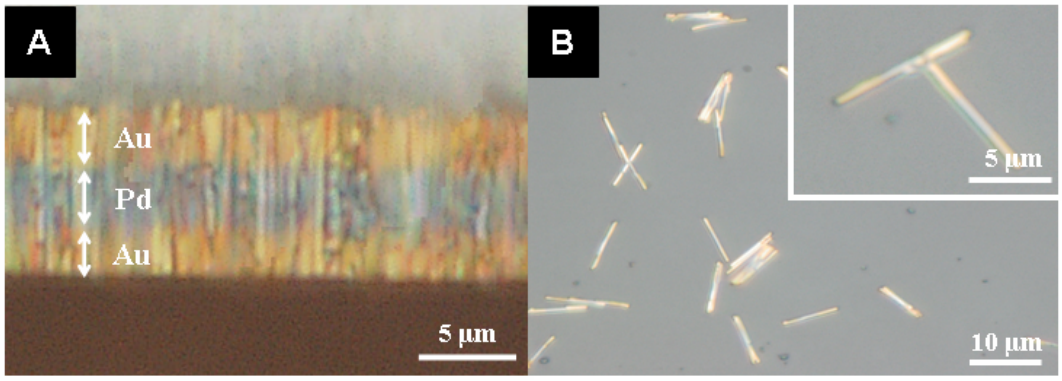

Figure 2.2 Optical images of multi-segmented Au/Pd/Au nanowires embedded in alumina template (A) and dispersed nanowires (B).

Figure 3 shows the X-ray diffraction pattern of Au/Pd/Au nanowires after the removal of alumina template. The nanowires were polycrystalline and show face centered cubic

(FCC) structure. The intensity ratio of I_{111}/I_{200} for gold segments was 2.4, which indicated that the gold segments have preferred the orientation along [111] direction. The palladium segments have also preferred the orientation along [111] direction. Using Debye-Scherrer's equation, the mean grain sizes of gold and palladium segments were determined to be 28.5 and 34.3 nm, respectively.

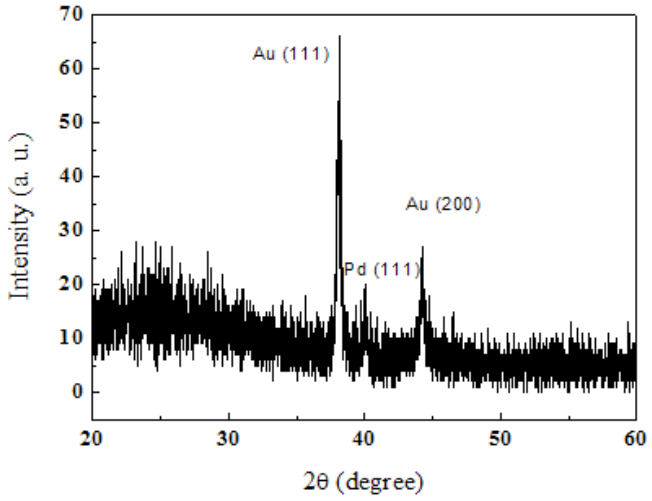

Figure 2.3 X-ray diffraction pattern of Au/Pd/Au nanowires.

2.3.2 DNA-assisted Assembly of Nanowires

To verify that the DNA-assisted assembly can be extended to multi-segmented nanowires, the ability to deposit Au/Pd/Au segmented nanowires onto plain gold surfaces was studied. On the same chip, one gold surface was functionalized with DNA_2 and the other gold surface was not functionalized as a control. The gold surfaces were incubated with a drop of the Au/Pd/Au nanowire solution that was functionalized with DNA_1. After washing the gold surfaces, observable nanowires deposition was detected only on the

gold surface functionalized with DNA_2 (figure 4A and B). The PEG groups presented on the silicon dioxide surfaces prevent any non-specific binding of nanowires[22,23].

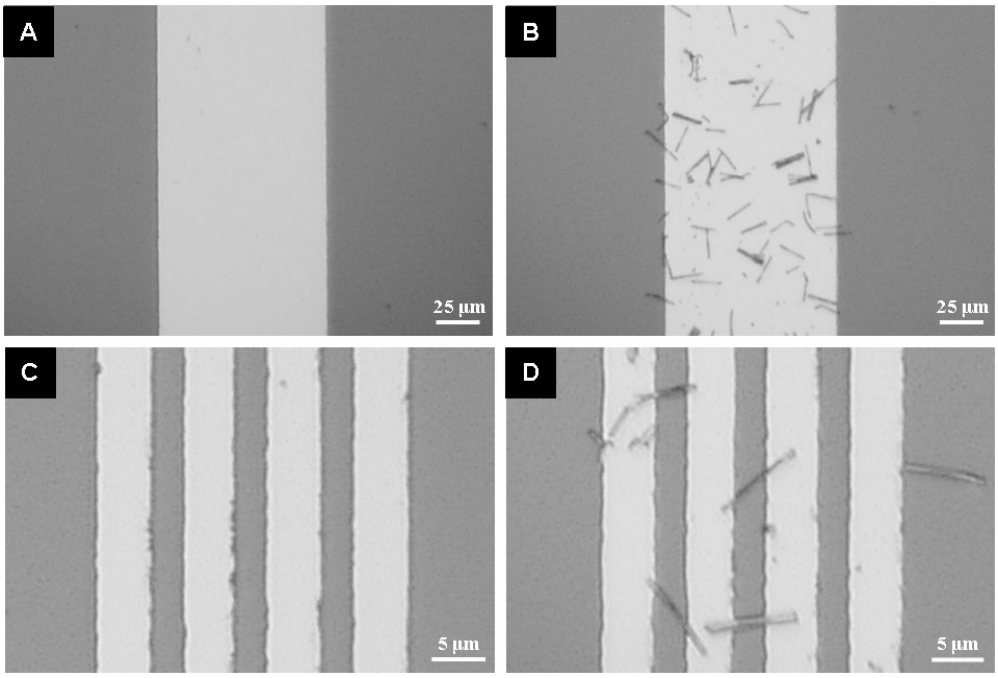

Figure 2.4 Assembly of nanowires on gold electrodes (A) unfunctionalized gold surface incubated with DNA_1 functionalized nanowires (control), (B) DNA_2 functionalized gold surface incubated with DNA_1 functionalized nanowires, (C) unfunctionalized interdigitated gold electrodes with DNA_1 functionalized nanowires (control) and (D) DNA_2 functionalized interdigitated electrodes with DNA_1 functionalized nanowires.

Previously Mbindyo *et al.* have demonstrated the DNA hybridization of gold nanowires on gold surfaces[20]. The group investigated surface coverage of 6 µm-long gold nanowires with a diameter of 200 nm. They achieved a surface density of $(9 \pm 2) \times 10^5$ NWs cm^{-2} by using a 36mer DNA oligo pair functionalized on the nanowires and surfaces. The surface coverage of our Au/Pd/Au segmented nanowires, which were 8 µm

in length and 200 nm in diameter, was 3.2 x 10^5 NWs cm^{-2}. This result indicates that the non DNA-binding palladium middle segment has no adverse effect on DNA hybridization and the same order of magnitude of nanowire coverage could be achieved.

Similar hybridization experiments were performed on a four-interdigitated gold electrode to further investigate the directed positioning of nanowires across electrodes. Using the same strategy of hybridization on two different interdigitated gold electrodes, we confirmed the same results showing no nanowires on the non-functionalized electrode (figure 4C), and many nanowires were deposited across DNA-functionalized electrodes (figure 4D). In accordance with our design of the nanowire, only the gold segments were interacting with the gold electrodes via DNA hybridization while the palladium segment remained in the middle of the micro-gap (figure 5A). Line scanning of the EDAX (figure 5B) confirmed that the palladium segment is located in the middle of the micro-gap, which indicated that gold segments were interacting with the gold electrodes.

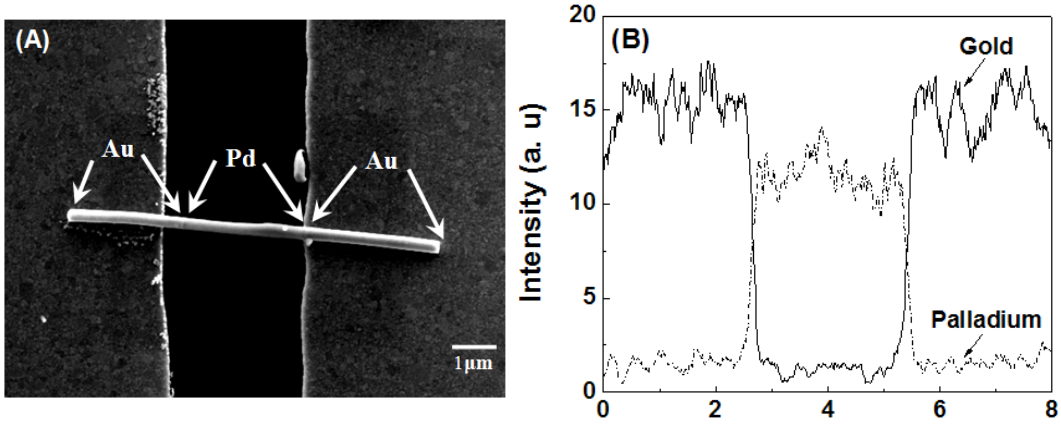

Figure 2.5 SEM image (A) and EDX line scan (B) of an assembled Au/Pd/Au nanowire between electrodes.

2.3.3 Electron Transport Properties of Assembled Nanowires

The room temperature I-V characteristic of assembled Au/Pd/Au nanowires was measured by sweeping the voltage from -10 mV to 10 mV. 66 % of observed assembled nanowires showed ohmic behavior, with resistance ranging from 66 to 178 Ω at room temperature (Figure 6B). Since the double-stranded DNA (dsDNA) layer between the electrodes and the nanowire is thinner (≈ 1 nm) and soft, the ohmic contact between nanowire and electrodes might be attributed to direct contact between them. The lowest resistivity of single assembled nanowire was approximately 126 mΩcm, which was greater than bulk palladium (10.5 mΩcm). Higher electrical resistivity of assembled nanowires might be attributed to greater electron scattering at the wire surfaces and the grain boundaries[24-28].

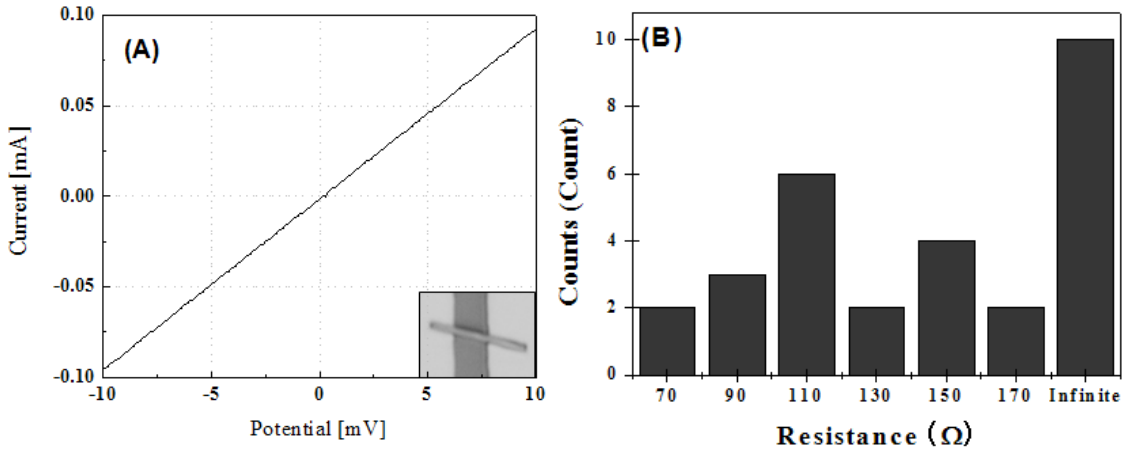

Figure 2.6 Room temperature I-V characteristic of a single Au/Pd/Au nanowire bridging microfabricated gold electrodes. The gap distance between electrodes was approximately 3 microns. Inset: optical image of the assembled nanowire.

Temperature dependent electrical resistance of Au/Pd/Au nanowire was measured from 10 to 320 K in increasing step. As the temperature was increased, the resistance of nanowire monotonically increased. For a detailed analysis, the temperature coefficient of resistance (TCR) was calculated using

$$TCR = \frac{1}{R_O}\frac{\Delta(R - R_O)}{\Delta(T - T_O)} \qquad \text{Eq. (1),}$$

where R is the resistance at temperature, T, and R_0 is the resistance at T_0, which is 300 K. Since, gold segments are assembled on top of electrodes, and have much lower electrical resistivity than the palladium segment, the majority of electrical resistance is expected to come from the palladium segment. Figure 7 shows the comparison of the normalized resistance of multi-segmented nanowires versus bulk polycrystalline palladium, and DNA templated palladium nanowires[27]. The diameter of DNA templated palladium nanowires was approximately 60 nm. The TCR of the multi-segmented nanowire was 0.0027 K^{-1} compared to 0.0007 K^{-1} and 0.0034 K^{-1} for the DNA templated Pd nanowire and bulk palladium, respectively, at 290 K. As expected, the TCR of multi-segmented nanowires (200 nm in diameter) lies between that of the DNA templated Pd nanowire (60 nm in diameter) and bulk palladium. Lower TCR of nanowire compared to the bulk counterpart is caused by an increase in the volume fraction of interface scattering sites with a decrease of nanowire diameter[30].

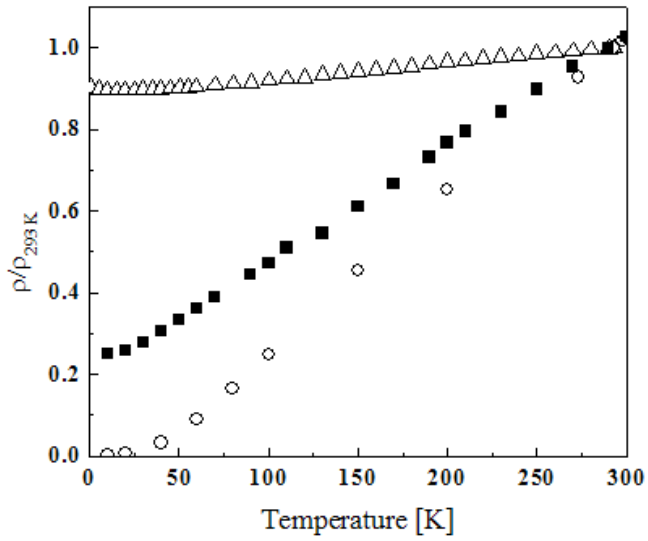

Figure 2.7 Normalized resistance of Au/Pd/Au nanowires (■), bulk palladium (○), and DNA templated palladium nanowire[29] (△) as a function of temperature.

2.3.4 Gas Sensing Properties of Assembled Nanowires

The functionality of the DNA-assisted assembled nanowires was demonstrated by utilizing the palladium middle segment for hydrogen sensing, since the resistance of palladium increases when it is exposed to hydrogen. The sensing performance of nanowire was characterized as a function of hydrogen concentration at room temperature. Figure 8 shows that the sensor resistance increases rapidly in response to hydrogen injection, and returns to the baseline resistance upon purging with dry air. The inset of figure 8 shows the sensitivity of the sensor, which was defined as the relative resistance change over the initial resistance. The assembled nanowires responded to hydrogen with a detection limit of 0.5 vol.% at room temperature. The sensitivity ($\Delta R/R$) of assembled

nanowires increased linearly with an increase in hydrogen concentration, and was comparable to previously reported results[31, 32]

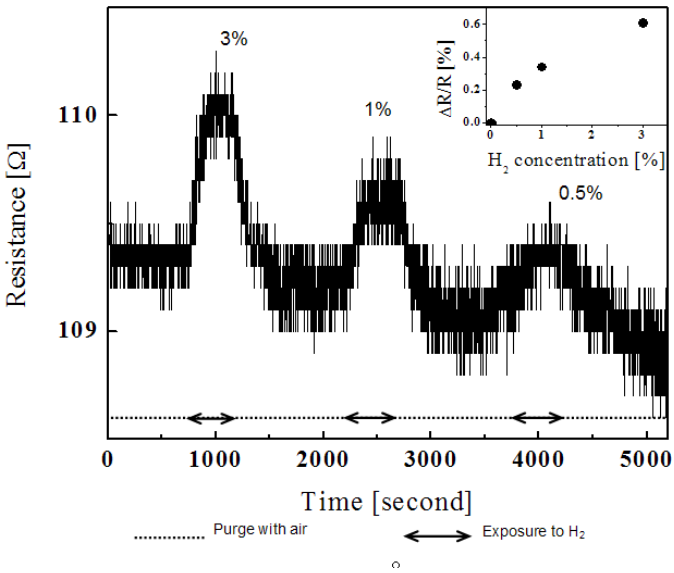

Figure 2.8 Resistance versus time in the presence of various hydrogen gas concentrations (3%, 1%, and 0.5 vol. %). Inset: the hydrogen sensitivity of assembled nanowire as a function of hydrogen concentration. The arrows indicate the exposure to hydrogen.

2.4. Conclusions

In summary, we demonstrated a facile method of site-specific assembling of Au/Pd/Au nanowires on microfabricated gold electrodes using DNA hybridization. The surface coverage of multi-segmented nanowires was similar to gold nanowires, which indicates that the non DNA-binding palladium middle segment has no adverse effect on DNA hybridization. The assembled nanowires show ohmic contact with minimum contact resistance. The temperature dependent electrical resistances show that the majority of electron scattering occurred at the surface and grain boundaries. The

assembled Au/Pd/Au nanowires were sensitive toward hydrogen gas at room temperature, with the detection limit of 0.5 %.

2.5. References

(1) X. Duan, Y. Huang, R. Agarwal, C. M. Lieber, *Nature* **2003**, 421, 241.

(2) Y. Xia, P. Yang, Y. Sun, B. Mayers, B. Gates, Y. Yin, F. Kim, H. Yan, *Adv. Mater*. **2003**, 15, 353.

(3) H. He, N. J. Tao, *Encyclopedia of Nanoscience and Nanotechnology*, American Scientific Publishers, CA **2004**.

(4) P. A. Smith, C. D. Nordquist, T. N. Jackson, T. S. Mayer, B. R. Martin, J. Mbindyo, T. E. Mallouk, *Appl. Phys. Lett.* **2000**, 77, 1399.

(5) X. Duan, Y. Huang, Y. Chi, J. Wang, C. M. Lieber, *Nature* **2001**, 409, 66.

(6) K. Ramanathan, M. A. Banhar, M. Yun, W. Chen, A. Mulchandani, N. V. Myung, *Nano Lett.* **2005**, 4, 1237.

(7) D. Whang, S. Jin, Y. Wu, C. M. Lieber, *Nano lett.* **2003**, 3, 1255.

(8) Y. Huang, X. W. Duan and C. M. Lieber, *Science* **2001**, 291, 630.

(9) A. K. Bentley, J. S. Trethewey, A. B. Ellis, W. C. Crone, *Nano Lett.***2004**, 4, 487.

(10) M. Tanase, D. M. Silevitch, A. Hultgren, L. A. Bauer, P. C. Searson, G. J. Meyer, D. H. Reich, *J. Appl. Phys.***2002**, 91, 8549.

(11) J. C. Love, A. R. Urbach, M. G. Prentiss, G. M. Whitesides, *J. Am. Chem. Soc.* **2003**, 125, 12696.

(12) C. M. Hangarter, N. V. Myung, *Chem. Mater.***2005**, 17, 1320.

(13) M. Tanase, L. A. Bauer, A. Hultgren, D. M. Silevitch, L. Sun, D. H. Reich, P. C. Searson, G. J. Meyer, *Nano Lett.* **2001**, 1, 155.

(14) J. J. Storhoff, R. Elghanian, R. C. Mucic, C. A. Mirkin, *J. Am. Chem. Soc.***1998**, 120, 1959.

(15) R. Elghanian, J. J. Storhoff, R. C. Mucic, R. L. Letsinger, C. A. Mirkin, *Science* **1997**, 277, 1078.

(16) C. A. Mirkin, R. L. Letsinger, R. C. Mucic, J. J. Storhoff, *Nature* **1996**, 382, 607.

(17) R. C. Mucic, J. J. Storhoff, C. A. Mirkin, R. L. Letsinger, *J. Am. Chem. Soc*. **1999**, 120, 12 674.

(18) G. P. Mitchell, C. A. Mirkin and R. L. Letsinger, *J. Am. Chem. Soc.* **1999**, 121, 8122.

(19) B. Kannan, R. P. Kulkarni, A. Majumdar *Nano Lett.* **2004,** 4, 1521.

(20) J. K. N. Mbindyo, B. D. Reiss, B. R. Martin, C. D. Keating, M. J. Natan, T. E. Mallouk, *Adv. Mater.* **2001**, 13, 249.

(21) A. Papra, N. Gadegaard, N. B. Larsen *Langmuir* **2001**, 17, 1457.

(22) J. H. Lee, H. B. Lee, J. D. Andrade *Prog. Polm. Sci.***1995**, 20, 1043.

(23) M. Amiji, K. Park, *ACS Symp. Ser*.**1994**, 540, 135.

(24) K. Fuchs, *Proc. Cambridge Philos. Soc.***1938**, 34, 100.

(25) E. H. Sondheimer, *Adv. Phys.***1952**, 1, 1.

(26) F. Mayadas, M. Shatzkes, *Phys. Rev.* B **1970**, 1, 1382.

(27) W. Steinhogl, G. Schindler, G. Steinlesberger, M. Engelhardt, *Phys. Rev.* B **2002**, 66, 075414.

(28) W. Steinhogl, G. Steinlesberger, M. Traving, M. Engelhardt, *J. App. Phys.* **2005**, 97, 023706.

(29) J. Richter, M. Mertig, W. Pompe, H. Vinzelberg, *App. Phys.* A **2002**, 74, 725.

(30) Zhang J, Wang X, Peng X and Zhang L, *Appl. Phys.* A **2002**, **75** 485.

(31) C. Wang, A. Mandelis, J. A. Garcia, *Sens. Actuators* B **1999**, 60, 228.

(32) V. G. Ponomareva, G. V. Lavrova, E. F. Hairetdinov, *Sens. Actuators* B **1997**, 40, 95.

Chapter 3: Glycine-mediated Synthesis of Gold Nanostructures

3.1. Introduction

With the recent advancement of nanotechnology and rising environmental concerns of nanomaterial manufacturing, there have been growing needs in the development of clean synthetic procedures for nanostructures with controlled morphology and structural architectures. Compare to chemical routes, which often involve toxic solvent-chemical systems and energy consuming operation conditions, biological approaches to material synthesis are ideal in the respect of realizing "Green processes".

In the past decade, the utilization of biological systems for the synthesis of inorganic structures has spurred as a result of environmental concerns. Various kinds of biological systems were reported utilizing living micro-organisms, extracts of plants, and sub units of bio-organisms for the synthesis of inorganic nanostructures. Intracellular and extracellular production of metals (Au[1] and Ag[2]), sulfides (CdS[3,4], PbS[5] and ZnS[6]) and magnetite[7] were elucidated as a result of bioreductions by bacteria, fungi and yeasts. Numbers of studies showed the use of plants, such as grass[8-10], algae[11] and seaweed[12], and constituents of biomolecules, such as proteins[13], peptides[14,15] and amino acids[16,17], to synthesize silver and gold nanostructures.

Synthesis of gold nanostructures has been studied by many research groups for the versatility of gold nanostructures resulted by their unique properties in nanoscale. Gold nanostructures can be produced in numbers of different geometry by bioreduction:

spheres[14], wires[17], ribbons[18], and platelets[9,10]. Amongst the gold nanostructures, gold nanoplatelets and nanoribbons were identified as single crystalline in many studies.

Single crystalline gold nanostructures have been attractive in the area of nanoelectronics for their higher conductivity and failure current in nanoscale than polycrystalline nanostructures[19]. As described in the previous paragraph, wide ranges of biomaterials were employed in numbers of studies for the syntheses of gold nanoplatelets, nanoribbons, nanowires and nanoparticles starting from living microorganisms to amino acids. Biological synthesis of gold nanoparticles and single crystalline nanoplatelets was first demonstrated by Brown and co-workers by using proteins[13]. Later, Xie and the co-workers, who studied the alga-mediated synthesis of gold nanostructures by using *Chlorella vulgari*, have identified the gold shape-directing proteins (GSP) claiming that it played the major role for synthesizing single crystalline gold nanoplatelets[11]. The synthesis of gold nanostructures by using amino acids was reported by Dong's group with a motivation of exploring the influence of amino acid moieties on the synthesis of single crystalline gold nanostructures which is the constituent units for peptides and larger biomolecules[16]. They claimed that among natural L-amino acids, aspartic acid showed a distinct capability to form single crystalline gold nanoplatelets while other amino acids, such as lysine, tryptophan, arginine and tyrosine, form nanoparticles. Extended investigations on the synthesis properties of aspartic acid studied by Wang's group showed that single crystalline gold nanoplatelets and nanoribbons could be synthesized by controlling the ratio of the concentrations of aspartic acid and hydrochloroauric acid ($HAuCl_4$)[19].

Even though the biomaterials used for the synthesis process were different, similar gold nanostructures could be found in many different studies. Many research groups have synthesized single crystalline gold nanoplatelets as products of biosynthesis which were in hexagonal, truncated triangular and triangular geometry grown along {111} faces. Gold nanoribbon structures have variations in their length, width and thickness depending on the synthesis conditions; however the single crystalline structures dominated by {111} faces still remains in common in many studies. Interestingly, the gold nanoplatelet and nanoribbon structures with the same geometries and crystallographic properties could also be found in the studies of wet chemical synthesis where the aqueous tetrachloroaurate solvent system was used in common[20-22].

Until now, most of the research was focused on the roles of various kinds of reducing and capping agents rather than on the solvent systems to control the geometries of the gold nanostructures. A few groups have briefly demonstrated the morphological changes of gold nanostructures in different pH or solvents[13,23,24]; however the prevailing variable, that determines the geometries of the gold nanostructures in spite of the use of different reducing and capping agents, still remains undiscovered. Thus, in this chapter, systematic approaches to understand the role of aqueous $HAuCl_4$ solvent system to the synthesis process of single crystalline gold nanostructures were demonstrated.

Numbers of researches showed the eligibility of biomaterials for the synthesis of gold nanostructures. Few groups found the cause of bioreduction on the peptides existing in the biomass[11], whereas direct approaches to the use of elemental unit, amino acids, towards the synthesis of gold nanostructures were demonstrated by other research

groups[13-18]. Here in this chapter, the assumption was made to consider the existence of proteins, peptides and amino acids as the cause of bioreduction. Therefore, glycine, which is in the simplest structure among amino acids, was selected as reducing and capping agents in this study, and its effect on the synthesis of single crystalline gold nanostructures was demonstrated.

Many novel biomaterials to synthesize single crystalline gold nanostructures have been discovered by many groups; however the electron transport properties and applications of the single crystalline gold nanostructures have rarely been studied so far. Thus, the characterization of electron transport properties, and applications of single crystalline nanoribbons to gas sensing were demonstrated.

3.2. Experimental Details

3.2.1. Materials

Hydrochloroauric acid ($HAuCl_4$) was purchased from Sigma Aldrich. Glycine (G), sodium chloride (NaCl), sodium hydroxide (NaOH), and hydrochloric acid (HCl) were purchased from Fisher Chemicals. Nanopure water was prepared by using Milli-Q system and was sterilized before use.

3.2.2. Synthesis of Gold Nanostructures

The reaction volume of the solution was 1ml, where the final concentration of $HAuCl_4$ and glycine were 0.5 and 0.18mM for standard experiments. The pH of $HAuCl_4$ solutions were adjusted to 4, 5, 7, and 10 with 5M of NaOH and 5M of HCl before adding glycine to the solutions. Concentration of 0.1, 0.3, 0.5 and 1mM were chosen for $HAuCl_4$ for the set of experiments where the concentration of $HAuCl_4$ was a variable, and similarly, 0.036, 0.18 and 0.9mM were chosen for concentration of glycine. The reaction solution was placed in dark environment at 37°C for three days without any disturbance.

After the reaction, the solution was centrifuged at 12,000rpm for 30minutes to separate the synthesized structures from the reaction solution. The supernatant was used for analyzing the amount of synthesized gold nanostructures, and the gold nanostructures remained in the bottom of the microcentrifuge tube were dispersed in nanopure water. Centrifugation and dispersion of gold nanostructures were repeated for three times to remove the gold ions from the solution.

3.2.3. Spectrophotometric Analysis

The supernatant of the reaction solution was diluted in 10% of HCl, and then the concentration of the remaining gold ions was analyzed with atomic absorption spectrophotometer (AAnalyst800, Perkin Elmer, Inc.) at flame mode. The measured concentration of remaining gold ions was subtracted from the initial gold concentration of the reaction solution to calculate the amount of synthesized gold.

The optical properties of the gold nanostructures dispersed in nanopure water were measured with UV-Vis spectrophotometer (DU800, Beckman Coulter, Inc.) in the range of wavelength from 400 to 1100nm.

3.2.4. Structural Characterization

Structural characteristics of the gold nanostructures were studied by using optical microscopy (KH-3000, Hirox, Inc.), scanning electron microscopy (SEM), transmission electron microscopy (TEM) and atomic force microscopy (AFM). The gold nanostructures were prepared on a silicon wafer and were observed with SEM (XL30-FEG, Royal Philips Electronics, Inc.) at 15kV of accelerating voltage.

For TEM imaging, the gold nanostructures dispersed in nanopure water were deposited onto carbon-coated Cu support grids and dried in ambient condition. The structures were observed with TEM (JEM-2100F, JEOL, Ltd.) at an accelerating voltage of 200kV. Selected area electron diffraction (SAED) was utilized to study the crystallographic orientation of the gold nanostructures.

Atomic force microscopy (AFM) was used to study the morphological characteristics of the gold nanostructures. The gold nanostructures were prepared on mica (Ted Pella, Inc.) for observation in tapping mode with Innova SPM (Veeco Instruments, Inc.).

3.2.5. Microfabrication of Gold Electrodes

The gold electrodes were microfabricated on silicon substrate using standard lithographic patterning. Using chemical vapor deposition (CVD), SiO_2 film was first deposited on a (100) oriented silicon wafer in the thickness of 300nm to insulate the substrate. After photo-lithographically defining the electrode area, Cr adhesion layer and Au layer were e-beam evaporated in the thickness of 100 and 300nm, respectively. In the end of the process, the electrodes were defined using lift-off techniques.

3.2.6. Electron Transport Property Measurements

Alternating current electric field was employed for the alignment of the gold nanostructures across microfabricated gold electrodes[25,26]. Nanoribbons and nanowires were aligned by placing a droplet of a suspension in volume of 2μl on the gap of the gold electrode while applying alternating current of $1V_{pp}$, 50 kHz and stayed for 30seconds. The droplet on the electrode was gently removed by a flow of nitrogen, and then 10μl of nanopure water was added and removed in the same way to clean out the residues. Nanoparticles were aligned in the same way at $16V_{pp}$ in the frequency range of 0.1~1MHz for 100 seconds.

Room temperature resistivity was measured in four probe configuration to correct the contact resistance using a Delta mode system (Keithley 6221 AC/DC Current Source and 2182A Nanovoltmeter, Keithley Instruments, Inc.) with applied current of ±2nA[27]. Temperature dependent electrical properties of the gold nanostructures were measured from 300K to 10K with the Delta Mode system, and a cold-finger cryogenic system (CCS-350SH, Janis Research Company, Inc.).

3.2.7. Gas Sensing Measurements

Interdigitated gold electrodes with AC aligned gold nanoribbon were wire-bonded to a chip carrier. A sealed glass chamber in volume of 1.3 cm^3 with inlet and outlet ports for gas flow-through were positioned over the gold electrode located on the chip carrier. The circuits were connected to Keithley 2631 (Keithley Instruments, Inc.) to continuously monitor the current change at a constant voltage of 0.5mV. The electrical resistance of the sensor was determined by applying Ohm's law based on the measured currents. The gas flow rates of H_2S and dry air were regulated using mass flow controllers (Alicat Scientific, Inc.). All experiments were conducted at room temperature with H_2S (100ppm) diluted in dry air (purity: 99.998%) at a flow rate of 200 std. cm^3 min^{-1}.

3.2.8. Electrochemical Analysis

Solutions in volume of 3ml of $HAuCl_4$ in different concentrations and pH with and without 0.9mM of glycine were purged with nitrogen in a sealed glass cell (CH222, CH Instruments, Inc.) for 30 minutes before linear sweep voltammetry (LSV) measurements.

Platinum wire (CHI221, CH Instruments, Inc.) was used as a counter electrode, Ag/AgCl (Saturated KCl, CHI111, CH Instruments, Inc.) electrode as a reference electrode, and a circular gold electrode in diameter of 2mm (CHI101, CH Instruments, Inc.) was used as a working electrode. The potential was swept from 1.5V to -0.5V in a scan rate of 2mV/sec which was controlled by a potentiostat (CHI1202A, CH Instruments, Inc.). In between measurements, the gold electrode was polished with aluminum oxide particle suspensions in the order of 3μm and 0.5μm to mirror smoothness, and then rinsed in water with ultrasonic for 5 minutes.

3.3. Results and Discussion

3.3.1. Effect of pH

The primary variable in the reaction condition was the pH for different sets of samples, where the concentration of $HAuCl_4$ and glycine were 0.5mM and 0.18mM, respectively. The initial color of 0.5mM $HAuCl_4$ solution is light yellow at low pH whereas the solution becomes transparent as the pH increases more than 6. As is clear from figure 3.1(a), the color of the gold nanostructure suspension from different pH solutions varies as transparent with existence of shining products (pH3.1 and 4.0), dark blue (pH5.0), purple (pH6.5) and pink (pH9.5) after 72hours of incubation at 37°C. Such differences in the color transitions at each pH indicate the formations of gold nanostructures in different sizes and shapes.

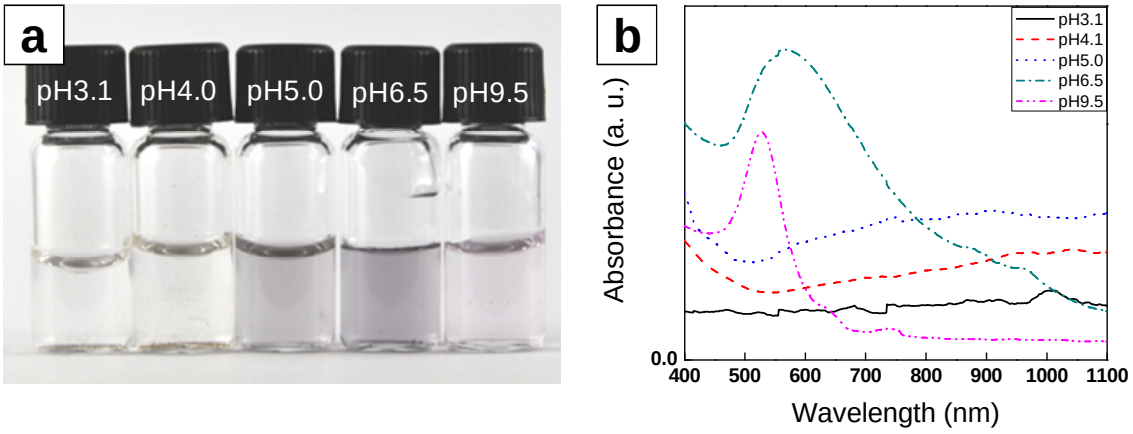

Figure 3.1 The photograph (a) and UV-Vis spectra (b) of as-prepared gold nanostructures dispersed in water. The gold nanostructures were synthesized by incubation of 0.5mM $HAuCl_4$ with 0.18mM glycine at pH 3.1, 4.0, 5.0, 6.5 and 9.5 for 3days at 37°C.

Gold nanostructures have optical properties strongly dependent on their sizes and shapes. Small spherical gold nanoparticles exhibit a single surface plasmon resonance (SPR) band in the range around 520nm or in longer wave lengths for larger particle sizes[28]. Anisotropic nanostructures exhibit two SPR bands for short and long axis of the structures which are known as transverse and longitudinal plasmon band[29]. The transverse plasmon band appears in the range around 520nm and is relatively insensitive to changes in the aspect ratio of the nanostructure, whereas the longitudinal plasmon band appears in longer wavelengths as the aspect ratio of the nanostructure increases[30,31]. The UV-Vis spectra in figure 3.1(b) show different locations and shapes of the bands for the gold nanostructures synthesized at different pH. The gold nanostructures synthesized at pH3.1 shows a band at 1012nm, Near-Infrared (NIR) region, which could be ascribed to the longitudinal plasmon band. The bands at lower wavelengths were difficult to be distinguished from the noise due to the low absorbance. Observed by SEM, the structures synthesized at pH3.1 were confirmed to be hexagonal, truncated triangular and triangular nanoplatelets that are shown in figure 3.2(a). The UV-Vis spectra of gold nanostructures synthesized at pH 4.1 and pH5.0 show similar trends to the spectra of 1 and 2D gold nanostructures, such as nanowires, nanobelts and nanokites[32-35]. The absorption bands are broadly increasing into the NIR region that could be ascribed to the polydispersity in the width, length and thickness of the nanostructures as observed in figure 3.2(b) and (c). The structures synthesized at pH4.1 were partially in hexagonal geometry and serrate ribbon structures. On the other hand, the structures synthesized at pH5.0 were elongated serrate ribbons without any large hexagonal platelets. The gold nanostructures synthesized at

pH6.5 and 9.5 show clear bands located at 566 and 527nm, respectively, which shapes can be qualitatively related to the nature of nanoparticles. Broadening and red-shifting of the absorption band could be the indication of wide size distribution or aggregation of the nanoparticles[36-40]. The results from the UV-Vis spectra and the SEM images have shown correlative relations between the optical properties and the shapes of the synthesized gold nanostructures. It was observed that nanoplatelets were the major product at pH3.1, nanokites and nanoplatelets at pH 4.1, nanowires and nanoribbons at pH 5.0 and nanoparticles at pH 6.5 and 9.5.

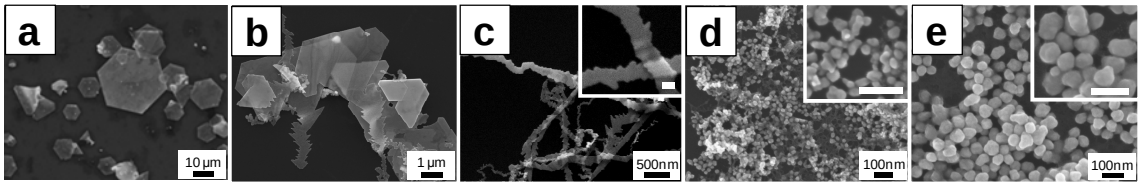

Figure 3.2 SEM images of gold nanostructures synthesized by incubation of 0.5mM $HAuCl_4$ with 0.18mM glycine at pH 3.1 (a), 4.0 (b), 5.0 (c), 6.5 (d) and 9.5 (e) for 3days at 37°C. Inset scale bar: 100nm.

The AFM topographies were taken to define the surface morphology and thickness of the gold nanostructures (figure 3.3). The thickness of the nanoplatelets fitted in the range of 20~60nm and the size of the platelets ranged from a few microns to 30 microns. The topography and the height profile of the gold nanoplatelet in figure 3.3(a) show that the surface was not smooth, but rough due to many nanoparticles remained on the surface of the platelet. The nanokites also showed similar range of thickness to nanoplatelets varying from 20~60nm. The surface from the plate-like head structure to the tail structure

was fairly smooth in the height profile in figure 3.3(b), which did not show any indication of two different structures sitting together, or merging to each other. The height of the nanoribbons varied from 10~50nm whereas the height remained uniform within the same structure.

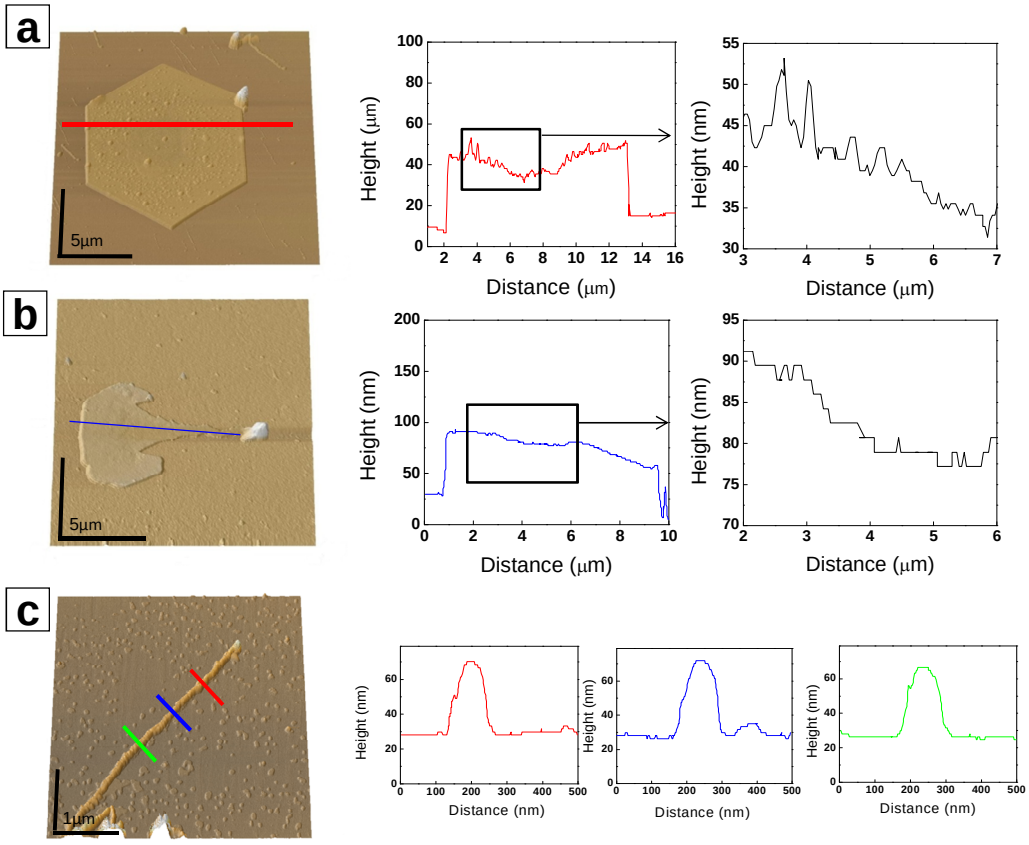

Figure 3.3 AFM topographies and height profiles of the gold nanoplatelet (a), nanokite (b) and a narrow nanoribbon (c).

Crystallographic orientation and phase analysis by TEM and SAED was carried out for the nanoplatelets, nanokites and nanoribbons. The nanoplatelets in figure 3.4(a) were in hexagonal and truncated triangular geometries with very smooth edges. Along with

nanoplatelets, nanoparticles of 5~8nm in diameter were also observed on and by the nanoplatelets which corroborates the observation of nanoparticles on the nanoplatelet by AFM in figure 3.3(a). The nanokite in figure 3.4(b) was partially in hexagon and in serrate ribbon structure whereas the nanoribbons were just in flat serrate ribbon structures. The diffracted spots of the SAED patterns for the three structures were in hexagonal symmetry which suggests face-centered cubic (fcc) single crystal growing along the (111) plane.

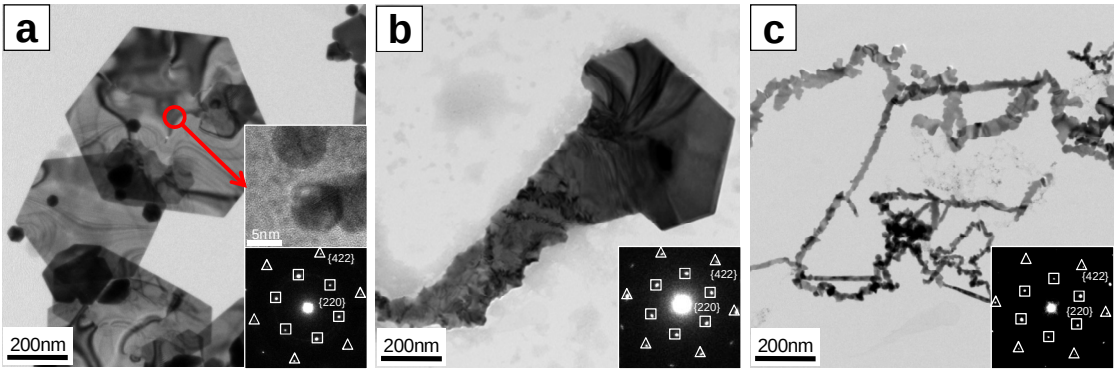

Figure 3.4 TEM images and the corresponding SAED patterns of the gold nanoplatelets, nanokites and nanoribbons. The SAED patterns were obtained by directing electron beam perpendicularly to the flat surface of each structure. The regular spots indexed to {220} and {422} are marked in squares and triangles, respectively.

The amount of synthesized gold after three days of incubation was determined by measuring the remaining gold ion concentrations in the solutions after the synthesis processes. The correlation of the amount of synthesized gold to pH is shown in figure 3.5(a). The highest amount of synthesized gold was observed in the pH range of 3~5,

where relatively larger structures, such as nanoplatelet, nanokite and nanoribbons, were synthesized. The amount of synthesized gold gradually decreases as the pH increases to 10.4, and only the nanoparticles were synthesized at this range of pH. No reduction was observed in the rage of pH lower than 1.7.

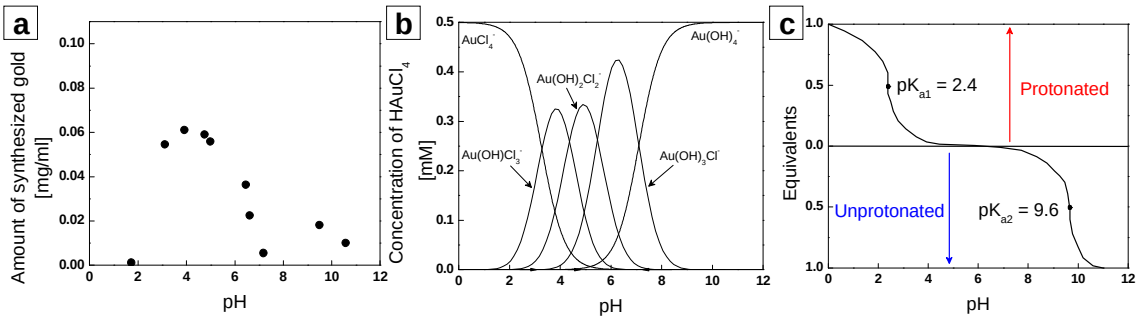

Figure 3.5 (a) The total amount of synthesized gold after three days of incubation carried out at 0.5mM $HAuCl_4$ at different initial pH with 0.18mM of glycine at 37°C. (b) The concentration of different species of gold complexes in 0.5mM $HAuCl_4$ as a function of pH which was calculated with the equilibrium constants reported by Nechayev et al.[41]. (c) The titration curve of glycine which shows the equivalent of hydrogen protonated and unprotonated from glycine as a function of pH[42].

Thus far, considerable structural and quantitative changes of the synthesized gold nanostructures caused by the changes of pH were observed. Theoretical investigation has carried out to find the reason of such changes with respect to pH. In the reaction solution, there are two components, $HAuCl_4$ and glycine, which chemical structures are sensitive to the change of the pH. Two components were considered in the focus of (1) the formation of different chlorohydroxyaurate ($AuCl_x(OH)_{4-x}^-$) complexes, in different pH, and (2) zwitterionic behavior of glycine.

Previous studies have shown that the gold ions from $HAuCl_4$ form different complexes with chloride (Cl^-) and hydroxide (OH^-) depending on the concentration of Cl^- and the pH of the solution[43]. The gold complexes remain as $AuCl_4^-$ in acidic condition. However, as the pH increases, the gold complexes gradually hydrolyze and finally become $Au(OH)_4^-$ in basic condition as a result of complete replacement of Cl^- to OH^- (Eq. 1~4). The concentration of each complex species as a function of pH was calculated with their equilibrium constants, which were reported by Nechayev et al.[41], and plotted in figure 3.5(b).

$$AuCl_4^- + OH^- \leftrightarrow Au(OH)Cl_3^- + Cl^- \quad \text{Eq. (1)},$$

$$Au(OH)Cl_3^- + OH^- \leftrightarrow Au(OH)_2Cl_2^- + Cl^- \quad \text{Eq. (2)},$$

$$Au(OH)_2Cl_2^- + OH^- \leftrightarrow Au(OH)_3Cl^- + Cl^- \quad \text{Eq. (3)},$$

$$Au(OH)_3Cl^- + OH^- \leftrightarrow Au(OH)_4^- + Cl^- \quad \text{Eq. (4)},$$

Correlating figure 3.5(a) and (b), the range of pH where the highest amount of synthesized gold was observed was related to the gold complex species of $AuCl_4^-$ and $Au(OH)Cl_3^-$. The amount of synthesized gold was gradually reduced as the species were transformed to $AuCl_2(OH)_2^-$, $AuCl(OH)_3^-$ and $Au(OH)_4^-$.

Glycine is known to exist predominantly as a zwitterion in aqueous solution near its isoelectric point (pI), pH 6.0. The amino group in glycine is protonated ($-NH_3^+$) and the carboxyl group is unprotonated ($-COO^-$) at pH 6.0, thus the net charge becomes zero. In acidic solution, the carboxyl group protonates as a result of buffering action. At the pK_a

of α-carboxyl group, pH2.4, the half of the carboxyl group protonates, and the other half ionizes as described in figure 3.5(c). Similarly, α-amino group unprotonates in basic condition, and the half of the amino group unprotonates when the pH reaches at its pK_a, pH9.6. The experimental results presented in figure 3.5(a) shows that the overall amount of synthesized gold was higher in the carboxyl-protonated pH range than the amino-unprotonated pH range except the pH below 1.7. The higher amount of synthesized gold at lower pH could be related to the electrostatic attraction of the protonated amine group towards the negatively charged gold complexes[44,45]. In contrast, the advantage of electrostatic interaction decreases due to the unprotonated amine group as the pH increases. The reason of large drop of the amount of synthesized gold below pH 1.7 could not be explained clearly. However, it can be assumed that the interaction of $AuCl_4^-$ and glycine ($^+H_3N\text{-}CH_2\text{-}COOH$), or the reactivities of the reactants are adversely affected by the high concentration of H^+.

3.3.2. Effect of Chloride Concentration

The addition of excessive amount of chloride into $HAuCl_4$ solution causes the replacement of OH^- on the gold complexes with Cl^-, thereby the numbers of chloride (x) in $Au(OH)_{4-x}Cl_x^-$ increases up to 4 depending on the amount of chloride and the pH of the solution[46]. If the speciation of gold complexes, rather than the pH itself, is the major variable to synthesize gold nanostructures in different shapes, the same type of structures would be expected from the solutions with similar speciation of gold complexes even at a different pH. Thus, to study how the chloride affects the speciation, thereby the

synthesized gold nanostructures, 0.5M of NaCl was added to 0.5mM of $HAuCl_4$ solutions at different pH with 0.18mM of glycine and then incubated at 37^{o}C for three days. In the range of pH4.7~5.8 with excessive amount of chloride, nanoplatelet structures were observed as majority with small amount of rod and particle structures. Nanokite-like structures were observed in the range of pH 6.6~7.5, and uneven shapes of nanoparticle structures were observed at pH10.1. Comparing the structures synthesized from the same range of pH without additional chloride, which is shown in figure 3.6, distinguishing differences could be noticed. Nanoribbon structures were the main products in the range of pH4.7~5.1, uneven nanoparticle structures were synthesized in the range of pH6.6~7.3, and uniform nanoparticle structures could be observed in the range of 9.5~10.5 without excessive amount of chloride. The observation by SEM of the structures showed that there were major structural changes in the synthesized gold nanostructures after the addition of 0.5M NaCl. The structures that could be found at low pH without addition of chloride was observed in higher ranges of pH in 0.5M NaCl solution with approximate interval of 2.5~3.

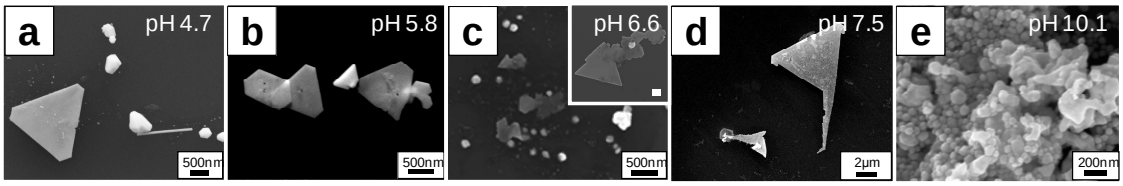

Figure 3.6 SEM images of gold nanostructures synthesized at pH4.7, 5.8, 6.6, 7.5 and 10.1 of 0.5mM $HAuCl_4$ with 0.18mM of glycine and addition of 0.5M NaCl to increase the chloride concentrations.

The amount of synthesized gold as a function of pH plotted in figure 3.7(a) shows the disparity of the trends between the sets of experiments with excessive amount of chloride and the one without additional chloride. The trend of the amount of synthesized gold with no additional chloride was demonstrated in section 3.5(a) with correlation of the highest amount of synthesized gold in the range of pH3~6, where $AuCl_4^-$ and $AuCl_3(OH)^-$ complex species exist as the majority. In the case of the sets of experiments with excessive amount of chloride, the amount of synthesized gold reached the highest value after pH 6 which is the most distinctive difference. However, the decrease of the amount of synthesized gold was not observed with excessive amount of chloride in the range below pH10.

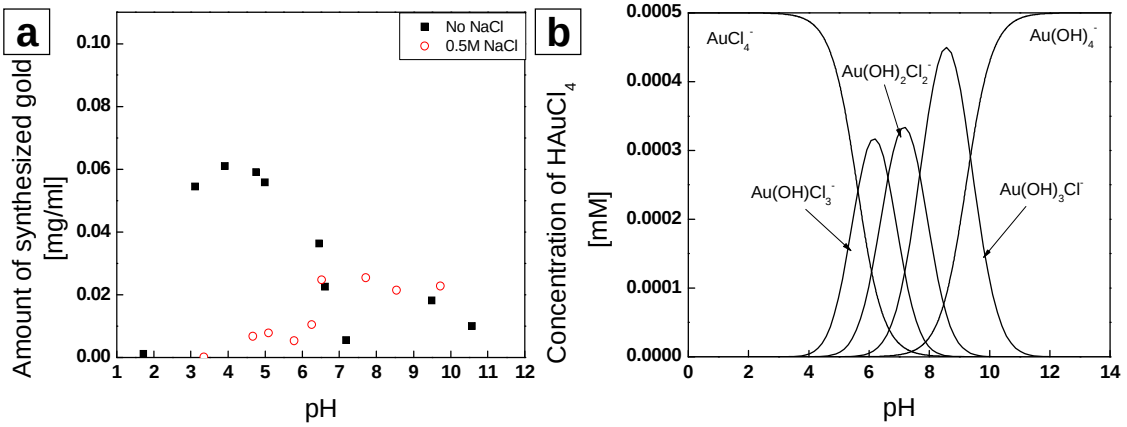

Figure 3.7 (a) The total amount of synthesized gold after three days of incubation of 0.5mM $HAuCl_4$, 0.18mM glycine with (○) and without (■) 0.5M of NaCl at different initial pH at 37°C. (b) The concentration of different species of gold complexes in 0.5mM $HAuCl_4$ and 0.5M NaCl as a function of pH.

The diagram of the concentration of gold species in the solution of 0.5mM $HAuCl_4$, 0.5M NaCl as a function of pH was calculated and plotted in figure 3.7(b). It is noticeable that the locations of the curves of gold complexes were shifted to higher range of pH than they were in figure 3.5(a), where there were no addition of chloride. Correlating the location of the curves of gold complexes to the amount of synthesized gold, the pH of the solution with 0.5M NaCl, where the amount of synthesized gold started to increase in figure 3.7(a), can be found in the range of pH in figure 3.5(a) where $AuCl_4^-$ and $Au(OH)Cl_3^-$ are the majority in the solution. This correlation of the trend of the amount of synthesized gold with the composition of the gold complexes coincides with those observed in figure 3.5. The amount of synthesized gold in 0.5M NaCl were lower in overall than that without NaCl which might be considered as the effect by reduced electrostatic attraction of the unprotonated amino group in glycine towards gold complex at high pH, and the interaction of glycine with sodium chloride. However the reasons have not been clearly concluded due to the lack of information. More detailed and systematic studies can be carried out to find the effect of NaCl on the reduction of gold by glycine at high pH.

3.3.3. Effect of $HAuCl_4$ Concentration

The speciation of gold complexes changes with respect to the concentration of $HAuCl_4$[46]. The changes in the speciation of gold complexes can result in the structural changes of synthesized gold nanostructures. Thus, to demonstrate the effect of the concentration of $HAuCl_4$ on the synthesized gold structures, the concentration of $HAuCl_4$

was varied as 0.1, 0.3 and 0.5mM while keeping the same condition for the pH and the concentration of glycine. After three days of incubation of the solutions of 0.1, 0.3 and 0.5mM of $HAuCl_4$ with 0.18mM of glycine at pH3.1, many structural differences of the gold nanostructures were observed in figure 3.8. The structures synthesized at 0.5mM $HAuCl_4$ were nanoplatelets as reported previously, whereas the structures synthesized at 0.1 and 0.3mM of $HAuCl_4$ resembled aggregated nanowires and nanoribbons, respectively.

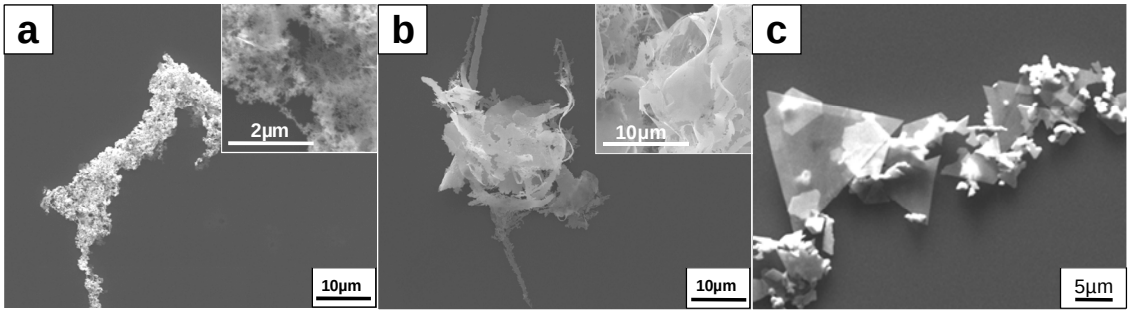

Figure 3.8 SEM images of gold nanostructures synthesized at 0.1 (a), 0.3 (b) and 0.5mM (c) of $HAuCl_4$ with 0.18mM of glycine at 37^{o}C for three days.

The amount of synthesized gold at different concentration of $HAuCl_4$ plotted in figure 3.9(a) shows the amount gradually increasing until 0.5mM, and then reaching to the plateau value after 0.5mM, which relates to the maximum amount of gold that can be reduced by 0.18mM of glycine at 37^{o}C in three days. The diagram of relative concentrations of $AuCl_4^-$, $Au(OH)Cl_3^-$ and $Au(OH)_2Cl_2^-$ plotted as a function of pH in figure 3.9(b) shows the relative concentrations of the gold complexes in 0.1, 0.3 and

0.5mM of $HAuCl_4$. Shifting of the curves towards lower pH could be found as the concentration of $HAuCl_4$ decreases from 0.5 to 0.1mM. It is apparent that the relative concentration of $AuCl_4^-$ decreases at the vertical line located at pH 3.1, indicating the pH of the solutions, while the relative concentrations of $Au(OH)Cl_3^-$ and $Au(OH)_2Cl_2^-$ increase as the concentration of $HAuCl_4$ decreases. Such changes in the composition of gold complexes could be ascribed as the cause of the formation of different gold nanostructures at 0.1 and 0.3mM of $HAuCl_4$. This result supports the previous results which show the correlation of the gold complex species and the structures of the synthesized gold nanostructures.

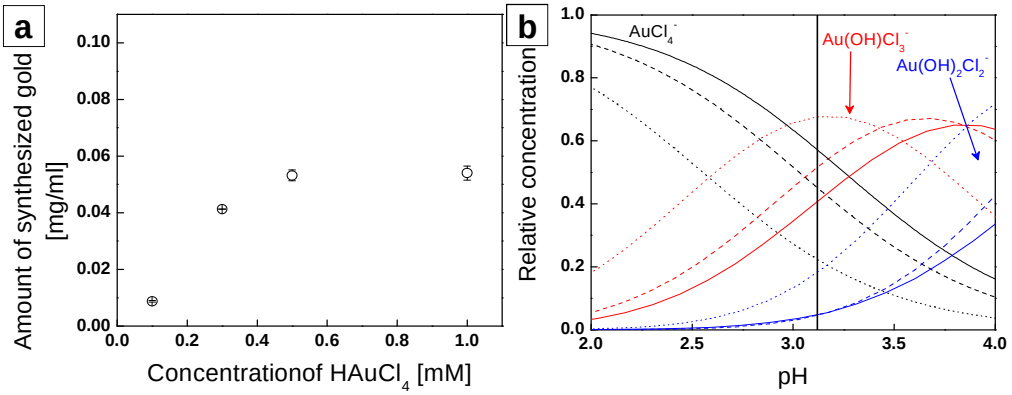

Figure 3.9 (a) Amount of synthesized gold at different concentrations of $HAuCl_4$ with 0.18mM of glycine at 37°C for three days. (b) Relative equilibrium concentrations of the gold species of $AuCl_4^-$ (black), $Au(OH)Cl_3^-$ (red) and $Au(OH)_2Cl_2^-$ (blue) at function of the pH of the solution at the concentration of $HAuCl_4$ at 0.1 (dotted line), 0.3 (dash line) and 0.5mM (solid line).

3.3.4. Effect of Glycine Concentration

The concentrations of each component in the solution are important variables to the synthesis process of gold nanostructures. Since glycine takes a role as reducing and

capping agent, the amount and the structural shape of the synthesized gold could be found different with respect to the concentration of glycine. Therefore, the effect of the concentration of glycine on the synthesis of gold nanostructures was first investigated by decreasing and increasing the concentration of glycine by a factor of 5 from the initial concentration of 0.18mM. As shown in figure 3.10(a) and (c), the different colors of the gold nanostructure suspensions indicate different shapes and sizes of the synthesized structures. The suspensions incubated with 0.036mM of glycine show transparent color at pH 3.1 and a little amount of shining products at pH4.0. The color was observed as green at pH5.0, grey at pH6.6 and pink at pH9.6. The longitudinal bands were only observable for the structures from pH 3.1 and 4.0, which were located at 965 and 1020nm, respectively. The UV-Vis spectrum of the gold nanostructures from pH5.0 shows a transverse band at 525nm and a clear longitudinal band at 917nm, which ascribes relatively more uniform widths and lengths of the nanostructures than those from the synthesis with 0.18mM of glycine. The wide band located at 556nm for the nanostructures from pH6.6 shows characteristics of nanoparticles with wide size distribution or aggregation[36-40]. The spectrum of the nanostructures from pH9.6 shows a narrow band at 545nm indicating nanoparticles in uniform sizes and shapes. The SEM image in figure 3.11(a) confirms the structures from pH3.1 as nanoplatelets where the majority of the nanoplatelets were in incomplete polygon structures. The structures from pH 4.0 were in shapes of nanokites, but distinctively smaller compared to the nanokites synthesized with 0.18mM of glycine at the same pH. Nanoribbon structures were observed from pH5.0 as shown in figure 3.11(c). The structures observed for pH6.6 were

small nanostructures with uneven sizes and shapes, and relatively much more uniform nanoparticles were observed for pH9.6, as ascribed from the UV-Vis spectrum.

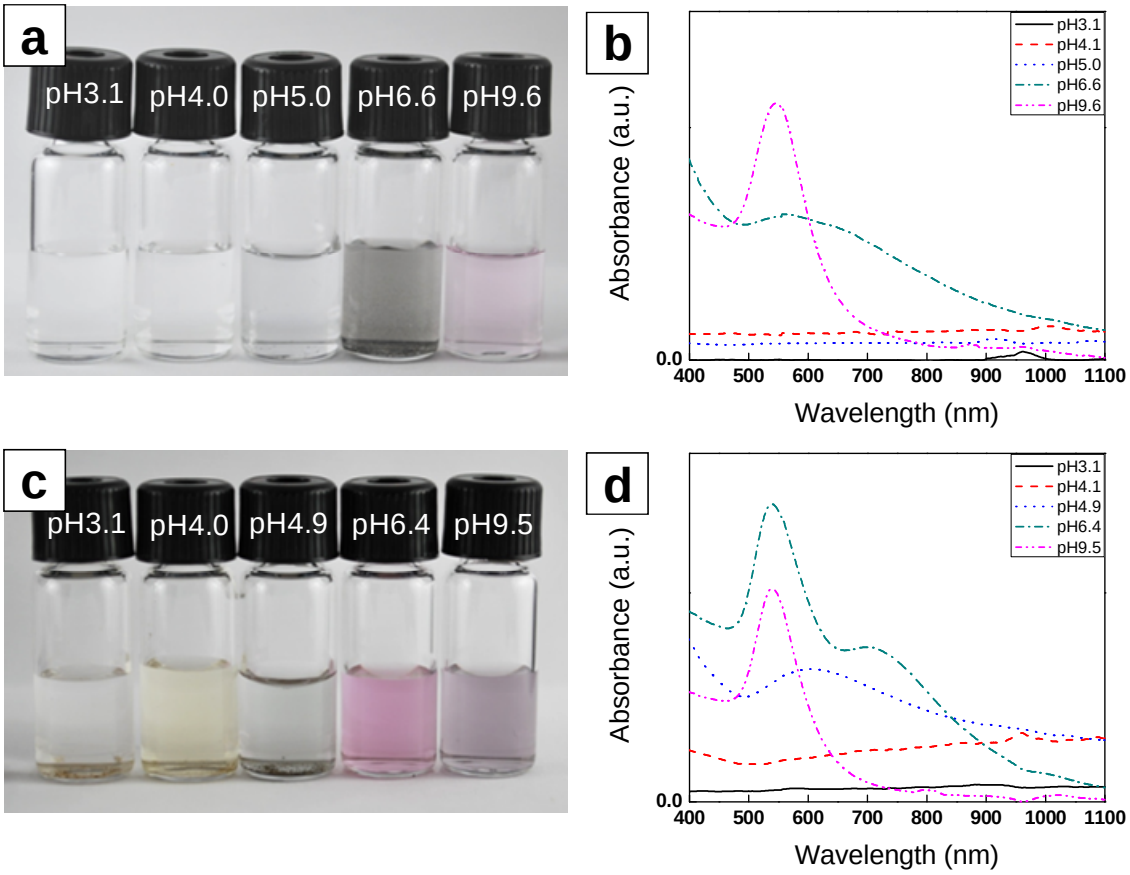

Figure 3.10 The photograph (a, c) and UV-Vis spectra (b, d) of as-prepared gold nanostructures dispersed in water. The gold nanostructures were synthesized by incubation of 0.5mM $HAuCl_4$ with 0.036mM (a, b) and 0.9mM (c, d) of glycine at pH 3.1, 4.0, 5.0, 6.5 and 9.5 for 3days at 37°C.

The suspensions synthesized with 0.9mM of glycine showed much more distinct colors than those from 0.036 or 0.18mM of glycine. The suspensions from pH3.1 and 4.0 in figure 3.10(c) showed transparent color with shining products like the others in different glycine concentrations. The suspension colors were green for pH4.9, pink for

pH6.4 and violet for pH9.5. No distinct bands for the suspensions of pH3.1 and pH4.0 were observed which might be due to the structures that quickly settle in the bottom of the glass bottle. The UV-Vis spectrum of gold nanostructures synthesized at pH 4.1 shows similar trend to the spectra of 1 and 2D gold nanostructures as observed in other counterparts at the same pH. The absorption bands were broadly increasing into the NIR region which ascribes the polydispersity in the width, length and thickness of the nanostructures as observed in figure 3.11(g). Sharp bands were observed for pH 6.4 and pH9.5 which indicates the presence of uniform nanoparticles. The SEM image in figure 3.11(f) shows the nanoplatelets synthesized at pH3.1 where many of the nanoplatelets had kink structures grown towards the center of the nanoplatelets. The structures from pH4.0 showed in figure 3.11(g) had irregular platelet-like structures with existence of aggregated nanoparticles which is different from the previous results of nanokite structures at the same pH. Nanoribbons with branches in random shapes and directions were observed from the suspension of pH 4.9. The nanoparticle structures found from the suspension of pH6.4 were fairly uniform in shapes and sizes that correlate well with the sharp band in the UV-Vis spectrum. The structures from pH 9.5 were also uniform nanoparticles, which was consistent with other conditions with different glycine concentrations at the same pH.

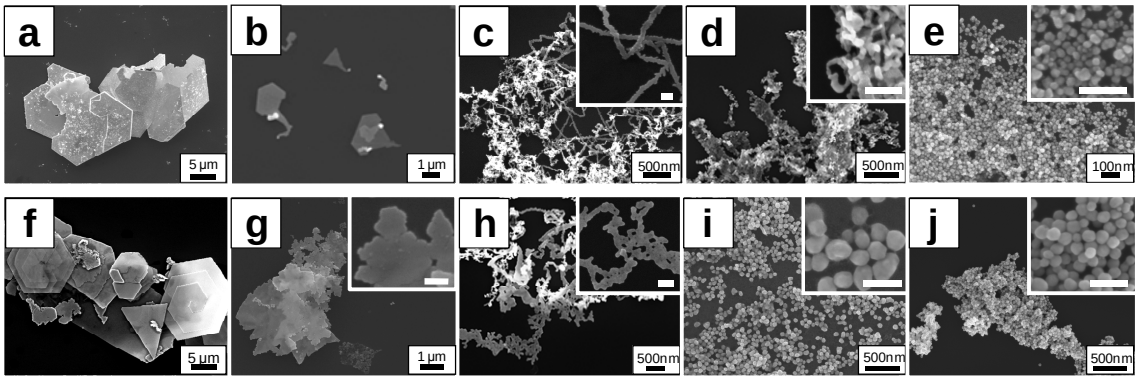

Figure 3.11 SEM images of gold nanostructures synthesized by incubation of 0.5mM $HAuCl_4$ at pH 3.1, 4.0, 5.0±0.1, 6.5±0.1 and 9.5±0.1 with 0.036mM (a ~ e) and 0.9mM (f ~ j) of glycine for 3days at 37°C. Inset scale bar: 100nm.

The correlations of the amount of synthesized gold to pH for three different concentrations of glycine are shown in figure 3.12. The trend of having the highest amount of synthesized gold in the range of pH 3~5, and the gradual decrease of it in the range of pH 7~10 prevails for all of the glycine concentrations. However the amount of synthesized gold had higher values for the sets of experiments with higher concentration of glycine indicating the capability of glycine as reducing agent with respect to its concentration.

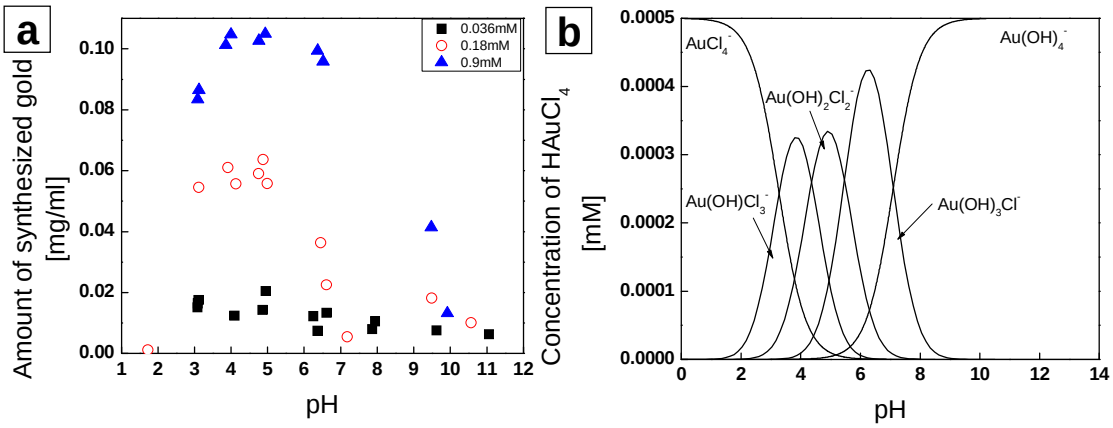

Figure 3.12 (a) The total amount of synthesized gold after three days of incubation of 0.5mM $HAuCl_4$ at different initial pH with 0.18mM of glycine at 37°C. (b) The concentration of different species of gold complexes in 0.5mM $HAuCl_4$ as a function of pH.

Overall, it was observed that there were changes in the shapes and the amounts of the synthesized gold depending on the concentration of glycine except for the range of pH above 9.5. The nanoplatelets, nanoribbons and nanoparticles synthesized at pH 3.1, 4.9 and 6.6, respectively, had the same basic structures at every concentration of glycine, but additional structures grown as kinks or branches on and by the basic structures. The structure of the nanokites showed consistencies in the basic shapes for 0.036 and 0.18mM of glycine. However, the structures became more like platelet structures with no distinct shapes at 0.9mM of glycine. Uniform nanoparticle structures were consistently observed at pH 9.5, but the average sizes of the nanoparticles were observed to increase as the concentration of glycine increased from 0.036 to 0.9mM.

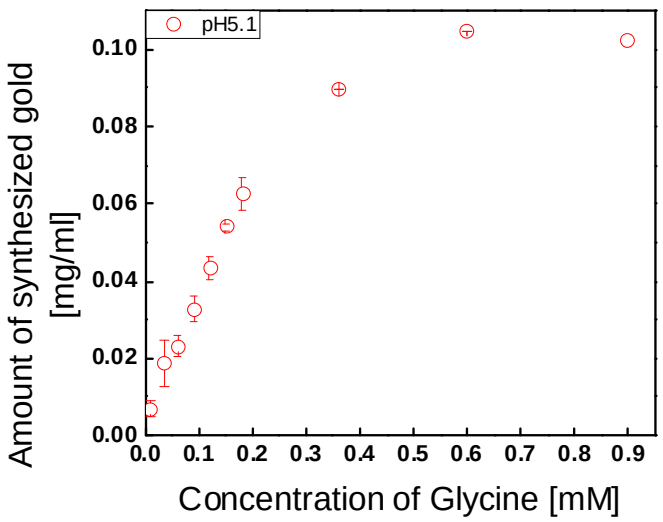

Figure 3.13 The glycine concentration dependence of the amount of synthesized gold after three days of incubation of 0.5mM $HAuCl_4$ at pH 3.1 and 5.1 with glycine concentration varied from 0.009 to 0.9mM at 37°C.

With particular interest on the nanoribbon structures, which showed sensitive changes to the concentration of glycine, the structural changes related to the concentration of glycine, was studied in detail. The amount of synthesized gold from 0.5mM $HAuCl_4$ solutions at pH 5.1 with glycine which concentration was varied from 0.009 to 0.9mM is shown in figure 3.13. The amount of synthesized gold linearly increases until 0.18mM of glycine, and then reaches to the point of full reduction of gold after 0.6mM. The trend of the amount of synthesized gold reaching to the plateau after 0.6mM of glycine can be explained by insufficient amount of gold complex ions compare to the amount of glycine in the solution. Since glycine has role as reducing agent in the system, the increase in the amount of glycine indicates the increase in the numbers of electrons available for the

reduction. Thus, linear increase of the amount of synthesized gold was reasonable in the synthesis process.

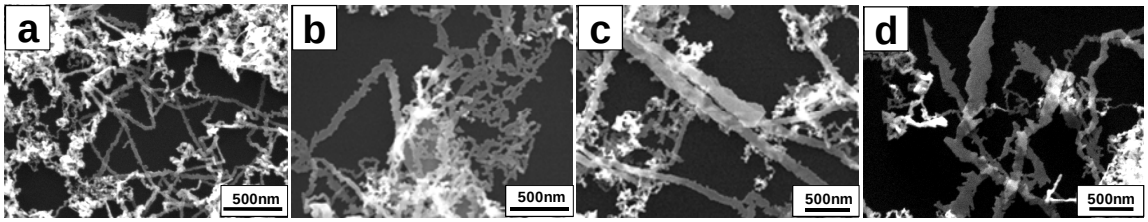

Figure 3.14 Nanoribbon structures synthesized at 0.036 (a), 0.06 (b), 0.12 (c) and 0.18mM (d) of glycine in 0.5mM $HAuCl_4$ at pH4.8. Scale bar: 1μm.

The nanoribbon structures observed with SEM (figure 3.14), and the average width and the width distribution of the nanoribbons synthesized with different amount of glycine (figure 3.15) show that the width and the shape of the nanoribbons became more irregular and random as the concentration of glycine increases.

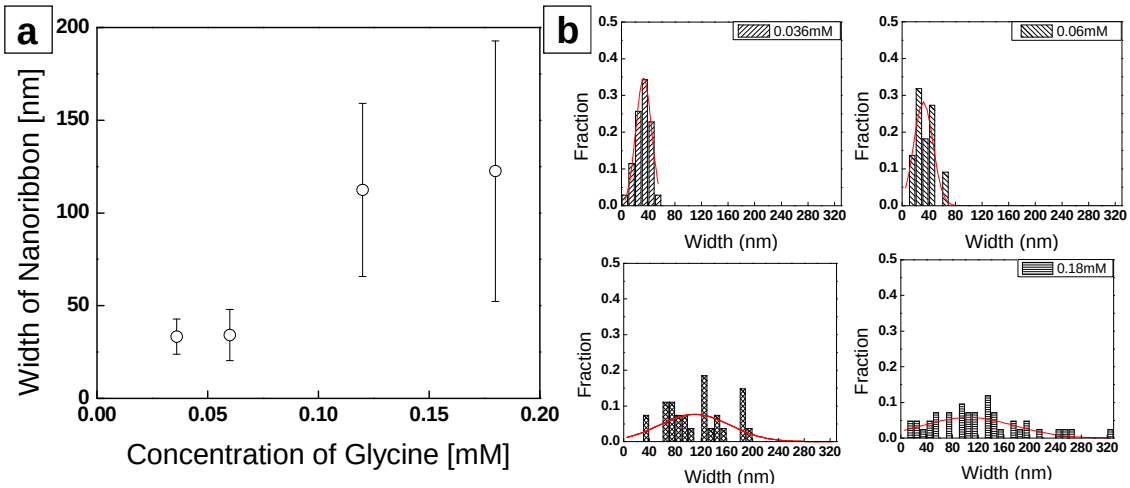

Figure 3.15 Average widths (a) and the histograms (b) of the nanoribbons synthesized at 0.5mM $HAuCl_4$ at pH4.8, 37^{o}C for three days with 0.036, 0.06, 0.12 and 0.18mM of glycine.

3.3.5. Effect of Temperature

The effect of the temperature on the synthesis of gold nanostructures was studied in the range of 4 to 90°C for 0.5mM $HAuCl_4$, 0.18mM Glycine at pH3.1. As shown in figure 3.16, the amount of synthesized gold is closely related to the temperature of the synthesis process. The amount of synthesized gold increases as the temperature raises, but the gold complex ions in the controls with no glycine also start to reduce in the temperature range higher than 50°C (figure 3.16(a)). The reduction of gold without reducing agents in high temperatures supports the hydrothermal reaction in aqueous solvent which has been widely studied for the synthesis of gold nanostructures [47]. However, the synthesis of gold nanostructures in such high temperatures is not very encouraging in sense of the control of the shapes of the nanostructures. The optical images of the synthesized gold nanoplatelets at 50 and 90 $^{\circ}$C are shown in figure 3.16(b) and (c). Compare to the structures in figure 3.2(a) which was synthesized at 37 $^{\circ}$C, increase in the irregularity of the structures could be found in the structures as the temperature increases to 50°C and 90°C. Thus the synthesis of gold nanostructures in high temperatures is not encouraging in this study since the role of glycine, as an effective capping agent to control the shapes, significantly reduces.

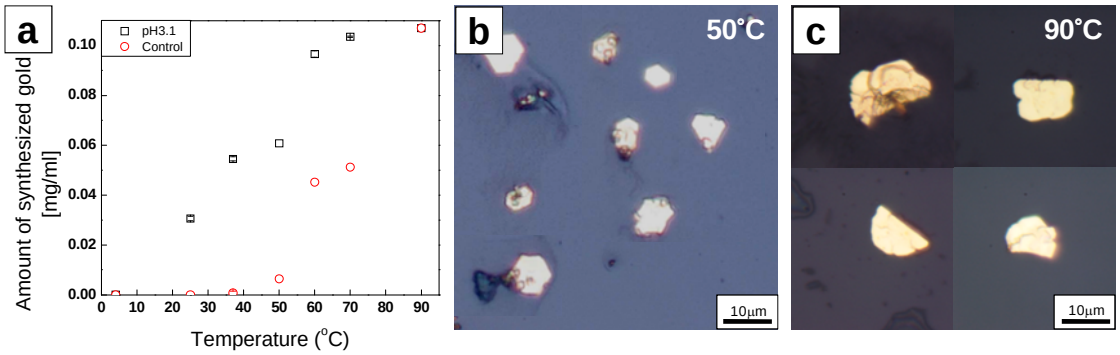

Figure 3.16 The amount of synthesized gold from the sets of experiments where the temperature was varied from 4 to 90°C. The composition of the reaction solution was 0.5mM $HAuCl_4$ and 0.18mM glycine at pH3.1, and no glycine was added to the controls (a). Optical images of the synthesized gold nanoplatelets at 50°C (b) and 90°C (c).

3.3.6. Transient Kinetics

Time dependent changes in the structural and quantitative characteristics of the synthesized gold nanostructures were studied. The time courses of the amount of synthesized gold (figure3.17(a)) at pH 3.0, 4.1 and 4.8 follow a characteristic sigmoidal shape which suggests the involvement of autocatalysis[48,49]. Previous studies of Wang's group showed systematic approach to the synthesis of gold nanostructures using aspartic acid[17]. In their time course of UV-Vis absorbance evolution, which can be considered identical to the amount of synthesized gold as a function of time, they have divided the sigmoidal curve into three regions: (a) the induction period, where the amount of synthesized gold remains low and visibly unchanged, (b) the growth period, where the amount of synthesized gold undergoes the most rapid changes, and (c) the termination period, where the amount of synthesized gold reaches to a plateau value. Overall, in figure 3.17, no induction period could be observed which could be due to the appearance

of the induction region before three hours. Rapid increase in the amount of synthesized gold was observed in the range of 3~24 hours, in figure 3.3.16a, for pH 3.0, 4.1 and 4.8 which suggests the growth of nanostructures, and finally reached to plateau after 24hours indicating the termination of the reaction. However the amount of synthesized gold for pH 7.0 gradually increased until 72 hours of reaction which might reach to plateau after a longer period of reaction. The set of experiment for pH 10.4 reached to a plateau value in the first 6 hours. The earlier termination of reaction before the growth of the structures in pH10.4 could be correlated to the nanoparticle structures synthesized at this pH which hardly involve any extensive growths.

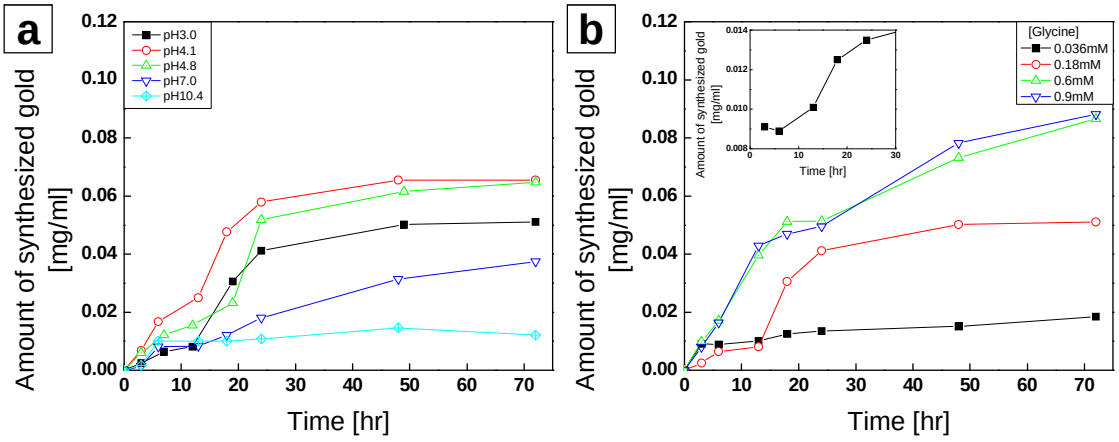

Figure 3.17 Amount of synthesized gold as a function of time for the sets of experiments where the variables were the pH (a), the concentration of glycine (b) and the concentration of $HAuCl_4$ (c).

The time courses of the amount of synthesized gold at pH 3.1 with different amount of glycine, in figure 3.17(b), shows a characteristic sigmoidal shape for the glycine concentration of 0.036 and 0.18mM only with growth and termination periods as

described previously. In contrary, the sets of experiments with 0.6 and 0.9mM of glycine showed sharp increases of the amount of synthesized gold starting from 3 hours to 18hours of reactions which might be due to the faster growth of the structures in short period of time with existence of sufficient amount of glycine in the solutions.

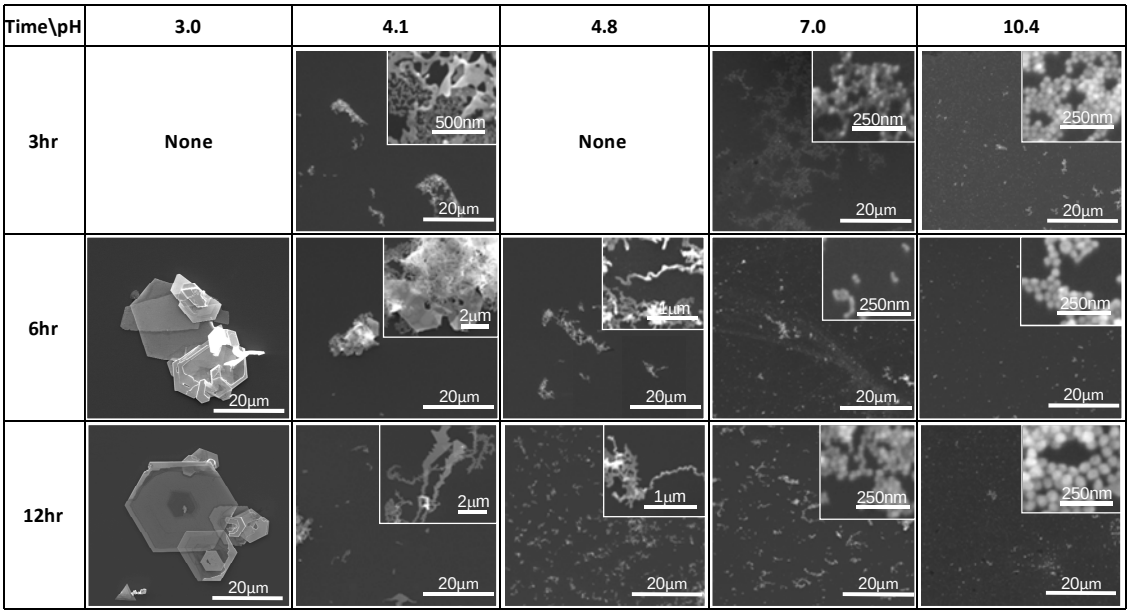

Figure 3.18 SEM images of the gold nanostructures synthesized by incubation of 0.5mM $HAuCl_4$ with 0.18mM of glycine at pH3.0, 4.1, 4.8, 7.0 and 10.4 at 37^{o}C. Structures could be hardly observed after three hours of incubation for pH3.0 and 4.8.

Figure 3.18 shows the structures observed by SEM after 3, 6 and 12hours of incubation of 0.5mM of $HAuCl_4$ and 0.18mM of glycine at different pH. The structures in the batch of pH3.0 were grown into relatively much larger structures than those at different pH. The structures from pH 4.1 showed the most structural variation. Particle

and irregular wire structures were observed after 3hours of incubation, wide ribbon and aggregated wire structures after 6hours and nanoribbon structures with a small platelet as a head after 9hours of incubation. Aggregated wires were consistently observed from the reactions terminated after 6 and 12hours at pH4.8, but the amount of the structures were increased. Particles structures synthesized at pH7.0 and pH10.4 showed no structural changes after 3, 6 and 12 hours of incubation. However, the growth of the particles could be visually confirmed.

3.3.7. Electron Transport Properties

The electron-transport properties at nanoscale are significantly challenged by the scattering of electrons on the surfaces and by the reflection of the electrons at the grain boundaries of the nanostructures. Accordingly, polycrystalline 1-dimensional (1D) nanostructures have higher resistivity values than the values of materials in bulk. Moreover, the current density that the polycrystalline 1D nanostructures can stand is considerably lower than bulk materials, and it precipitously decreases at the diameters below 60nm as a result of electromigration[50-52]. Single crystalline nanostructures are attractive candidates for nanoelectronnics in these respects because of the absence the grain boundaries implying significant improvements of the conductivities in nanoscale[19].

To understand the characteristics of metallic conduction in single crystalline gold nanostructures, temperature coefficient of resistivity (TCR) and room temperature resistivity were studied. Nanoribbons were in particular interest due to their versatile utility as interconnects and as sensing elements for nanoelectronic devices. Before the

electrical measurements, gold nanoribbons in different dimensions were aligned across microfabricated interdigitated gold electrodes, with gap width of 3~5μm, using AC electric field[25]. The temperature dependent electrical properties of the gold nanostructures were measured from 300K to 10K with applied current of ±2nA. Low range of currents was used to avoid failure current that creates gap as a result of electromigration[53]. The TCR values of the nanostructures were calculated using

$$TCR = \frac{1}{R_O}\frac{\Delta(R - R_O)}{\Delta(T - T_O)} \qquad \text{Eq. (5),}$$

where R is the resistance at temperature, T, and R_0 is the resistance at T_0, which was 300 K.

Theoretical predictions of the resistivity of metallic nanowires with rectangular cross-sentions can be estimated by the equation derived from Fuchs-Sondheimer[54,55] and Mayadas-Shatzkes[56] theories by Steinhogl and co-workers:

$$\rho = \rho_0 \left\{ \frac{1}{3} \Big/ \left[\frac{1}{3} - \frac{\alpha}{2} + \alpha^2 - \alpha^3 \ln\left(1 + \frac{1}{\alpha}\right) \right] + \frac{3}{8} C(1-p) \frac{1+AR}{AR} \frac{\lambda}{w} \right\} \text{ with } \alpha = \frac{\lambda}{d} \frac{R}{1-R} \quad \text{Eq. (6),}$$

where ρ is the measured wire resistivity, ρ_0, the temperature-dependent bulk resistivity of the metal, d, grain diameter, w, the nanowire width, AR, the aspect ratio of height to width, C, a geometrical parameter which is 1.2 for nanowires with rectangular cross-section, and, λ, the electron mean free path which is 50nm at 300K. The specularity

parameter, p, was adapted from Fuchs-Sondheimer theory[54,55] which is the fraction of surface scattering events preserved momentum, and R, the reflectivity coefficient from Mayadas-Shatzkes[56] theory which is the fraction of electrons scattered by the potential barriers at grain boundaries.

Block-Grüneisen equation was used to predict the bulk resistivity (ρ_0) of metal:

$$\rho(T) = C\frac{T^5}{\Theta^6}\int_0^{\frac{\Theta}{T}}\frac{x^5 dx}{(e^x-1)(1-e^{-x})} \qquad \text{Eqn. (7),}$$

where Θ is Debye temperature of metal which is 165K in case of gold, C is a constant that varies with respect to the kind of metals (C_{Au} = 9.0 x 10^{-6} $\Omega m^{-1}K$).

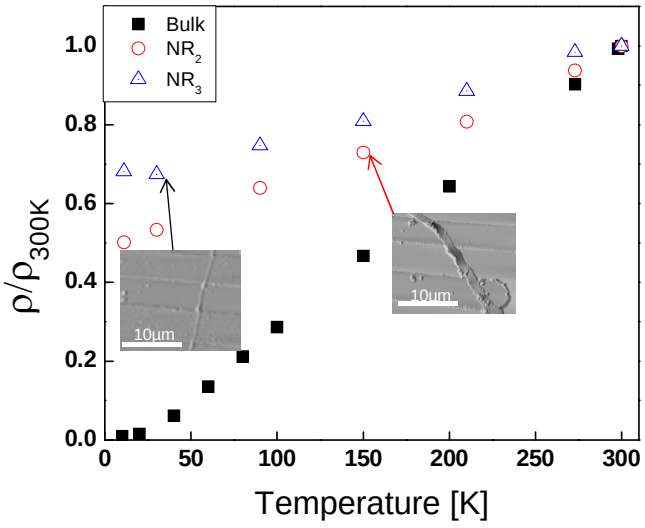

Figure 3.19 Normalized resistivity of single-crystalline gold nanowire(△,H 31.5nm x W 0.25μm, L3.67μm 0.0014 K^{-1}), nanoribbon (○, H 67.0nm x W 1.38μm, L6.66μm, 0.0019 K^{-1}), and bulk gold (■, 0.0036K^{-1}) as a function of temperature.

Positive values of TCR were observed for a single nanoribbon and a nanowire in figure3.19, which support the metallic conduction through the nanoribbon. The normalized electrical resistivity of the nanoribbon, nanowire and bulk gold show that the disparity between the structures increases as the temperature decreases, as reported for nanowires in previous studies[57,58]. The TCR values of the nanoribbons (NR_2 $0.0019K^{-1}$; NR_3 $0.0014K^{-1}$) were distinctively smaller than the value of bulk gold ($0.0036K^{-1}$), and considerably larger than the values of NR_a and NR_b which were reported by Penner's group[59]. Generally, such discrepancy in the TCR values associates with the diminutive sizes of the structures, where the electron scattering on the ribbon surfaces[54,55] and the reflection of the electrons at grain boundaries[56] contribute to the resistivity of the nanostructures. In our case, surface scattering of the electrons could be the major contribution to the resistivity since there are no grain boundaries in the nanoribbons. Thus NR_2 and NR_3 showed significantly smaller TCR values than bulk gold due to diminutive dimensions of the structures, and larger TCR values than NR_a and NR_b due to the absence of grain boundaries. The TCR values of NR_2 and NR_3 also differ from each other because of the significant differences in their thickness and width.

Source	Name	Thickness x Width	Length (um)	Grain diameter (nm)	Crystallinity	ρ (10^{-8}Ωm)		TCR (K^{-1})	Configuration
						Experimental	Calculated		
CRC handbook	Bulk	-	-	-	Poly	2.3	-	0.0036	-
Penner et al.	NR_a	20nm x 233nm	400	100-20	Poly	20.5	18.7-77.3	0.00041	4 probe
	NR_b	100nm x 166nm	400	100-20	Poly	7.8	17.7-76.2	0.0010	4 probe
Our work	NR_1	29.5nm x 398nm	5.51	-	Single	3.3	3.4	-	4 probe
	NR_2	67.0nm x 1.38um	6.66	-	Single	-	2.9	0.0019	4 probe
	NR_3	31.5nm x 250nm	3.67	-	Single	3.2	3.4	0.0014	4 probe

Table 3.1 Compared electron transport properties for gold nanoribbons (NR) and nanowires (NW).

The room temperature resistivity of the nanoribbon and the nanowires were measured in four probe configuration to correct the contact resistance[27]. Previously, Penner's group has studied the electron transport properties of polycrystalline gold nanoribbons in different dimensions[59]. Polycrystalline gold and single crystalline gold in bulk have little difference in their room temperature resistivity[60]. However, in such diminutive structures, where the electron scattering on the surface and the grain boundary become the major contribution to the resistivity, it appears that the resistivity of polycrystalline and single crystalline have larger difference than those in bulk. Comparing NR_a and NR_3 which are in comparably similar dimensions, the resistivity values show significant disparity where the resistivity value is much higher in polycrystalline gold nanoribbon than it in single crystalline nanoribbon. Such disparity of the resistivity can be reasoned for more dominant contribution of the electron scattering on the grain boundaries than on the surface in diminutive structures, thereby the structural dimensions can much less influence the resistivity of gold nanoribbons without the presence of grain boundaries. Theoretically predicted resistivity was calculated in the same way as the calculations of

Penner's group[59] using the equation derived from Fuchs-Sondheimer[55,56] and Mayadas-Shatzkes[56] theories, and Block-Grüneisen equation. Theoretically calculated resistivity for single crystalline nanoribbon ($3.4x10^{-8}$ Ωm) shows similar values to experimentally measured values (3.3, $3.2x10^{-8}$ Ωm) indicating the reasonable prediction of the size effect on nanostructures by the reported theories.

3.3.8. Gas Sensing Properties

3.3.8.1. Nanoribbon Based Sensor

The application of a single nanoribbon as a gas sensor has been studied to demonstrate the utility of the single crystalline nanoribbons in terms of electrical stability. A single nanoribbon aligned across interdigitated gold electrode by AC electric field was used as both sensing element and transducer for hydrogen sulfide (H_2S). It has been reported that H_2S strongly adsorbs on gold surface and forms gold-sulfur bonds which lowers the surface work function of gold, thereby increases the resistivity[61-63].

Figure 3.20 shows the response of the sensor (NR_1) to 50 and 100ppm of H_2S at room temperature where 0.5mV of constant voltage was applied in 2 probe configuration. The resistance of the sensor increased as H_2S was induced and decreased as dry air was induced for purging. The time for the recovery was much slower than it for the response, thus the baseline could not be fully recovered during the measurement. Although the sensing result of the gold nanoribbon is not as encouraging as the previous studies using gold nanoparticles[61-63] or gold-decorated conducting polymer[63], the electrical endurance

of the gold nanoribbon as an element of a nanodevice can be a satisfactory property for more appropriate applications.

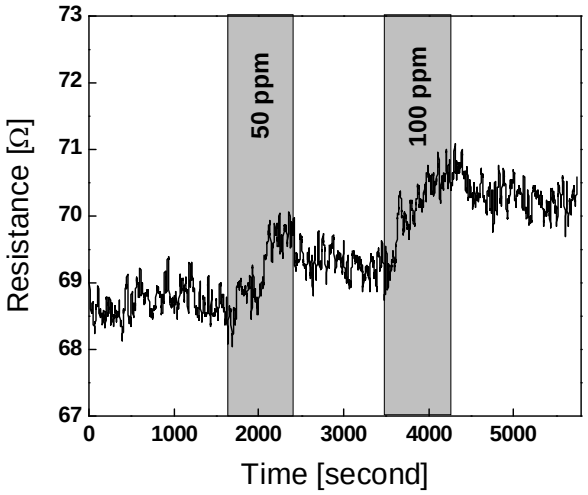

Figure 3.20 Sensor response to 50 and 100ppm H_2S at room temperature for a single crystalline gold nanoribbon. The dark bands indicate the exposure of the sensor to the analyte gas.

3.3.8.2. Nanoparticle Based Sensor

As a different approach to H_2S sensing, gold nanoparticles were used as sensing elements and also as a transducer to demonstrate the sensing properties. The nanoparticles used for this study was synthesized in 0.5mM $HAuCl_4$, 0.18mM glycine at pH10.4, 37°C for three days, and the average diameter was 48±2nm. The gold electrodes were 200μm wide with a 3μm gap in which configuration was reported to form numbers of nanoparticle chains in between gold electrodes with high preservation of the individual nanoparticles[26]. The alignment of the nanoparticles by electric field has sensitive dependence on the frequency of the applied electric field[64]. Thus the optimum frequency for the nanoparticle alignment was studied in a range of 0.1~1MHz at $16V_{pp}$. The

frequency dependence on the alignment of nanoparticles was observed using SEM is presented in figure3.21. The numbers of the nanoparticle chains were significantly high in 100kHz, and dramatically reduced as the frequency was increased to 1MHz (figure3.21 (a~c)). In most of the cases, parallel arrays of gold nanoparticle chains (figure3.21(d)) were observed which are ultimately connected through 1~2 nanoparticles with many nanoparticles sustaining the structure. A few cases of aligned nanoparticles at 1MHz showed low ranges of resistance near 1kΩ. In the SEM images of these samples (figure3.21(e)), a single nanoparticle chain was observed in between the electrode gap in which the nanoparticles were fused to each other. The fusion of nanoparticle occurred due to the high current flowing through one nanoparticle chain, and eventually reduced the resistance of the chain by forming a nanowire.

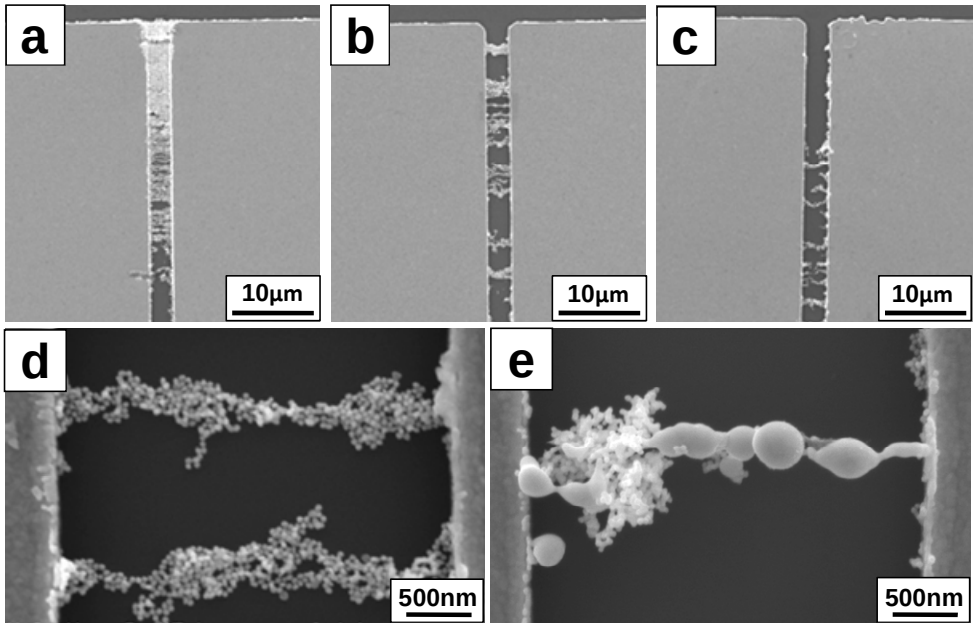

Figure 3.21 SEM images of AC aligned nanoparticles at 100kHz (a), 500kHz (b) and 1MHz (c) at low magnification. Multiple numbers of aligned nanoparticles were observed without fusing and forming larger particles (d) while the nanoparticles in a single chain

fused into neighboring particles and formed larger particles during the alignment process (e).

As a result, the ranges of the resistances for gold nanoparticles increased as the numbers of nanoparticle chains decreased due to the reduced numbers of conduction pathways (figure3.22). Based on the observed results of the frequency dependence of nanoparticle alignments, the samples aligned at 1MHz with high resistance range was chosen for the gas sensing expecting high sensitivity towards H_2S due to lesser numbers of nanoparticle chains.

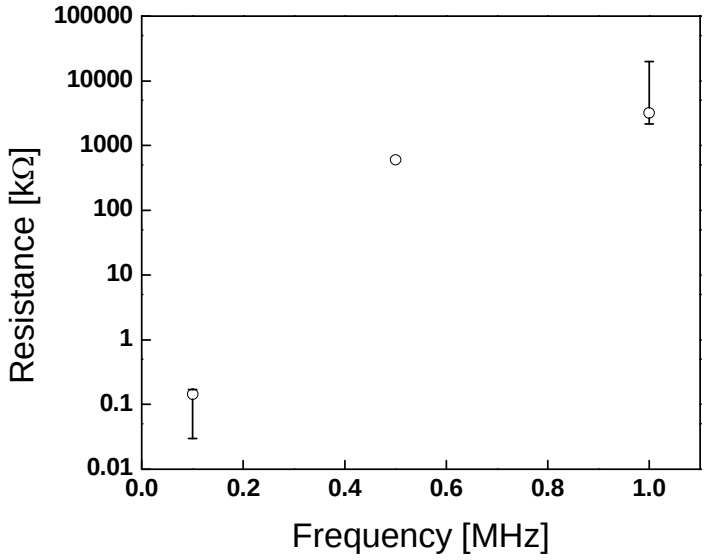

Figure 3.22 The correlation of the resistance and the frequency on the alignment of gold nanoparticles.

Previously, there have been many studies on the electronic transport properties of gold nanoparticles. Most of the studies used gold nanoparticles coated with a layer of thiolated molecules to assemble and to enhance the Coulomb blockade effect between

gold nanoparticles[65]. Such coating of thiolated molecules saturates the surface of gold nanoparticles with Au-S bonding by forming self-assembled monolayer, thereby limits the utility of gold nanoparticles towards the detection of sulfur compounds. However, with an assistance of electric field, functionalization of gold nanoparticles with organic layer was not necessary in this study. The temperature dependent electron transport properties in figure 3.23(a) show the resistance of the nanoparticles increasing as the temperature decreases which is opposite to general metallic materials. Such behavior indicates the hopping of electron from one nanoparticle to another, which requires certain amount of energy to occur. The activation energy of the nanoparticle chains were 2.75meV which was calculated from the Arrhenius plot in figure 3.23(b). The average activation energy from three samples was 2.49meV with a variation of 0.37meV. The value of our activation energy is smaller than those of gold nanoparticles coated with thiolated molecules at least by an order of magnitude[66,67] which could be due to closer distances of uncoated nanoparticles than those of thiol-coated nanoparticles.

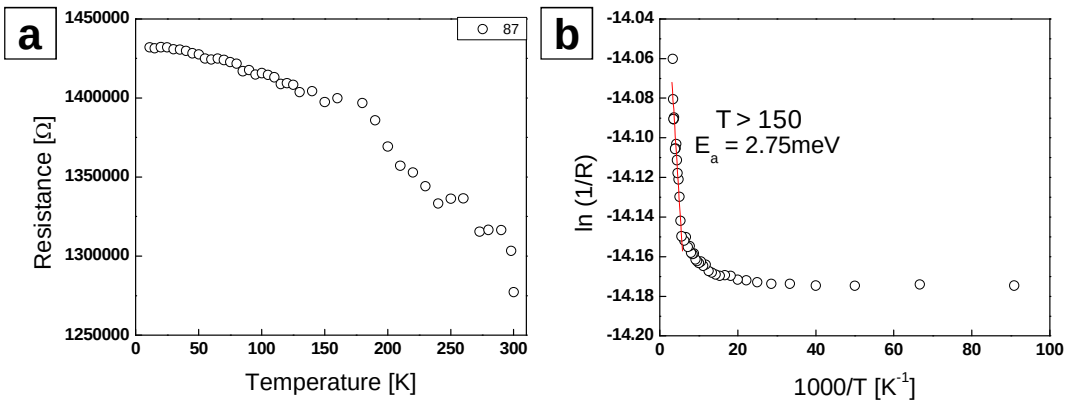

Figure 3.23 Temperature dependence of resistance (a) and the Arrhenius plot (b) of the AC aligned nanoparticles.

Figure3.24 shows the electrical responses of the gold nanoparticle chains to various concentrations of H_2S at room temperature. The resistance of the nanoparticle chains increased immediately upon exposure to H_2S gas, and decreased instantly after purging the system with dry air. Such dramatic changes in the resistance of the gold nanoparticle chains indicate significantly sensitive changes in the hopping of electrons due to the adsorption and desorption of H_2S molecules on gold resulting in fast response and recovery less than half a minute. The increase of the resistance reaches to the sensor's high detection limit after 2ppm of H_2S due to the saturation of H_2S molecules on the gold surface.

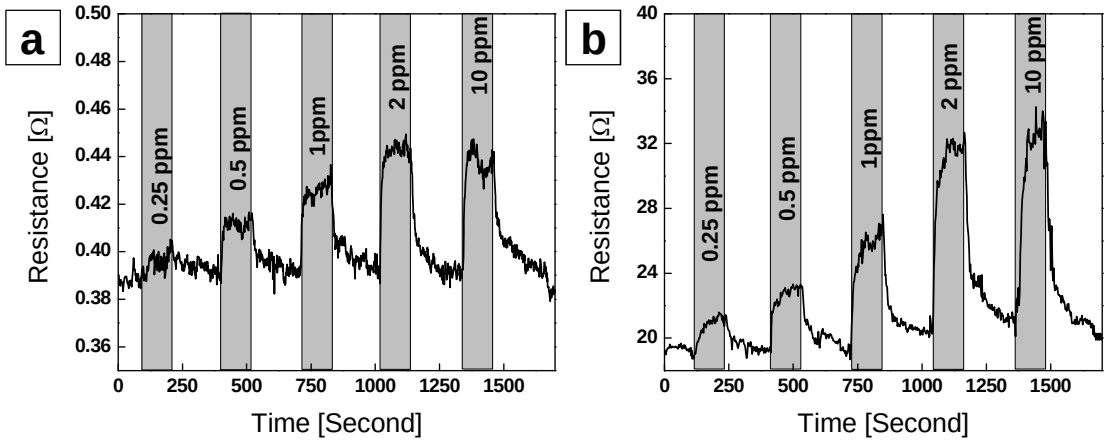

Figure 3.24 Resistance versus time in the presence of various concentrations (0.25, 0.5, 1, 2 and 10ppm) of H_2S gas. The resistance ranges of the AC aligned nanoparticles were 0.4MΩ (A) and 20M Ω (B). The dark bands indicate the exposure of H_2S to the sensor and dry air was purged for the rest of the time.

The sensitivity of the nanoparticle sensor has shown large difference with respect to the resistance. Higher resistance from gold nanoparticle chains can indicate lesser

numbers and more discrete structures of the chains without fusion. Thus the resistance of the sensor could be strongly related to the sensitivity where lower detection limit can be expected due to more sensitive changes of electron transports in the same amount of analyte gas. In fact, the sensitivity of the sensor was dramatically increased when the resistance was increased from 0.4MΩ to 20MΩ which is compared in figure3.25. Such improvement in the sensitivity encourages the development of sensors with a detection limit near a few ppb if the range of the resistance for the sensor was chosen wisely.

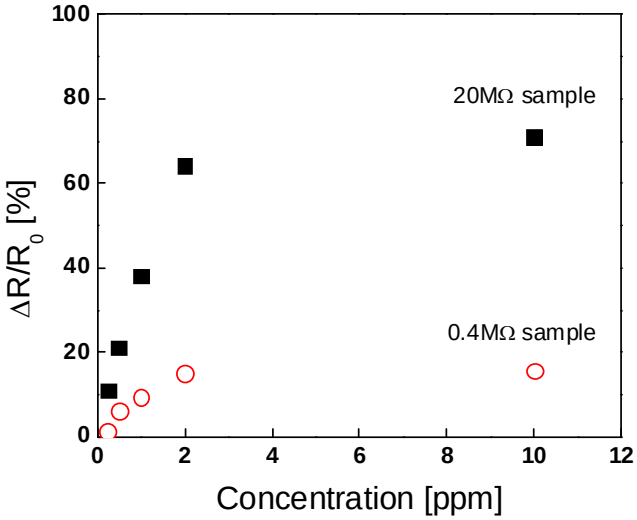

Figure 3.25 Sensor response to 50 and 100ppm H_2S at room temperature for a single crystalline gold nanoribbon. The dark bands indicate the exposure of the sensor to the analyte gas.

3.3.9. Electrochemical Analysis

The synthesis of gold nanostructures can be described as a process, which involves with electron transfer occurring between gold complexes and glycine resulting in reductions of gold as an electrochemical reaction. The reduction of gold complexes by

glycine was studied in electrochemical point of view to understand the synthesis process of gold nanostructures. The standard reduction potentials for each species existing in the $HAuCl_4^-H_2O$ system were calculated by Nernst equation with the values of standard reduction potential of $AuCl_4^-$ reported by Bjerrum[68], the Gibbs free energy of formation of gold complexes reported by Machesky et al.[69]. The Gibbs free energy of formation was used to calculate the Gibbs free energy of reaction of gold complexes which lead to the calculation of standard reduction potentials of each gold complex using equation (8).

$$\Delta G^0 = -nFE^0 \qquad \text{Eqn. (8),}$$

Reactions	E° vs NHE 25°C (V)	Reference
$AuCl_4^- + 3e^- = Au^0 + 4Cl^-$	0.994	[68]
$Au(OH)Cl_3^- + 3e- = Au^0 + OH^- + 3Cl^-$	0.879*	[69]
$Au(OH)_2Cl_2^- + 3e^- = Au^0 + 2OH^- + 2Cl^-$	0.775*	[69]
$Au(OH)_3Cl^- + 3e^- = Au^0 + 3OH^- + Cl^-$	0.678*	[69]
$Au(OH)_4^- + 3e^- = Au^0 + 4OH^-$	0.591*	[69]

Table3.2 Standard reduction potentials of gold complexes. *Calculated from Gibbs free energy of formation reported by Machesky et al.[69] and the equilibrium constants reported by Baes et al.[43].

The calculated reduction potentials in table3.2 and thermodynamic equilibrium constants of gold complexes reported in table3.3 were adapted into Nernst equation (equation (9)) to estimate the changes of gold complex species and the corresponding reduction potentials at different range of pH.

$$E = E^0 - \frac{RT}{nF}\ln\frac{[Red]}{[Ox]} \qquad \text{Eqn. (9),}$$

Reactions	Log K	Reference
$AuCl_4^- + OH^- = Au(OH)Cl_3^- + Cl^-$	8.1	[43]
$Au(OH)Cl_3^- + OH^- = Au(OH)_2Cl_2^- + Cl^-$	7.17	[43]
$Au(OH)_2Cl_2^- + OH^- = Au(OH)_3Cl^- + Cl^-$	6.11	[43]
$Au(OH)_3Cl^- + OH^- = Au(OH)_4^- + Cl^-$	5.66	[43]
$AuCl_4^- + Gly = AuCl_3Gly^-$	7.05	[70]
$AuCl_3Gly^- + Gly = AuCl_2Gly_2^-$	3.52	[70]

Table3.3 Thermodynamic equilibrium constants of gold complexes reported by Baes et al.[43] and Farooq et al.[70].

As a result of the calculations with equation (9), an E_h-pH diagram (figure 3.26) was constructed for the $HAuCl_4$-H_2O system with exclusion of Au(I) species which hardly exists in mild condition of $HAuCl_4$-H_2O system[71]. The diagram shows the stable species of gold complexes at different ranges of pH, which occupy domains at fairly high potential region. Unlike other species, $Au(OH)_4^-$ becomes more unstable as the pH increases to 14.

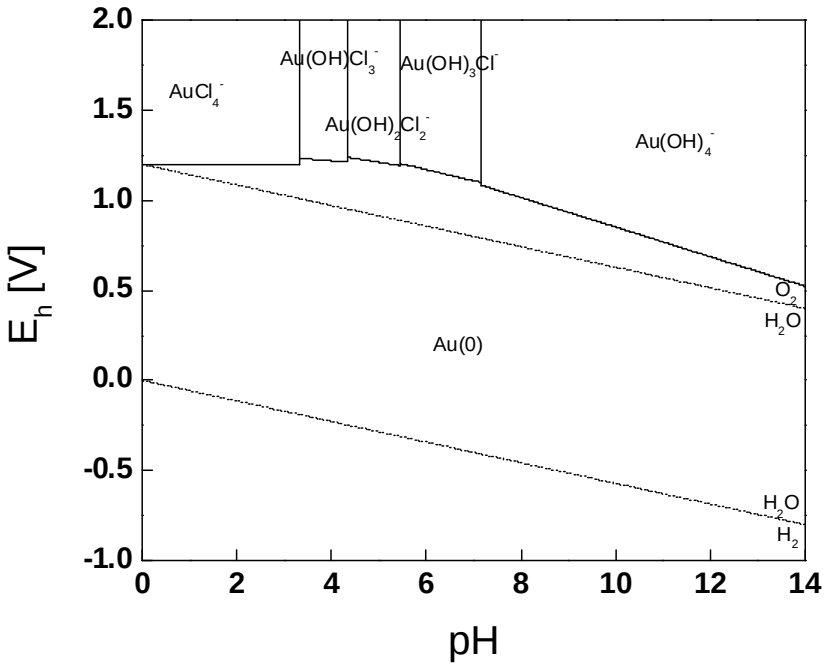

Figure 3.26 E_h-pH diagram for $HAuCl_4$-H_2O system at 37°C and 0.5mM dissolved species. Au(I) species are not considered.

Figure 3.27 shows voltammograms recorded at pH 3.0, 5.0, 7.0 and 10.0 of 0.5mM $HAuCl_4$ solution with presence and absence of 0.9mM glycine. Larger amount of glycine was used for LSV studies than the standard experimental condition used in previous studies to enhance the electrochemical observation in voltammograms. The voltammograms showed the appearance of the reduction waves moving towards negative potentials as the pH of the solution was increased. The shifting of the reduction waves indicates the changes of gold complex species in the solutions of which reduction potential decreases as the hydrolysis proceeds. The voltammograms of the solutions with presence of glycine showed significant disparities compared to those with absence of

glycine. Such disparity could be due to the formation of gold-glycine complex formation as previously reported by Zou et al.[45] and Farooq et al.[70]. Refer to the positive equilibrium constant listed in table 3.3, it could be estimated that the complex of glycine and $AuCl_4^-$ would have more negative reduction potential than $AuCl_4^-$. In fact, an additional negative reduction wave could be observed in the voltammograms at pH3.0 with presence of glycine which could be ascribed as the reduction wave of gold-glycine complex. However, the equilibrium constants and reduction potentials of other gold complexes and glycine have rarely been reported, thereby the reason for disparity of voltammograms in 0.5mM $HAuCl_4$ with presence and absence of 0.9mM glycine could not be concluded. The limiting currents at pH 3.0 and 10.0 showed similar values independent of the presence of glycine. The limiting currents observed at pH5.0 and 7.0 showed significant discrepancies in their values when the glycine was added to the solutions.

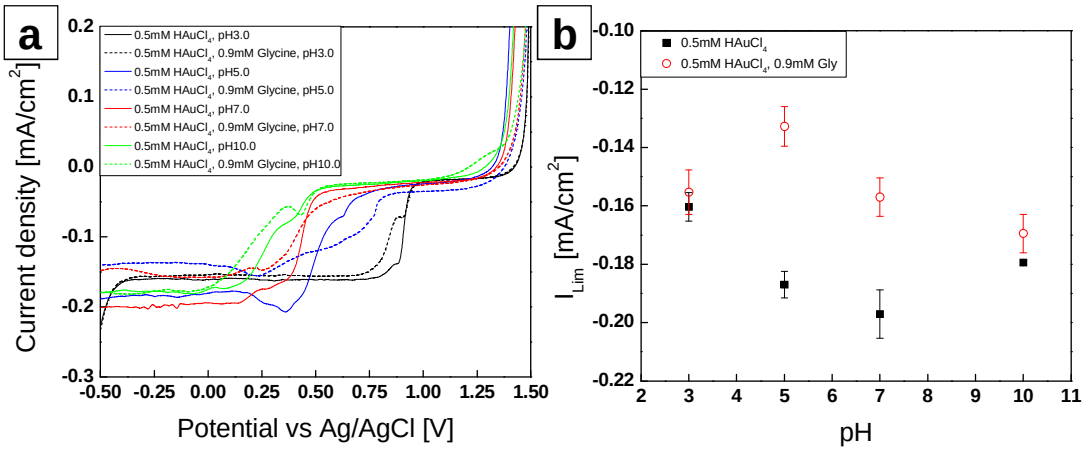

Figure 3.27 Voltammograms (a) and limiting currents (b) observed for 0.5mM $HAuCl_4$ with presence and absence of 0.9mM glycine at pH3.0, 5.0, 7.0 and 10.0.

The voltammograms in figure 3.28 showed significant disparities of the curves with respect to the presence and absence of glycine. The appearance of the reduction waves for every concentration was observed nearly at the same location that supports the correlation of the gold complex species and the location of reduction waves described in the previous paragraph. The limiting current was comparably increased with presence of glycine, and the quantitative disparity was increased proportional to the concentration of $HAuCl_4$. It could be observed that glycine plays important role in the electrochemical reduction of gold complexes resulting in major changes in the electrochemical behavior of limiting currents. However, more information and systematic studies on the electrochemical relationship between gold complexes and glycine should be followed to understand the reduction mechanism.

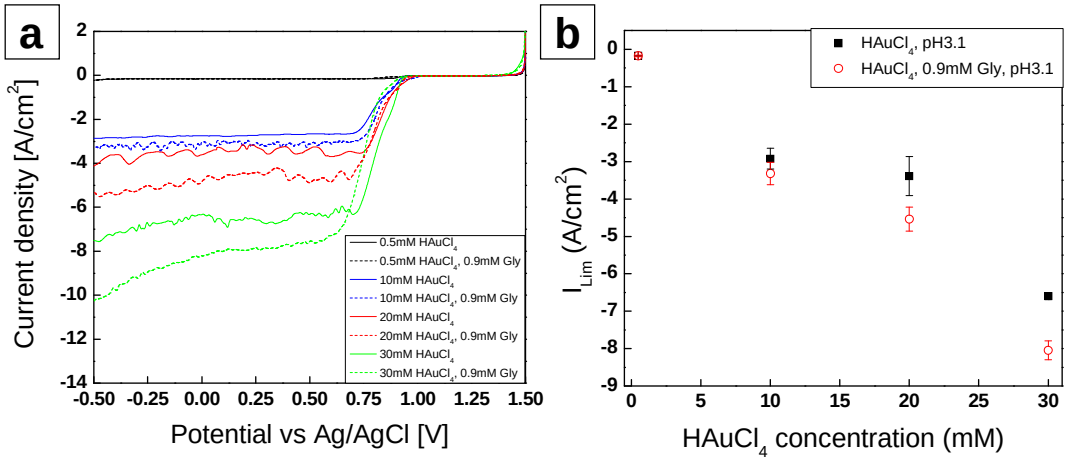

Figure 3.28 Voltammograms (a) and limiting currents (b) observed for 0.5, 10, 20 and 30mM $HAuCl_4$ with presence and absence of 0.9mM glycine at pH3.1.

3.4. Conclusion

The effect of the speciation of gold complex resulted by the changes of pH, excessive amount of chloride, and concentration of $HAuCl_4$ on the structural architectures was demonstrated in biological synthetic process of using glycine as reducing and capping agents. The gold nanoplatelets were synthesized in the solvent condition where $AuCl_4^-$ was predominant, and nanokites and nanoribbons were synthesized in the solvent of predominant species of $Au(OH)Cl_3^-$ and $Au(OH)_2Cl_2^-$, respectively. Gold nanoparticles were synthesized in the solutions of predominant $Au(OH)_3Cl^-$ and $Au(OH)_4^-$. Structural characterization confirmed the single crystallinity of the gold nanoplatelets, nanokites and nanoribbons grown along (111) plane. The amount of synthesized gold reached the highest in the region of predominant $AuCl_4^-$ and $Au(OH)Cl_3^-$ species, and it gradually decreased as the gold complexes were more hydrolyzed. Relatively higher amount of synthesized gold was observed in the unprotonated region of zwitterionic glycine than the protonated zwitterionic glycine suggesting the assistance of electrostatic interaction of anionic gold complexes to positively charged glycine at pH below 6.

The role of glycine as reducing and capping agent was confirmed by studying the structural changes of gold nanostructures in different concentration of glycine. The amount of synthesized gold increased as the concentration of glycine was increased indicating the raise of available electrons in the reaction due to larger amount of glycine induced. The primary structures of nanoplatelets, nanokites, nanoribbons and nanoparticles synthesized at 0.036mM glycine remained very close to what was observed in 0.18mM glycine. However the additional kinks and branches growth on and by the

primary structures could be observed for nanoplatelets, nanokite and nanoribbons at 0.9mM glycine solution. The irregular structures of nanoparticles synthesized in $Au(OH)_3Cl^-$ predominant region at 0.036 and 0.18mM glycine comparably improved the uniformity of the nanoparticles at 0.9mM glycine.

The temperatures above 37°C showed reduction of gold complex even with absence of glycine. The structures of the nanoplatelets synthesized became more irregular at higher temperatures indicating the loss of capping ability of glycine at such high temperature and uncontrollability of the crystal growth without appropriate capping agent.

Transient kinetic studies showed the sigmoidal characteristics of time evolution curves indicating autocatalytic nature of the reactions. Increase of the glycine concentration considerably increased the growth of structures in the first 15 hours of reaction. The formation of fully grown gold nanoplatelets was found after 6 hours of reaction whereas the formation of nanokites and nanoribbons took longer period time to observe fully grown structures. Significant growths of nanoparticles could be observed in the reaction time between 3 to 12 hours.

Temperature dependent resistivity of nanoribbon structures showed distinct decrease of their TCR values as the sizes of the structures decreased. Compared to polycrystalline gold nanoribbon in similar dimension, single crystalline gold nanoribbon showed considerably lower resistivity and higher TCR value indicating the significant improvement of conductivity by the absence of grain boundaries.

The H_2S gas sensing studies of AC aligned single crystalline gold nanoribbon showed the stable endurance with continuous applied voltage; however the sensitivity and the low detection limit are not as comparable as other type of gas sensors. Nanoparticles were also employed for the gas sensing application. The alignment of nanoparticles by AC electric field showed strong frequency dependence of the electric field. Numerous amounts of nanoparticles were aligned in between two gold electrodes at 100kHz, and the numbers of aligned nanoparticle chains was gradually decreased as the frequency was increased to 500kHz and 1MHz. The resistance of nanoparticles was the highest when aligned at 1MHz and the lowest when aligned at 100kHz due to different numbers of conduction pathways. The nanoparticle chains aligned at 1MHz showed non-metallic behavior for temperature dependent resistivity, and had activation energy of 2.49±0.37meV. The H_2S gas sensing results of gold nanoparticle chains show fast response and recovery less than half a minute indicating sensitive changes in the electron hopping. The gold nanoparticle sensors were not adequate for high concentrations of H_2S above 2ppm. The sensitivity of the nanoparticle sensors shows much higher values for the sample with higher resistance indicating more sensitive response with lesser numbers of nanoparticle chains.

The E_h-pH diagram was constructed to determine the potential and pH region of the domain of stable gold complex species. LSV studies ascertained the negative shift of reduction potentials as the hydrolysis of gold complexes proceeds. Large disparity was observed in the limiting currents with presence and absence of glycine which could be reasoned as the formation of gold-glycine complex.

3.5. References

(1) Priyabrata, M.; Absar, A.; Deendayal, M.; Satyajyoti, S.; Sudhakar, R. S.; Mohammad, I. K.; Ramani, R.; Renu, P.; Ajayakumar, P. V.; Mansoor, A.; Murali, S.; Rajiv, K. *Angewandte Chemie International Edition* **2001**, *40*, 3585-3588.

(2) Klaus, T.; Joerger, R.; Olsson, E.; Granqvist, C. G. *Proceedings of the National Academy of Sciences of the United States of America* **1999**, *96*, 13611-13614.

(3) Kowshik, M.; Deshmukh, N.; Vogel, W.; Urban, J.; Kulkarni, S. K.; Paknikar, K. M. *Biotechnology and Bioengineering* **2002**, *78*, 583-588.

(4) Cunningham, D. P.; Lundie, L. L. *Applied and Environmental Microbiology* **1993**, *59*, 7-14.

(5) Kowshik, M.; Vogel, W.; Urban, J.; Kulkarni, S. K.; Paknikar, K. M. *Advanced Materials* **2002**, *14*, 815-818.

(6) Labrenz, M.; Druschel, G. K.; Thomsen-Ebert, T.; Gilbert, B.; Welch, S. A.; Kemner, K. M.; Logan, G. A.; Summons, R. E.; De Stasio, G.; Bond, P. L.; Lai, B.; Kelly, S. D.; Banfield, J. F. *Science* **2000**, *290*, 1744-1747.

(7) Lovley, D. R.; Stolz, J. F.; Nord, G. L.; Phillips, E. J. P. *Nature* **1987**, *330*, 252-254.

(8) Gardea-Torresdey, J. L.; Parsons, J. G.; Gomez, E.; Peralta-Videa, J.; Troiani, H. E.; Santiago, P.; Yacaman, M. J. *Nano Letters* **2002**, *2*, 397-401.

(9) Shankar, S. S.; Rai, A.; Ankamwar, B.; Singh, A.; Ahmad, A.; Sastry, M. *Nat Mater* **2004**, *3*, 482-488.

(10) Chandran, S. P.; Minakshi, C.; Renu, P.; Absar, A.; Murali, S. *Biotechnology Progress* **2006**, *22*, 577-583.

(11) Xie, J.; Lee, J. Y.; Wang, D. I. C.; Ting, Y. P. *Small* **2007**, *3*, 672-682.

(12) Liu, B.; Xie, J.; Lee, J. Y.; Ting, Y. P.; Chen, J. P. *The Journal of Physical Chemistry B* **2005**, *109*, 15256-15263.

(13) Brown, S.; Sarikaya, M.; Johnson, E. *Journal of Molecular Biology* **2000**, *299*, 725-735.

(14) Slocik, J. M.; Stone, M. O.; Naik, R. R. *Small* **2005**, *1*, 1048-1052.

(15) Naik, R. R.; Stringer, S. J.; Agarwal, G.; Jones, S. E.; Stone, M. O. *Nat Mater* **2002**, *1*, 169-172.

(16) Shao, Y.; Jin, Y.; Dong, S. *Chemical Communications* **2004**, 1104-1105.

(17) Tan, Y. N.; Lee, J. Y.; Wang, D. I. C. *The Journal of Physical Chemistry C* **2008**, *112*, 5463-5470.

(18) Huang, L.; Zhang, Y.; Guo, Z.; Gu, N. *Chinese Science Bulletin* **2009**, *54*, 1626-1629.

(19) Wang, C.; Hu, Y. J.; Lieber, C. M.; Sun, S. H. *Journal of the American Chemical Society* **2008**, *130*, 8902-+.

(20) Wang, J.; Wang, Z. *Materials Letters* **2007**, *61*, 4149-4151.

(21) Lim, B.; Camargo, P. H. C.; Xia, Y. *Langmuir* **2008**, *24*, 10437-10442.

(22) Kan, C.; Wang, G.; Zhu, X.; Li, C.; Cao, B. *Applied Physics Letters* **2006**, *88*, 071904-3.

(23) Armendariz, V.; Herrera, I.; peralta-videa, J. R.; Jose-yacaman, M.; Troiani, H.; Santiago, P.; Gardea-Torresdey, J. L. *Journal of Nanoparticle Research* **2004**, *6*, 377-382.
(24) Rai, A.; Singh, A.; Ahmad, A.; Sastry, M. *Langmuir* **2006**, *22*, 736-741.
(25) Smith, P. A.; Nordquist, C. D.; Jackson, T. N.; Mayer, T. S.; Martin, B. R.; Mbindyo, J.; Mallouk, T. E. *Applied Physics Letters* **2000**, *77*, 1399-1401.
(26) Kretschmer, R.; Fritzsche, W. *Langmuir* **2004**, *20*, 11797-11801.
(27) Walton, A. S.; Allen, C. S.; Critchley, K.; Gorzny, M. L.; McKendry, J. E.; Brydson, R. M. D.; Hickey, B. J.; Evans, S. D. *Nanotechnology* **2007**, *18*, 6.
(28) Daniel, M. C.; Astruc, D. *Chemical Reviews* **2004**, *104*, 293-346.
(29) Murphy, C. J.; San, T. K.; Gole, A. M.; Orendorff, C. J.; Gao, J. X.; Gou, L.; Hunyadi, S. E.; Li, T. *Journal of Physical Chemistry B* **2005**, *109*, 13857-13870.
(30) Huang, X.; El-Sayed, I. H.; Qian, W.; El-Sayed, M. A. *Journal of the American Chemical Society* **2006**, *128*, 2115-2120.
(31) Nikoobakht, B.; El-Sayed, M. A. *Chemistry of Materials* **2003**, *15*, 1957-1962.
(32) Swami, A.; Kumar, A.; Selvakannan, P. R.; Mandal, S.; Pasricha, R.; Sastry, M. *Chemistry of Materials* **2003**, *15*, 17-19.
(33) Zhao, N.; Wei, Y.; Sun, N.; Chen, Q.; Bai, J.; Zhou, L.; Qin, Y.; Li, M.; Qi, L. *Langmuir* **2008**, *24*, 991-998.
(34) Pei, L. H.; Mori, K.; Adachi, M. *Langmuir* **2004**, *20*, 7837-7843.
(35) Lim, B.; Camargo, P. H. C.; Xia, Y. *Langmuir* **2008**, *24*, 10437-10442.
(36) Liz-Marzan, L. M. *Langmuir* **2005**, *22*, 32-41.
(37) Schultz, D. A. *Current Opinion in Biotechnology* **2003**, *14*, 13-22.
(38) Sun, Y.; Xia, Y. *The Analyst* **2003**, *128*, 686-691.
(39) Schofield, C. L.; Haines, A. H.; Field, R. A.; Russell, D. A. *Langmuir* **2006**, *22*, 6707-6711.
(40) El-Sayed, M. A. *Accounts of Chemical Research* **2001**, *34*, 257-264.
(41) Nechayev, Y. A.; Nikolenko, G. V. *Geochemistry International* **1986**, *23*, 32-37.
(42) Switzer, R.; Garrity, L. *Experimental biochemistry: theory and exercises in fundamental methods*; 3rd ed.; W. H. Freeman, 1999.
(43) Charles F. Baes, J.; Mesmer, R. E. *The Hydrolysis of Cations*; John Wiley & Sons, Inc: Canada, 1976.
(44) Newman, J. D. S.; Blanchard, G. J. *Langmuir* **2006**, *22*, 5882-5887.
(45) Zou, J.; Guo, Z. J.; Parkinson, J. A.; Chen, Y.; Sadler, P. J. *Chemical Communications* **1999**, 1359-1360.
(46) Murphy, P. J.; LaGrange, M. S. *Geochimica Et Cosmochimica Acta* **1998**, *62*, 3515-3526.
(47) Lee, J.-H.; Kamada, K.; Enomoto, N.; Hojo, J. *Crystal Growth & Design* **2008**, *8*, 2638-2645.
(48) Boudart, M. *Kinetics of Chemical Processes*; Prentice Hall: Englewood Cliffs, New Jersey, 1968.
(49) Huang, Z. Y.; Mills, G.; Hajek, B. *The Journal of Physical Chemistry* **1993**, *97*, 11542-11550.

(50) Durkan, C.; Schneider, M. A.; Welland, M. E. *Journal of Applied Physics* **1999**, *86*, 1280-1286.
(51) Aherne, D.; Satti, A.; Fitzmaurice, D. *Nanotechnology* **2007**, *18*, 6.
(52) Karim, S.; Maaz, K.; Ali, G.; Ensinger, W. *Journal of Physics D: Applied Physics* **2009**, *42*, 5.
(53) Xiang, C. X.; Kim, J. Y.; Penner, R. M. *Nano Letters* **2009**, *9*, 2133-2138.
(54) Fuchs, K. *Proceedings of the Cambridge Philosophical Society* **1938**, *34*, 100-108.
(55) Sondheimer, E. H. *Advances in Physics* **1952**, *1*, 1-42.
(56) Mayadas, A. F.; Shatzkes, M. *Physical Review B* **1970**, *1*, 1382-&.
(57) Durkan, C.; Welland, M. E. *Physical Review B* **2000**, *61*, 14215-14218.
(58) De Marzi, G.; Iacopino, D.; Quinn, A. J.; Redmond, G. *Journal of Applied Physics* **2004**, *96*, 3458-3462.
(59) Menke, E. J.; Thompson, M. A.; Xiang, C.; Yang, L. C.; Penner, R. M. *Nature Materials* **2006**, *5*, 914-919.
(60) Fischer, W.; Geiger, H.; Rudolf, P.; Wissmann, P. *Applied Physics* **1977**, *13*, 245-253.
(61) Cui, X.; Freitag, M.; Martel, R.; Brus, L.; Avouris, P. *Nano Letters* **2003**, *3*, 783-787.
(62) Schonenberger, C.; Jorritsma, J.; Sondaghuethorst, J. A. M.; Fokkink, L. G. J. *Journal of Physical Chemistry* **1995**, *99*, 3259-3271.
(63) Shirsat, M. D.; Bangar, M. A.; Deshusses, M. A.; Myung, N. V.; Mulchandani, A. *Applied Physics Letters* **2009**, *94*, 3.
(64) Gierhart, B. C.; Howitt, D. G.; Chen, S. J.; Smith, R. L.; Collins, S. D. *Langmuir* **2007**, *23*, 12450-12456.
(65) Zamborini, F. P.; Leopold, M. C.; Hicks, J. F.; Kulesza, P. J.; Malik, M. A.; Murray, R. W. *Journal of the American Chemical Society* **2002**, *124*, 8958-8964.
(66) Brust, M.; Bethell, D.; Kiely, C. J.; Schiffrin, D. J. *Langmuir* **1998**, *14*, 5425-5429.
(67) Hardy, N. J.; Hanwell, M. D.; Richardson, T. H. *Journal of Materials Science-Materials in Electronics* **2007**, *18*, 943-949.
(68) Bjerrum, N. *Bulletin Des Societes Chimiques Belges* **1948**, *57*, 432-445.
(69) Machesky, M. L.; Andrade, W. O.; Rose, A. W. *Geochimica Et Cosmochimica Acta* **1991**, *55*, 769-776.
(70) Farooq, O.; Ahmad, N. *Journal of Electroanalytical Chemistry* **1974**, *53*, 457-460.
(71) Pan, P.; Wood, S. A. *Geochimica Et Cosmochimica Acta* **1991**, *55*, 2365-2371.

Chapter 4: Amino acid - Mediated Synthesis of Gold Nanostructures

4.1 Introduction

Amino acids have important functions as building blocks of biomolecules and as nutrients in metabolism. Recently, amino acids have been given another important role as a reducing and capping agent for the synthesis of gold nanostructures[1-5]. So far, aspartic acid[1,2,4], arginine[1,3], cysteine[5], lysine[1], tryptophan[1] and tyrosine[1,3] have been used in a few studies ascribing the feasibility of amino acid-mediated synthesis to produce various kinds of gold nanostructures. In the previous chapter, the effect of various reaction conditions in amino acid-mediated synthesis of gold nanostructures was demonstrated using glycine as reducing and capping agent due to the structural simplicity. Glycine is the smallest molecule of amino acids which can be considered as the fundamental form of amino acids. Each amino acid has distinct chemical structures and properties from each other, and such chemical differences might play a significant role in the formation of gold nanostructures. Therefore, in this chapter, the focus of study was on understanding the effect of using different amino acids on the synthesis of gold nanostructures. The effect of various reaction conditions on the synthesis process has also been demonstrated as an effort to understand the reduction properties of each amino acid.

4.1.1 Properties of Amino Acids

Twenty amino acids are consisted of an amine group and a carboxyl group in common, and an additional side chain (R) with different chemical structures between different amino acids varies the characteristics of each amino acid. The chemical

structures and properties of twenty amino acids are listed in table 4.1 and 4.2. Twenty amino acids are often categorized into a few groups based on the polarity and chemical structures of the side chains. Based on the chemical structures of the side chains of amino acids, twenty amino acids can be classified into seven groups which are aliphatic, aromatic, cyclic, carboxyl, hydroxyl, amide, amine and sulfur-containing functional groups.

Aliphatic functional group includes amino acids with hydrocarbon side chains which can be listed as glycine, alanine, valine, leucine and isoleucine. The amino acids with aliphatic side chains are in nonpolar and hydrophobic nature where the hydrophobicity increases as the number of carbon atoms in the hydrocarbon chain increases. Even though glycine is generally classified as aliphatic functional group, glycine has the simplest structure among all the amino acids which contains no side chains. The isoelectric points of aliphatic amino acids are centered between the pK_a values of α-carboxyl and α-amino groups which is near pH 6.00 with minute variations.

Proline is the only cyclic amino acid which is also known as imino acid due to the structural difference of the amine group on α-carbon forming a cyclic structure with δ-carbon. Nonetheless of such structural difference from the other amino acids, proline shares many properties with the aliphatic group. Proline is a nonpolar molecule with an isoelectric point of pH 6.30 which is similar to aliphatic amino acids.

Carboxyl functional group is known as acidic amino acid group due to the acidity of carboxyl group. A second carboxyl group is attached on aspartic acid and glutamic acid as a side chain where aspartic acid and glutamic acid contain one and two methylene

groups, respectively. Both amino acids are in polar and hydrophilic nature. The isoelectric point of aspartic acid (pH 2.85) and glutamic acid (pH 3.15) is lower than any other amino acids due to the contribution of ionizable carboxyl side chain. Amide functional group is often described together with carboxyl functional group due to the similarities in side chain structures where asparagine and glutamine are the amides of aspartic acid and glutamic acid, respectively. Amide functional side chains are polar, hydrophilic and not ionizable. Thus, the isoelectric points of asparagine (pH 5.41) and glutamine (pH 5.65) are determined by the pKa of α-carboxyl and α-amino group. Asparagine is known to hydrolyze converting asparagine into aspartic acid with ease, and glutamine is easily converted into proline.

Hydroxyl functional group includes serine and threonine; however tyrosine is also often classified as hydroxyl amino acid due to the hydroxyl group attached on an aromatic ring. Threonine contains an additional methyl group on the β-carbon of serine. Structurally serine and threonine have similar structures to alanine and valine except the replacement of a hydroxyl group with a methyl group. Serine and threonine are polar and hydrophilic molecules, and the isoelectric points are pH 5.68 and 5.60, respectively.

Aliphatic, carboxyl, amide and hydroxyl amino acids have high similarities between the amino acids in the same group. The differences of each amino acid in aliphatic, carboxyl, amide and hydroxyl group can be found in the numbers of carbon atoms or in the structural differences of hydrocarbon chains. However, aromatic, amine and sulfur-containing amino acids share similar properties, but the structural differences are more than the number or structural differences of carbon atoms.

Aromatic functional group contains amino acids incorporating side chains with aromatic ring in the structures. Phenylalanine contains a phenyl substituent on the β-carbon of alanine which can be inferred by the name of it. Tyrosine contains phenol group as a side chain which a derivative of phenylalanine hydroxylated on the para position. Tryptophan is the largest amino acid containing an indole group on the β-carbon. Phenylalanine and tryptophan are nonpolar, but tyrosine is polar due to the hydroxyl group in the side chain. The hydrophobicity of aromatic amino acid increases in the order of tyrosine, tryptophan and phenylalanine. The isoelectric points of aromatic amino acids also stay in the range of pH 5.50~5.90.

On the contrary of carboxyl group, amine functional group is known as basic group due to the basicity of amine group. Histidine has imidazole side chain which is an aromatic heterocyclic classified as an alkaloid. Lysine is consisted of four-carbon aliphatic chain and a ε-amino group as a side chain which contributes to increase the isoelectric point due to the highly reactive nature of amino group. Arginine has three-carbon aliphatic chain and a complex guanidinium group which is consisted of two primary amine and one secondary amine groups. Histidine, lysine and arginine are polar and hydrophilic, and their isoelectric points, especially, those of lysine (pH 10.79) and arginine (pH 12.48), are higher than any other amino acids.

Sulfur-containing functional group describes the amino acids containing sulfur in the structure of their side chains. Cysteine is consisted of a single-carbon aliphatic chain and a sulfur-hydrogen thiol group whereas methionine is consisted of two-carbon aliphatic chain, a thiol ether and a methyl group. The thiol group on cysteine ionizes to yield

thiolated anion and often forms a disulfide bond with another thiolated cysteine molecule. Cysteine and methionine are generally considered to be nonpolar and hydrophobic. The isoelectric point is lower for cysteine (pH 5.05) than methionine (pH 5.74) as a result of active contribution by thiol group in cysteine.

Table 4.1 Chemical structures and properties of aliphatic, cyclic, carboxyl, amide and hydroxyl amino acids.

Group	Amino Acid	Abbreviation	Chemical structure	Molecular weight (g/mol)	PI	pKa		
						α-carboxyl group	α-amino group	Side chain group
Aliphatic	Glycine	**G**	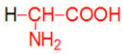	75	6.06	2.35	9.78	
	Alanine	**A**	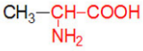	89	6.01	2.35	9.87	
	Valine	**V**	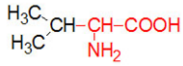	117	6.00	2.29	9.74	
	Leucine	**L**	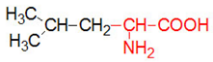	131	6.01	2.33	9.74	
	Isoleucine	**I**	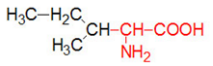	131	6.05	2.32	9.76	
Cyclic	Proline	**P**	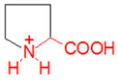	115	6.30	2.95	10.65	
Carboxyl	Aspartic acid	**D**	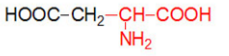	132	2.85	1.99	9.90	3.90
	Glutamic acid	**E**	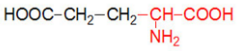	146	3.15	2.10	9.47	4.07
Amide	Asparagine	**N**	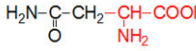	133	5.41	2.10	8.84	
	Glutamine	**Q**	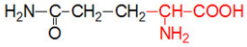	146	5.65	2.17	9.13	
Hydroxyl	Serine	**S**	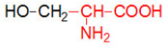	105	5.68	2.19	9.21	
	Threonine	**T**	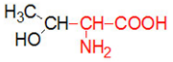	119	5.60	2.09	9.10	

Table 4.2 Chemical structures and properties of aromatic, amine and sulfur-containing amino acids.

Group	Amino Acid	Abbreviation	Chemical structure	Molecular weight (g/mol)	PI	pKa		
						α-carboxyl group	α-amino group	Side chain group
Aromatic	Phenylalanine	**F**	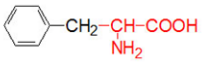	165	5.49	2.16	9.18	
	Tyrosine	**Y**	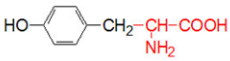	181	5.64	2.20	9.11	10.13
	Tryptophan	**W**	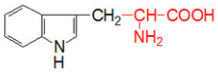	204	5.89	2.43	9.44	
Amine	Histidine	**H**	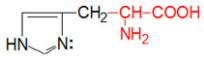	155	7.60	1.80	9.20	6.00
	Arginine	**R**	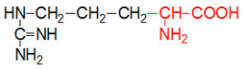	175	10.76	1.82	8.99	12.48
	Lysine	**K**	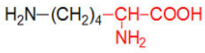	147	9.60	2.16	9.18	10.79
Sulfur-contating	Cysteine	**C**	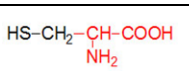	121	5.05	1.92	10.78	8.33
	Methionine	**M**	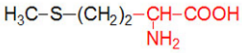	149	5.74	2.13	9.28	

4.2 Experimental Details

4.2.1 Materials

Hydrochloroauric acid ($HAuCl_4$) was purchased from Sigma Aldrich. Natural L form of alanine, arginine, asparagine, aspartate, cysteine, glutamine, glutamate, glycine, histidine, isoleucine, leucine, lysine, methionine, phenylalanine, proline, serine, threonine, tyrosine, tryptophan and valine, sodium chloride (NaCl), sodium hydroxide (NaOH), and hydrochloric acid (HCl) were purchased from Sigma-Aldrich and Fisher Chemicals. Nanopure water was prepared by using Milli-Q system and was sterilized before use.

4.2.2 Synthesis of Gold Nanostructures

The reaction volume of the solution was 1ml, where the final concentration of $HAuCl_4$ and amino acids were 0.5 and 0.18mM for standard experiments. The pH of 0.5mM $HAuCl_4$ solution is 3.0 initially and the pH for 4, 5, 7 and10 was adjusted with 5M of NaOH and 5M of HCl before adding amino acids to the solutions. The reaction solution was placed in dark environment at 37°C for three days without any disturbance.

After the reaction, the solution was centrifuged at 12,000rpm for 30minutes to separate the synthesized structures from the reaction solution. The supernatant was used for analyzing the amount of synthesized gold nanostructures, and the gold nanostructures remained in the bottom of the microcentrifuge tube were dispersed in nanopure water. Centrifugation and dispersion of gold nanostructures were repeated for three times to remove the gold ions from the solution.

4.2.3 Spectrophotometric Analysis

The supernatant of the reaction solution was diluted in 10% of HCl, and then the concentration of the remaining gold ions was analyzed with atomic absorption spectrophotometer (AAnalyst800, Perkin Elmer, Inc.) at flame mode. The measured concentration of remaining gold ions was subtracted from the initial gold concentration of the reaction solution to calculate the amount of synthesized gold.

The optical properties of the gold nanostructures dispersed in nanopure water were measured with UV-Vis spectrophotometer (DU800, Beckman Coulter, Inc.) in the range of wavelength from 400 to 1100nm.

4.2.4 Structural Characterization

Structural characteristics of the gold nanostructures were studied by using optical microscopy (KH-3000, Hirox, Inc.), scanning electron microscopy (SEM) and transmission electron microscopy (TEM). The gold nanostructures were prepared on a silicon wafer and were observed with SEM (XL30-FEG, Royal Philips Electronics, Inc.) at 15kV of accelerating voltage.

For TEM imaging, the gold nanostructures dispersed in nanopure water were deposited onto carbon-coated Cu support grids and dried in ambient condition. The structures were observed with TEM (JEM-2100F, JEOL, Ltd.) at an accelerating voltage of 200kV. Selected area electron diffraction (SAED) was utilized to study the crystallographic orientation of the gold nanostructures.

4.3 Results and discussions

In the previous chapter, among various reaction variables, the speciation of hydroxychloroaurate ($Au(OH)_xCl_{4-x}^-$) showed dominant effect of determining the structural features of gold nanostructures synthesized using glycine. The speciation of hydroxychloroaurate ions (figure 4.1) is highly dependent on the pH and the concentration of chloride of the reaction solutions which was correlated to seeing such structural changes at different pH. Herein, the effect of side chains on amino acid-mediated synthesis of gold nanostructures has been demonstrated at different ranges of pH and concentration of chloride to observe optical, structural and reductive changes by using different kind of amino acids. Glycine was considered as a control material which contains no side chains and was used to compare the properties of gold nanostructures synthesized by the other natural amino acids to understand the role of side chains on the synthesis process.

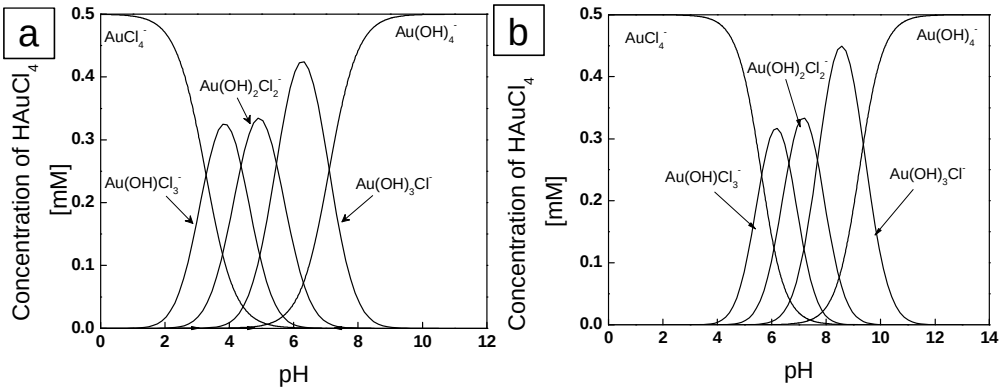

Figure 4.1 The concentration of different species of gold complexes in 0.5mM $HAuCl_4$ as a function of pH which was calculated with the equilibrium constants reported by Nechayev et al[6].

4.3.1 The Effect of Side Chains and pH

4.3.1.1. Aliphatic and Cyclic Functional Group

In this section, aliphatic and cyclic functional groups were studied together since proline shares many similar properties with aliphatic amino acids. The initial color of 0.5mM $HAuCl_4$ solution is light yellow at low pH and the color of solution becomes transparent as the pH increases to more than 6.0. Overall, the observed colors of as-synthesized gold nanostructures showed a general trend and similarity with respect to the pH of reaction solutions (figure 4.1). The colors of 0.5mM $HAuCl_4$ solutions at pH 3.1±0.01, which was initially light yellow, became transparent with shiny gold products settled down in the bottom after 3 days of incubation at 37°C with 0.18mM of each amino acid. The gold nanostructures synthesized at pH 4.1±0.04 were in light brown colors in which structures were more dispersible in water than those synthesized at pH 3.1±0.01; however the structures easily settled down in a few minutes indicating existences of large structures. The gold nanostructure suspensions showed greenish gray colors at pH 5.0±0.03 and blue, purple colors at pH 7.0±0.12. Pink colors could be observed for the suspension of gold nanostructures synthesized at pH 10.7±0.04 with aliphatic amino acids, and dark red color was observed for cyclic amino acid, proline. Such differences in the color transitions at each pH indicate the formations of gold nanostructures in different sizes and shapes.

Amino acid	pH				
	3.1±0.01	4.1±0.04	5.0±0.03	7.0±0.12	10.7±0.04
G	colorless				
A	colorless				
V	colorless				
L	colorless				
I	colorless				
P	colorless				

Figure 4.2 The photographs of as-synthesized gold nanostructures dispersed in water. The gold nanostructures were synthesized by incubation of 0.5mM $HAuCl_4$ + 0.18mM aliphatic and cyclic amino acids at pH 3.1±0.01, 4.1±0.04, 5.0±0.03, 7.0±0.12 and 10.7±0.04 for 3days at 37°C.

Measurements of optical properties were challenging for the structures synthesized at pH 3.1 and 4.1 due to the large structures which easily settled down in a short time. Thus, the optical properties were measured for the gold nanostructures synthesized at pH 5.0±0.03, 7.0±0.12 and 10.7±0.04. The UV-Vis spectra of gold nanostructures

synthesized at pH 5.0±0.03 with aliphatic and cyclic amino acids show similar trends to the spectra of 1-D gold nanostructures, such as nanowires, nanobelts and nanokites[7-10]. Clear broad absorption bands from 490nm to the Near-Infrared (NIR) region could be commonly observed for glycine, alanine, valine, isoleucine and proline. The absorbance of the spectrum for leucine was very low to show clear locations of bands, but the trend of increase of the absorbance from 480nm to NIR region could be confirmed by comparing the values of absorbance. The gold nanostructures synthesized at pH 7.0 show clear bands located near 550nm for alanine, leucine, isoleucine and proline, and relatively broader bands were observed for glycine and valine in the wavelengths of 544 and 547nm, respectively. Similarly, structures from pH 10.7 show clear sharp bands located near 530nm where the shapes of bands can be qualitatively related to the nature of nanoparticles.

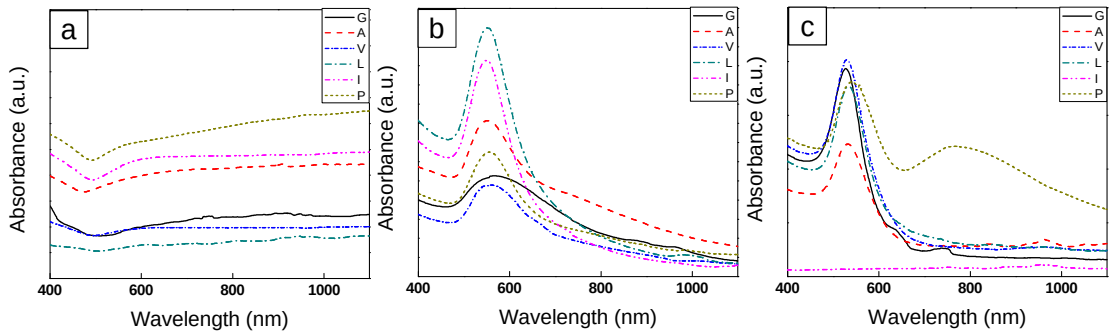

Figure 4.3 UV-Vis spectra of gold nanostructures synthesized at 0.5mM $HAuCl_4$ + 0.18mM aliphatic and cyclic amino acids at pH 5.0 (a), 7.0 (b) and 10.7 (c) for 3 days at 37°C.

The SEM and TEM images of synthesized gold nanostructures organized in figure 4.3 show a clear structural map of gold nanostructures which can be affected by two

variables of pH and side chains of amino acids. The images in vertical line shows the structural changes due to the differences of amino acids, and the horizontal line indicates structural changes due to the pH of the solutions. Since the side chain of aliphatic and cyclic group is not ionizable and reactive, structural differences due to side chains of amino acids were difficult to observe. However, distinctive changes could be observed due to the changes of pH. In general, nanoplatelets were synthesized at pH 3.0, nanokites at pH 4.1, nanoribbons at pH 5.0, and nanoparticles at pH 7.0 and 10.7. Slightly more structural variations could be observed for the structures synthesized at pH 4.1 and 5.0 than those of pH 3.1, 7.0 and 10.7 which might be due to the poor structural uniformity. As observed in the UV-Vis spectra, structures at pH 5.0 are dominantly in 1-D nanoribbon structures with little formation of nanoribbon networks. Nanoparticles synthesized at pH 10.7 are more uniform in their shape and sizes than those of pH 7.0 which corroborates the observation by UV-Vis spectra showing narrower bands for pH10.7 than pH 7.0. Comparing to the structures synthesized with glycine, which is an amino acid with fundamental structures containing no side chains, minor structural changes were observed in the gold nanostructures synthesized with the other amino acids in aliphatic and cyclic functional groups. This indicates that the side chains of aliphatic and cyclic amino acids are not in the center of the role to determine the structures of synthesized products.

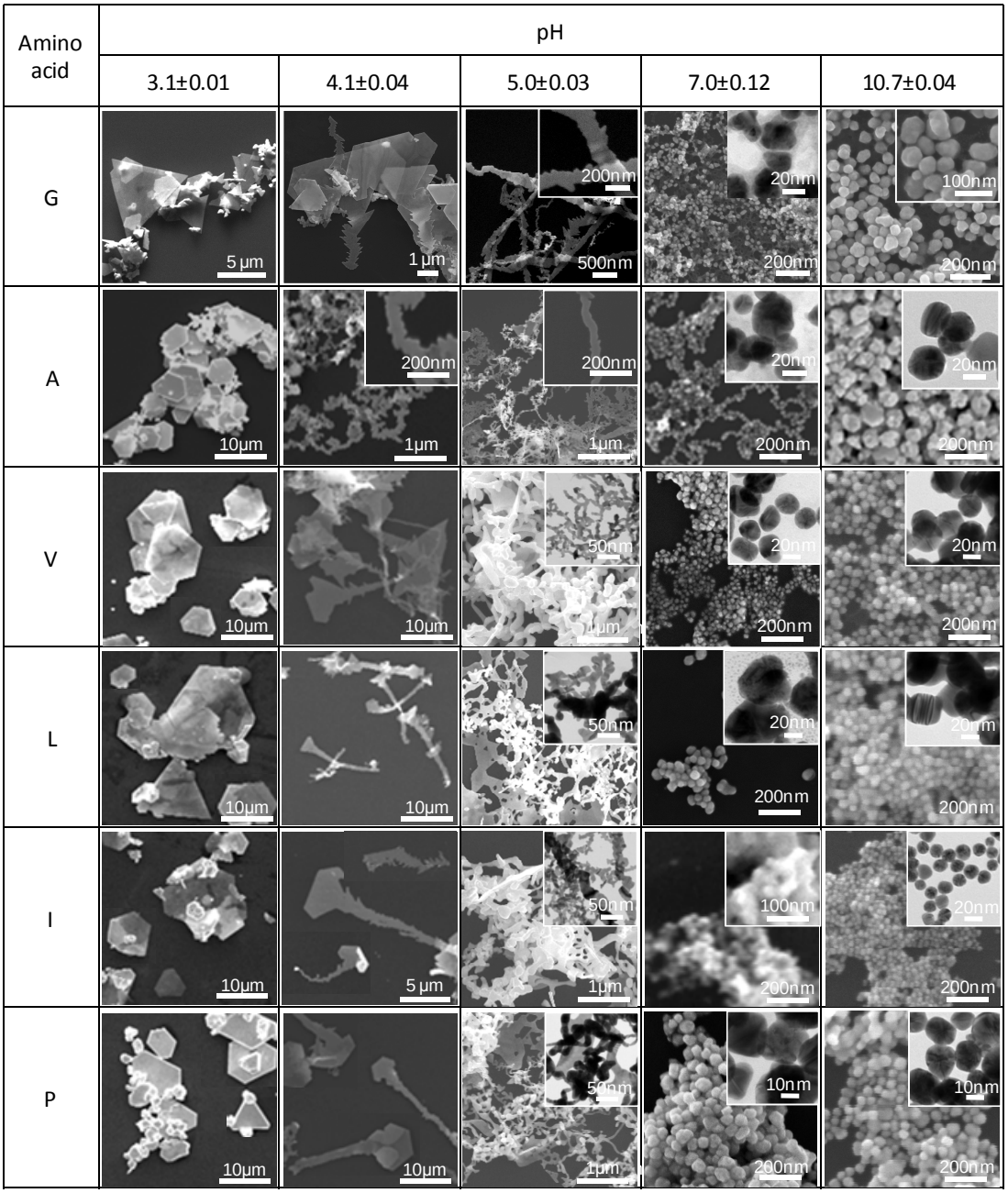

Figure 4.4 Tabulated SEM images and TEM images of gold nanostructures synthesized with 0.18mM aliphatic and cyclic amino acids in 0.5mM $HAuCl_4$ at different initial pH for three days at 37°C.

The amounts of synthesized gold with respect to the changes of pH are plotted in figure 4.4 for the six amino acids in aliphatic and cyclic functional group. For every amino acid, the amount of synthesized gold reaches its maximum around pH 4.8 where $Au(OH)_2Cl_2^-$ predominantly exists. The amount of synthesized gold significantly decreases above pH 8.0 in the case of using glycine, alanine and isoleucine; however, increased amount of the synthesized gold was observed in the same range of pH for valine, leucine and proline. The exact reason for such discrepancy is difficult to be explained. However, considering the speciation of hydroxychloroaurate ions in the solution (figure 4.1), valine, leucine and proline might be more interactive with $Au(OH)_4^-$ which is the predominant species at pH above 8.0. The ratio of maximum amount of synthesized gold to initial concentration of gold at pH4.85±0.05 for aliphatic amino acids were 57, 51, 55, 49, 52 and 64% for glycine, alanine, valine, leucine, isoleucine and proline, respectively. Within aliphatic group, the maximum amount of synthesized gold decreases with an addition of aliphatic chain compared to the value for glycine. The increased amount of synthesized gold at pH 4.8 for cyclic amino acid, proline, indicates higher reduction capability of proline than those of aliphatic amino acids.

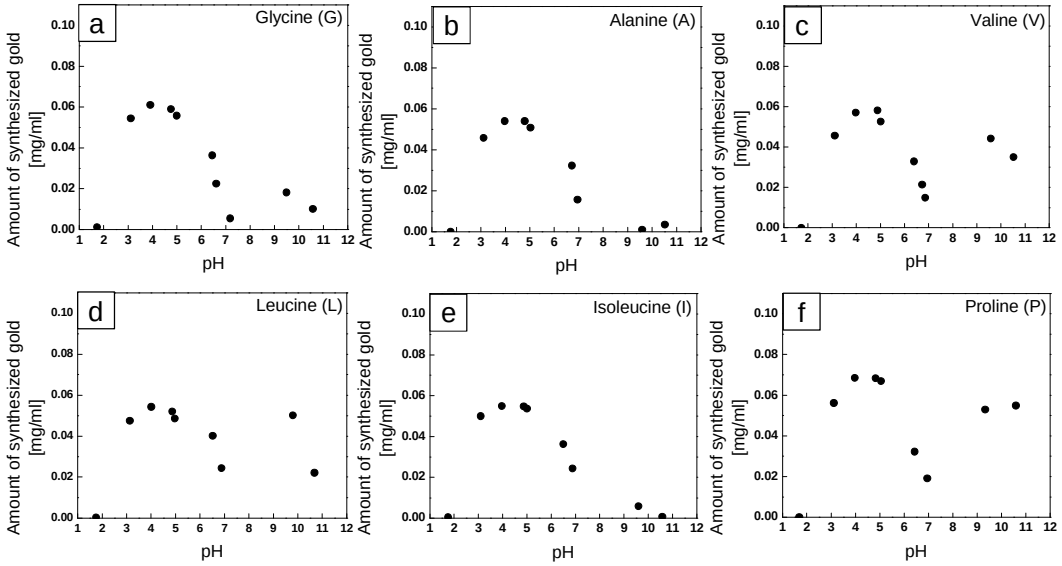

Figure 4.5 The total amount of synthesized gold after three days of incubation carried out with 0.5mM $HAuCl_4$ + 0.18mM aliphatic and cyclic amino acids at 37°C for different initial pH.

4.3.1.2. Carboxyl and Amide Functional Group

The colors of the gold nanostructure suspensions synthesized using carboxyl and amide amino acids are tabulated in figure 4.6. The as-synthesized gold nanostructures show transitions of colors from light brown, greenish gray, bluish purple to pink in general with respect to the change of pH from 4.0 to 10.5. Light variations could be observed for a few suspensions for aspartic acid and asparagine. The suspension colors of aspartic acid and asparagine at pH 4.0 and 5.0 showed slightly more green and brown colors, respectively, than those of glutamic acid and glutamine. The solutions of 0.5mM $HAuCl_4$ at pH 3.1 turned their color from yellow to transparent after 3 days of incubation at 37°C with 0.18mM of each amino acid and shiny gold products could be found which were settled down in the bottom of reaction bottle.

The UV-Vis spectra of gold nanostructures synthesized at pH 5.0, 6.5 and 10.5 show similar trends between aspartic acid and asparagine while glutamic acid and glutamine share similar spectral features. At pH5.0, the trend of UV-Vis spectra of glutamic acid and glutamine are close to those of the spectra of 1-D gold nanostructures showing broad absorption bands to the NIR region[7-10]. On the contrary, broad bands located near 570nm could be observed in the UV-Vis spectra of aspartic acid and asparagine at pH5.0 indicating different structural properties of the gold nanostructures synthesized with glutamic acid and glutamine. The gold nanostructures synthesized at pH 6.5 show clear bands located at 524, 536, 544 and 564nm for aspartic acid, glutamic acid, asparagine and glutamine, respectively. Clear sharp bands located near 520nm were observed for the gold nanostructures synthesized with aspartic acid, glutamic acid and asparagine at pH10.5 indicating existence of uniform nanoparticles. Optical properties could not be observed for the gold nanostructures synthesized with glutamine at pH 10.5 due to the low intensity of UV-Vis spectrum.

Amino acid	pH				
	3.1±0.02	4.0±0.06	5.0±0.04	6.5±0.01	10.5±0.01
G	colorless				
D	colorless				
E	colorless				
N	colorless				
Q	colorless				

Figure 4.6 The photographs of as-synthesized gold nanostructures dispersed in water. The gold nanostructures were synthesized by incubation of 0.5mM $HAuCl_4$ + 0.18mM carboxyl and amide amino acids at pH 3.1±0.01, 4.1±0.04, 5.0±0.03, 7.0±0.12 and 10.7±0.04 for 3days at 37°C.

Similarly to the trends observed in aliphatic and cyclic amino acids, the SEM and TEM images of synthesized gold nanostructures organized in figure 4.8 show major variations by the changes of pH and minor changes of structures depending on the changes of side chains in amino acids ascribing minor effects on the structural changes due to carboxyl and amide functional groups. Compared to the control material, glycine, similar structures of nanoplatelets were synthesized at pH 3.0, and nanoparticles were observed at pH 6.5 and 10.7. Glutamic acid and glutamine, which contain two methylene groups between the α-carbon and the functional groups, showed nanokite structures at pH

4.0 and nanoribbon structures at pH 5.0 coinciding with the structures observed for glycine at similar range of pH. Interestingly, aspartic acid and asparagine, which contain one methylene group between the α-carbon and the functional groups, showed flat irregular ribbon like structures at pH 4.0 and round irregular wire-like structures at pH 5.0. Based on the observations by SEM and TEM, the structures were more affected by the length of the hydrocarbon chains connecting the functional groups to the α-carbon rather than on the kind of functional group of carboxyl and amide. Nanoparticles synthesized at pH 6.5 and 10.5 by carboxyl and amide amino acids were more uniform in their shapes and sizes than those observed for glycine; however UV-Vis spectra showing narrower bands for pH 10.5 than pH 6.5 indicates possibly more uniformity of the nanoparticles synthesized at pH 10.5.

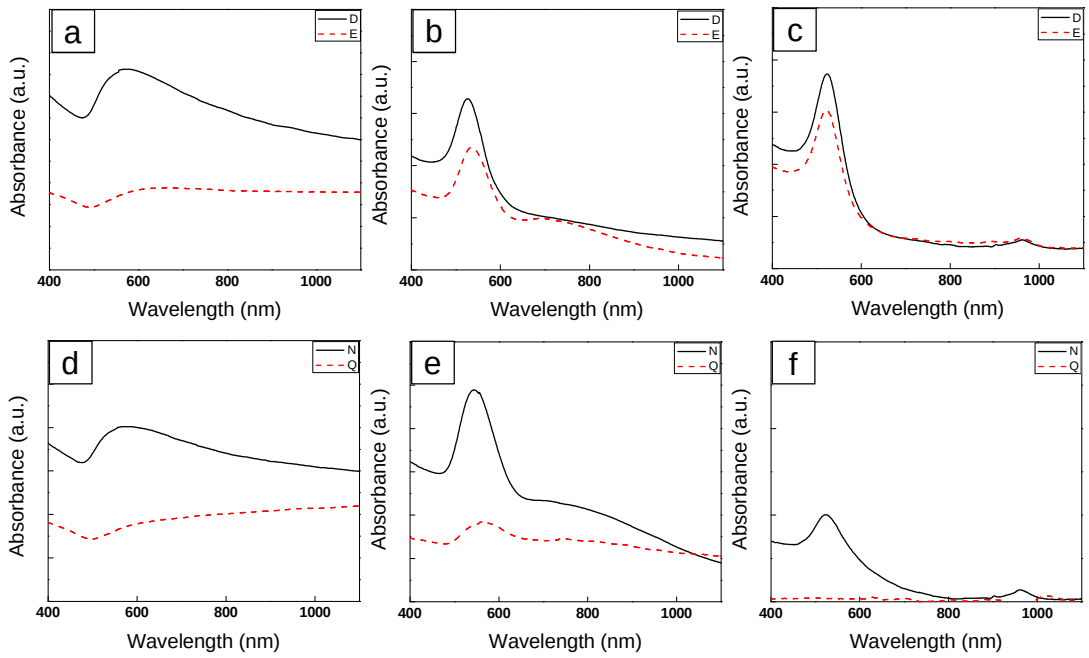

Figure 4.7 UV-Vis spectra of gold nanostructures synthesized at 0.5mM $HAuCl_4$ + 0.18mM carboxyl and amide amino acids at pH 5.0 (a, d), 6.5 (b, e) and 10.5 (c, f) for 3 days at 37°C.

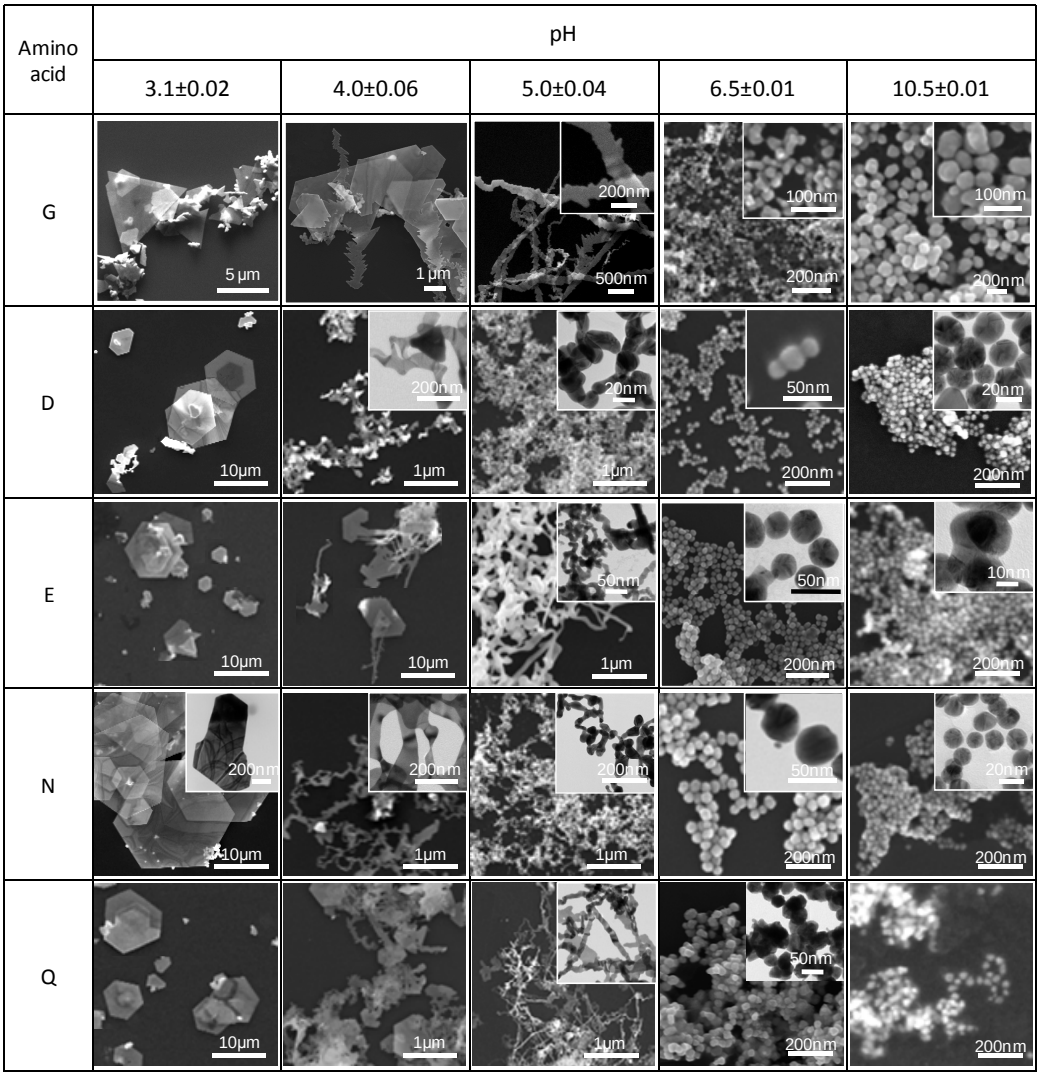

Figure 4.8 Tabulated SEM images and TEM images of gold nanostructures synthesized with 0.18mM carboxyl and amide amino acids in 0.5mM $HAuCl_4$ at different initial pH for three days at 37°C.

The reduction behavior of amino acid-mediated synthesis of gold nanostructures was plotted as the amount of synthesized gold versus pH. The amounts of synthesized gold reached the maximum values in the range of pH 4.0~5.0 for every amino acid in carboxyl and amide functional group which was in the same trend as glycine. The ratio of the

maximum amount of synthesized gold to the initial concentration of gold was 57% for glycine at pH 4.8, and similarly the ratio was 59% and 54% for glutamic acid and glutamine at pH 4.6 and 4.8 respectively. However, differently from glycine and the other carboxyl and amide amino acids, aspartic acid and asparagine showed more than 81% and 94% of the gold ions reduced at pH 4.7 and 4.9, respectively. Considering the structural differences observed for the gold nanostructures in the range of pH 4.0~5.0 for aspartic acid and asparagine, such structural changes might be affected by highly increased amount of synthesized gold which resulted increased numbers of structures with less structural maturity.

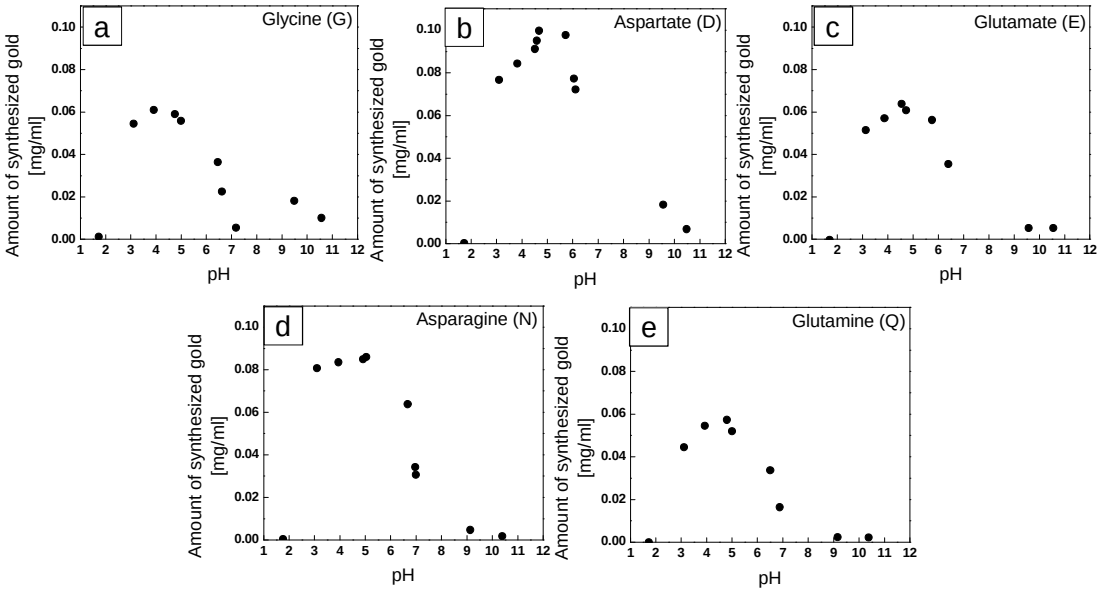

Figure 4.9 The total amount of synthesized gold after three days of incubation carried out with 0.5mM $HAuCl_4$ + 0.18mM carboxyl and amide amino acids at 37°C for different initial pH.

4.3.1.3. Hydroxyl Functional Group

The suspensions of gold nanostructures synthesized using hydroxyl amino acids showed similar color transitions to glycine (figure 4.10). The solutions at pH 3.1 with serine and threonine were transparent with shiny structures settled down in the reaction bottle after 3 days of incubation at 37°C with 0.18mM of each amino acid. The suspensions of gold nanostructures synthesized at pH 4.1, 5.0, 6.9 and 10.6 were light brown, greenish gray, blue and dark red. The UV-Vis spectra of gold nanostructures synthesized at pH 5.0, 6.9 and 10.6 show almost identical trends for serine and threonine (figure 4.11). The UV-Vis spectra of pH5.0 show the characteristics of 1-D gold nanostructures showing broad absorption bands to the NIR region. Clear bands could be observed for the gold nanostructures synthesized at pH 6.9 for both serine and threonine which were located near 555nm. Sharp bands located near 525nm were observed for the gold nanostructures synthesized at pH10.6.

Amino acid	pH				
	3.1±0.01	4.1±0.01	5.0±0.02	6.9±0.00	10.6±0.04
G	colorless				
S	colorless				
T	colorless				

Figure 4.10 The photographs of as-synthesized gold nanostructures dispersed in water. The gold nanostructures were synthesized by incubation of 0.5mM $HAuCl_4$ + 0.18mM hydroxyl amino acids at pH 3.1±0.01, 4.1±0.01, 5.0±0.02, 6.9±0.00 and 10.6±0.04 for 3days at 37°C.

SEM and TEM observations of the gold nanostructures synthesized with serine and threonine show more structural changes compare to glycine and the previous functional groups. Nanoplatelet structures were synthesized at pH 3.1 in common for glycine, serine and threonine; however the size of gold nanoplatelets synthesized with threonine were significantly smaller than those of glycine and serine. Unlike the nanokite structures observed for glycine at pH 4.1, the structures synthesized with serine at pH 4.1 were more similar to nanoribbons with irregular morphology whereas structures synthesized with threonine at the same pH were in irregular plate-like structures with random nanowire networks. The nanoribbons synthesized with serine at pH 5.0 were structurally very similar to those observed for glycine; however random gold networks were observed at pH 5.0 for threonine. Highly uniform nanoparticles in shapes and sizes were observed for pH 10.6 with both serine and threonine, and relatively more irregular-shaped

nanoparticles were observed at pH 6.9. Serine and threonine showed significant differences in the synthesized structures especially at pH 4.1 and 5.0 between themselves and also compared to glycine. The region of pH 4.0~5.0 showed more sensitive structural changes to the changes of side chains. Methylene hydroxyl group as a side chain in amino acid resulted in formation of random ribbon-like structures at pH 4.1, and addition of methyl group on the β-carbon of serine resulted very irregular structure formation at pH 4.1 and 5.0. More extensive studies is necessary to understand the role of hydroxyl group on formation of such irregular structures; however it could be assumed that additional hydroxyl group directs crystal growth into more random orientations than other amino acids in the range of pH 4.0~5.0.

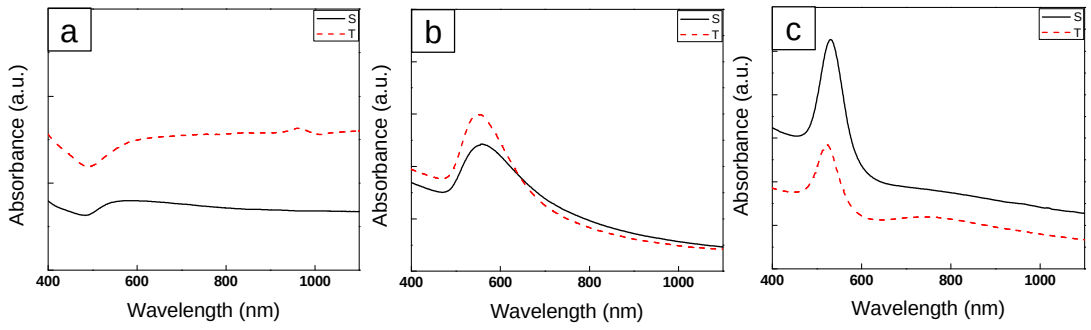

Figure 4.11 UV-Vis spectra of gold nanostructures synthesized at 0.5mM $HAuCl_4$ + 0.18mM hydroxyl amino acids at pH 5.0 (A), 6.9 (B) and 10.6 (C) for 3 days at 37°C.

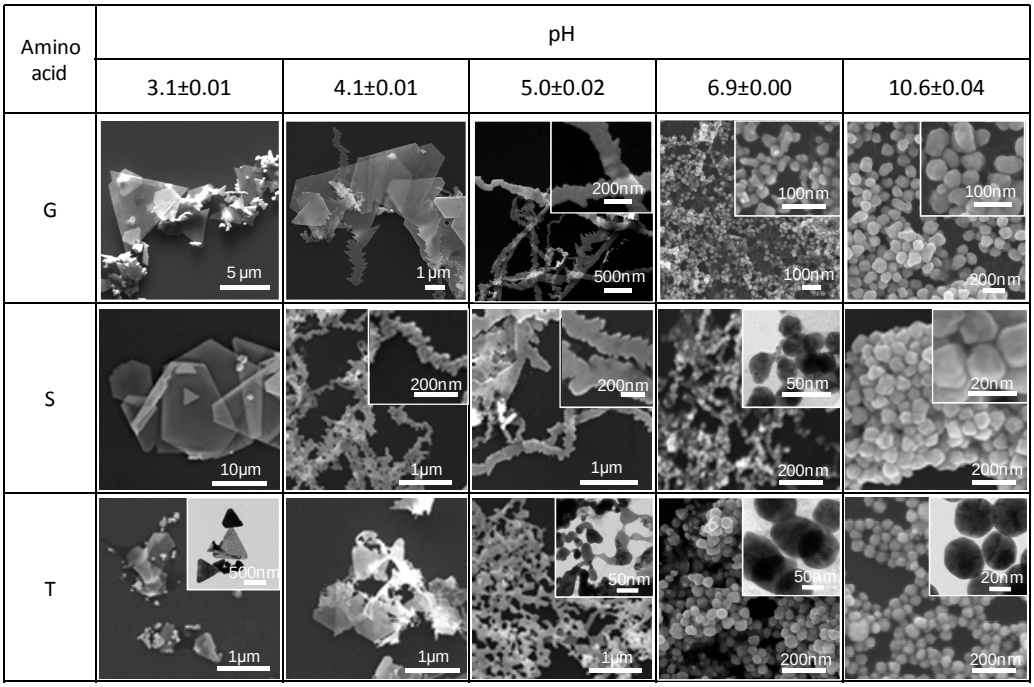

Figure 4.12 Tabulated SEM images and TEM images of gold nanostructures synthesized with 0.18mM hydroxyl amino acids in 0.5mM $HAuCl_4$ at different initial pH for three days at 37°C.

The amount of synthesized gold showed the maximum values in the range of pH 4.0~5.0 similarly to other amino acids, and the ratios of maximum amount of synthesized gold to initial concentration of gold for serine and threonine were 75% and 69%, respectively, at pH 4.8 ascribing more reduction ability of serine and threonine compare to glycine. The amount of synthesized gold decreased around pH 7.0; however increased amount was observed for the pH above 9.5 for both of the hydroxyl amino acids. The reduction behavior of carboxyl and amide groups showed that addition of methyl group between the α-carbon and functional group resulted in decrease of the amount of synthesized gold at the range of pH 4.0~5.0 up to 40%. Threonine showed nearly 6% of difference from the amount of synthesized gold of serine at pH 4.8 which might be

related to the addition of methyl group as a similar trend observed for aliphatic functional group.

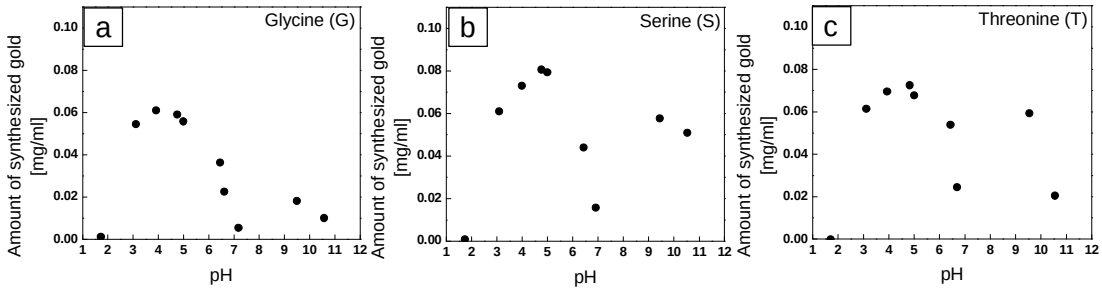

Figure 4.13 The total amount of synthesized gold after three days of incubation carried out with 0.5mM $HAuCl_4$ + 0.18mM hydroxyl amino acids at 37°C for different initial pH.

4.3.1.4. Aromatic Functional Group

As explained in the introduction, the amino acids with aromatic functional groups have larger variations in their chemical structures than those for aliphatic, carboxyl, amide and hydroxyl groups. Reflecting such variations, the colors of the suspensions of gold nanostructures show very distinct differences within the group. The suspension for phenylalanine, which has phenyl group attached on its α-carbon, was colorless with shiny products at pH 3.1, light brown at pH 4.0, light green at pH 5.0, dark blue at pH 6.9 and red at pH 10.5. Suspensions of tryptophan, which has indole group as functional group, show brown color at pH 3.1, brownish gray at pH 4.0, green at pH 5.0, dark blue at pH 6.9 and light pink at pH 10.5. Tyrosine contains phenol group as a side chain and the suspensions of tyrosine were brown at pH 3.1, brownish gray at pH 4.0, dark brown at pH 5.0, dark blue at pH 6.9 and pink at pH 10.5. Such distinctive differences of color

transitions between aromatic amino acids indicate the formation of different structures for each amino acid.

Amino acid	pH				
	3.1±0.06	4.0±0.12	5.0±0.05	6.9±0.07	10.5±0.14
G	colorless				
F	colorless				
W					
Y					

Figure 4.14 The photographs of as-synthesized gold nanostructures dispersed in water. The gold nanostructures were synthesized by incubation of 0.5mM $HAuCl_4$ + 0.18mM aromatic amino acids at pH 3.1±0.06, 4.0±0.12, 5.0±0.05, 6.9±0.07 and 10.5±0.14 for 3days at 37°C.

The UV-Vis spectra of gold nanostructures synthesized using aromatic amino acids also showed large variations for the synthesized structures as expected from the large differences observed for their suspension colors. Anisotropic nanostructures exhibit two surface plasmon resonance (SPR) bands for the short and long axis of the structures, which are known as transverse and longitudinal plasmon band[11]. The transverse plasmon band appears in the range around 520nm and is relatively insensitive to changes in the aspect ratio of the nanostructure, whereas the longitudinal plasmon band appears at

longer wavelengths as the aspect ratio of the nanostructure increases[12,13]. For the UV-Vis spectra of tryptophan at pH 3.1, SPR bands were located as 566, 705 and 990nm. The band located at 566nm might indicate existence of large spherical nanoparticles or a transverse SPR band of anisotropic nanostructures whereas the bands located at 705 and 990 nm might be considered as longitudinal SPR bands for the longer axis of anisotropic nanostructures[14]. Existence of nanostructures with large size distributions or aggregations could be assumed from the broad shape of the bands. The nanostructures synthesized with tyrosine at pH 3.1, showed SPR bands at 574 and 862 and 1005nm which can be also related to the nature of anisotropic nanostructures. Optical characteristics of the structures synthesized with phenylalanine at pH 3.1 were difficult to be analyzed due to low absorbance; however the trend of UV-Vis spectra showing a broad band increasing from 502nm to the NIR region resembles the characteristics of 1-D gold nanostructures, such as nanowires, nanobelts and nanokites[7-10]. The UV-Vis spectrum at pH 4.0 for tryptophan and tyrosine show SPR bands located at 560 and 546nm which might be related to existence of nanoparticles and to a transverse SPR band for anisotropic nanostructures. The UV-Vis spectrum for tryptophan continues to increase to the NIR region which might be due to a longitudinal SPR bands at higher wavelengths than the measurable region. The spectrum of tyrosine decreases after the appearance of a band at 546nm; however the spectrum shows increment after 1000nm which might be an indication of longitudinal SPR bands above 1100nm of wavelength. At pH 5.0, the UV-Vis spectrum for phenylalanine shows a characteristic of 1-D nanostructures which have been observed for many other nanostructures synthesized at the same pH range.

Tryptophan shows broad bands centered at 561 and 747nm indicating existence of anisotropic nanostructures in 1-D and 2-D shapes. Tyrosine shows a clear band at 544nm which implies an existence of nanoparticle structures. The UV-Vis spectra of phenylalanine, tryptophan and tyrosine at pH 6.9 show a broad band located at 600, 546 and 577nm, respectively indicating the nature of irregular and random distributions of nanoparticles. A clear sharp band was observed for the structures synthesized at pH10.5 for phenylalanine and tyrosine at 522nm and 519nm, respectively.

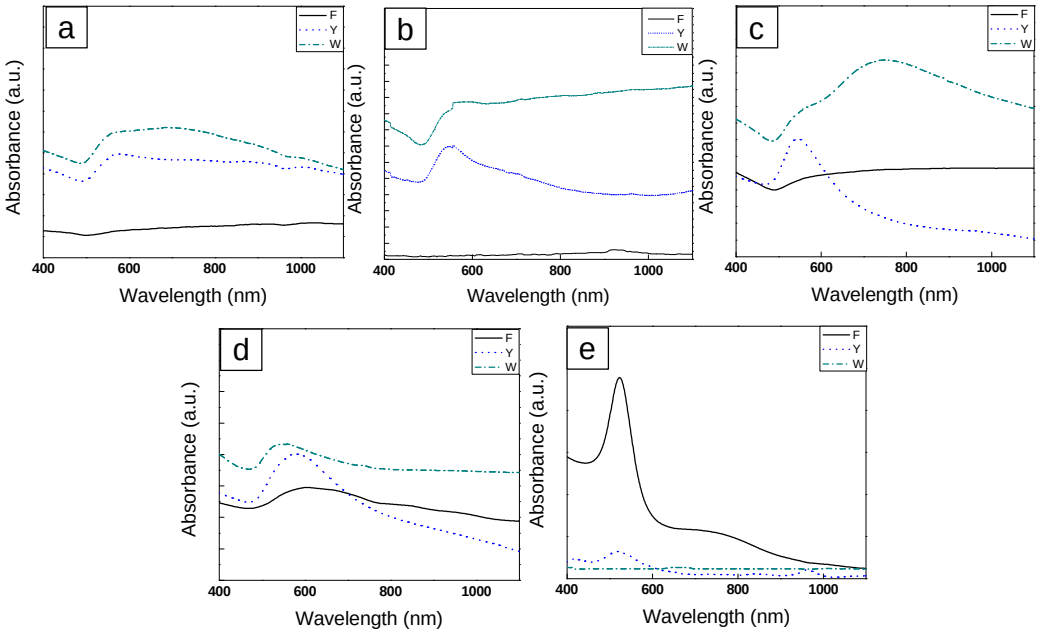

Figure 4.15 UV-Vis spectra of the gold nanostructures synthesized at pH 3.1±0.06 (a), 4.0±0.12 (b), 5.0±0.05 (c), 6.9±0.07 (d) and 10.5±0.14 (e) in 0.5mM $HAuCl_4$ with 0.18mM of each aromatic amino acid for three days at 37°C.

The SEM and TEM images of gold nanostructures synthesized with aromatic amino acids tabulated in figure 4.16 show significant differences from the structures synthesized with glycine. The structures synthesized with phenylalanine show close relations with

glycine for the structures synthesized at pH 3.1, 6.9 and 10.5 which are in the shapes of nanoplatelets, irregular-shaped nanoparticles and mono-dispersed spherical nanoparticles, respectively. Considerable differences could be observed for pH 4.0 and 5.0 where the structures still follow the general shapes of those from glycine forming head-tail structures for pH 4.0 and nanoribbon structures for pH 5.0; however, the detailed insight of the structures show that tadpole structures were synthesized at pH 4.0 and very thin ribbon structures with no indents were observed for phenylalanine. Tryptophan and tyrosine showed irregular-shaped nanoparticles and nanoplatelet structures of which widths were less than 500nm for pH 3.1. Similarly, at pH 4.0, nanoparticles and small nanoplatelets were also observed for tryptophan and tyrosine. Dispersion of such small nanoplatelet structures elucidates the anisotropic characteristics observed with UV-Vis spectrum. Tadpole structures were observed for tryptophan at pH 5.0 whereas spherical and faceted nanoparticles were observed for tyrosine at the same pH. In spite of dramatic differences of synthesized structures at the pH range lower than 5.00, tryptophan and tyrosine show irregular-shaped nanoparticles at pH 6.9 and uniformly distributed spherical nanoparticles at pH 10.5. The observations with SEM and TEM show that the phenyl group as side chain had minor effect on the determination of shapes; however phenol and indole group significantly impacts the structural changes in the range of pH 3.1~5.0.

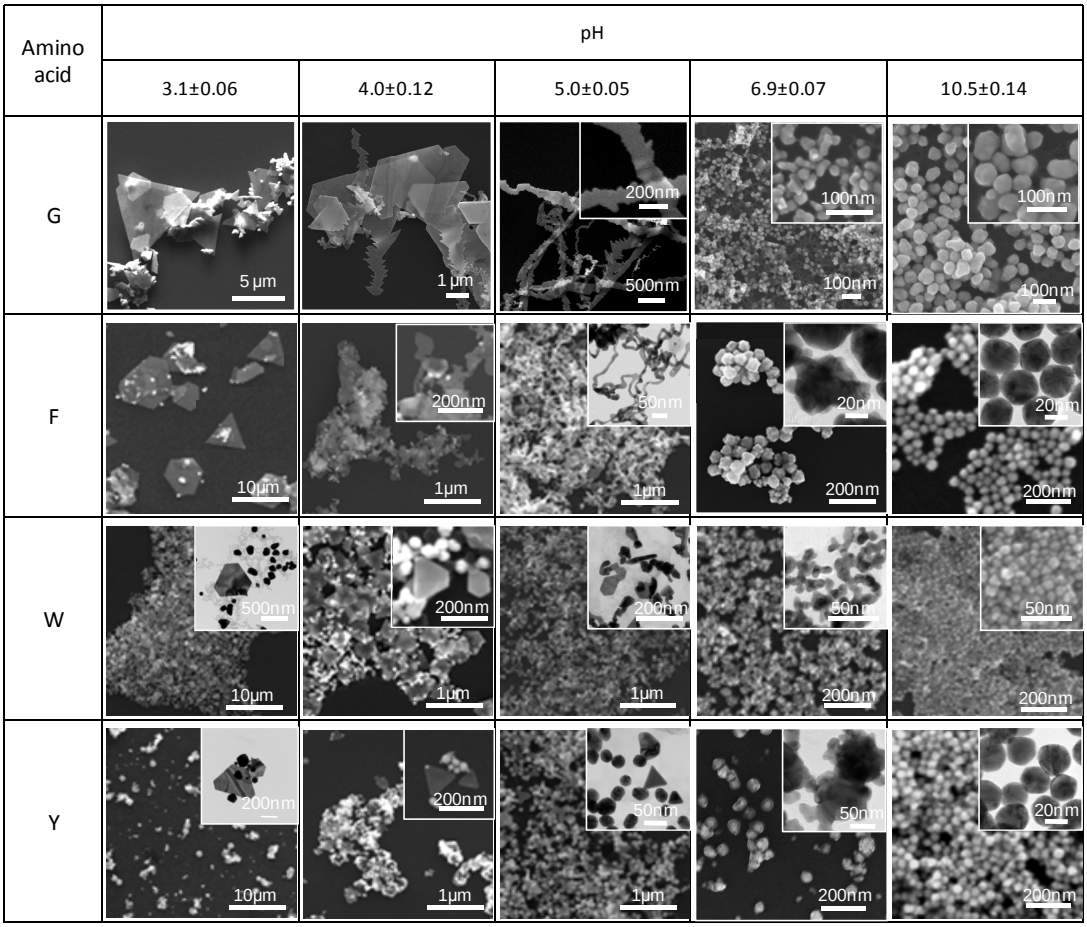

Figure 4.16 Tabulated SEM images and TEM images of gold nanostructures synthesized with 0.18mM aromatic amino acids in 0.5mM $HAuCl_4$ at different initial pH for three days at 37°C.

The general trend of reaching the maximum amount of synthesized gold in the range of pH 4.0~5.0 was observed for aromatic functional group which is similar to previous functional groups (figure 4.17). However dramatic increase of the amount of synthesized gold could be observed for aromatic amino acids, especially, for tryptophan and tyrosine which showed the most distinctive structural changes of synthesized gold nanostructures. The amount of synthesized gold gradually decreased after pH 6.0; however phenylalanine and tyrosine showed large amount of synthesized gold in the range of pH above 9.0

which could be found in the case of aliphatic and hydroxyl functional groups. The ratio of the maximum amount of synthesized gold to initial concentration of gold is 72% for phenylalanine, and 99% for both tryptophan and tyrosine. As assumed for the relation of synthesized structures and the amount of synthesized gold for hydroxyl functional group, such large reduction of gold ions due to amino acids might indicate the role of amino acids more as reducing agent than as capping agent which could reduce the properties of shape-directing crystal formation, thereby result in smaller and more random structures.

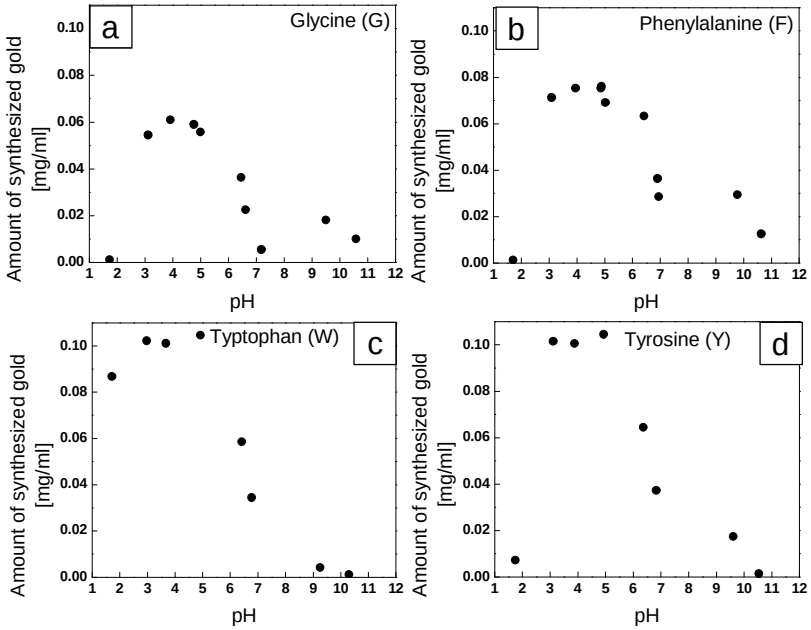

Figure 4. 17 The total amount of synthesized gold after three days of incubation carried out with 0.5mM $HAuCl_4$ + 0.18mM aromatic amino acids at 37°C for different initial pH.

4.3.1.5. Amine Functional Group

Amine functional group is consisted of three amino acids with side chains in different chemical structures which share common properties of polar, hydrophilic and highly

basic. The colors of the suspensions for arginine, lysine and histidine are colorless at pH 3.2 (figure 4.18). Light appearance of brown, green and yellow could be observed for the suspensions of arginine, lysine and histidine at pH 4.4. At pH 5.5, the suspensions for arginine were brown color while suspensions for lysine and histidine showed bluish green and light green, respectively. Initially, the reaction pH was targeted at 7.0; however addition of amine amino acids increased the solution pH significantly due to the high pK_a of amine functional groups and the sensitive pH changes near neutral pH. Thus the suspensions were incubated at final pH of 8.9±0.05. The suspensions for arginine, lysine and histidine showed blue and purple colors at pH 8.9, and the suspensions for pH 10.7 were all transparent.

Amino acid	pH				
	3.2±0.01	4.4±0.03	5.5±0.10	8.9±0.05	10.7±0.01
G	colorless				
R	colorless				
K	colorless				
H	colorless				

Figure 4.18 The photographs of as-synthesized gold nanostructures dispersed in water. The gold nanostructures were synthesized by incubation of 0.5mM $HAuCl_4$ + 0.18mM amine amino acids at pH 3.2±0.01, 4.4±0.03, 5.5±0.10, 8.9±0.05 and 10.7±0.01 for 3days at 37°C.

The UV-Vis spectra of lysine and histidine at pH 5.5 show a characteristic of 1-D and 2-D structures as described previously (figure 4.19). Arginine showed a broad band centered at 404nm which might be a characteristic of wide distributions of nanoparticles. By the shape of the UV-Vis spectrum at pH 8.9, the structures synthesized by each amino acid could be assumed as 1-D nanostructures and irregular-shaped nanoparticles for lysine and histidine, respectively. No optical properties could be measured for arginine at pH 8.0 and arginine, lysine and histidine at pH 10.7.

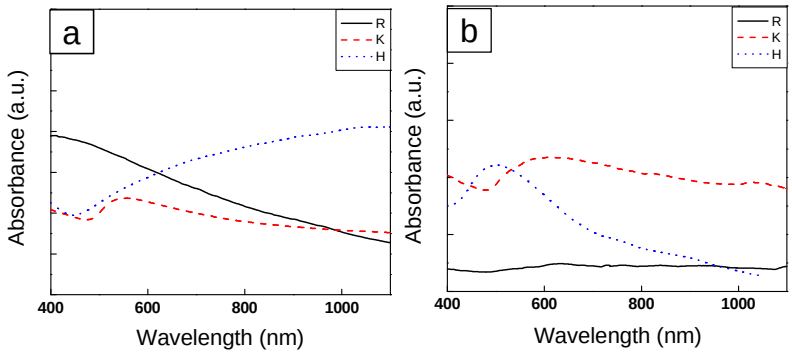

Figure 4.19 UV-Vis spectra of the gold nanostructures synthesized at pH 5.5±0.10 (a), 8.9±0.05 (b), in 0.5mM $HAuCl_4$ with 0.18mM of each aromatic amino acid for three days at 37°C.

Compared to the SEM and TEM images of glycine, the structures synthesized with arginine share no similarities in the range of pH below 5.5 (figure 4.20). Nanoplatelets and ribbon-like networks were observed at pH 3.2, 4.4 and 5.5 for arginine; however the majority of the products for arginine were spherical structures in a few hundreds of nanometers in diameter containing gold nanoparticles with diameters less than 30nm (insets of R at pH 3.3 and 5.5). The structures at pH 8.9 and 10.7 were in similar trends as

glycine, which were irregular-shaped nanoparticles and mono-dispersed nanoparticles. Lysine had a few platelet structures at pH 3.2 and 4.4, but most of the structures were randomly grown irregular platelet structures with nanoparticles. The structures synthesized at pH 5.5 and 8.9 with lysine were in similar anisotropic structures with high structural irregularity. Uniform spherical nanoparticles were observed at pH 10.7 for lysine. Unlike the other amine amino acids, histidine showed formation of small nanoplatelets and nanoparticles at pH 3.2 and 4.4, and serrate nanoribbon structures were observed at pH 5.5. Nanoparticles with irregular shapes were observed at pH 8.9 and relatively more uniform nanoparticles were synthesized at pH 10.7 with histidine. The trend of histidine is close to those observed for aromatic amino acids especially to tryptophan and tyrosine. Lysine showed poor shape-directing properties to synthesize nanoplatelets or nanoribbons, and arginine showed interesting feature of synthesizing spherical structures containing small nanoparticles inside the structures. Previously, a few studies showed the interaction of amino acids with gold nanoparticles, and demonstrated adsorption of amino acids on gold nanoparticles through amine groups[15,16]. Since arginine contains three terminal amine groups, the gold binding properties of arginine might be larger than other amino acids with a single amine group. Moreover, three terminal amine groups are facile to assemble nanoparticles in 3-D[17], and the spherical shape formation might be explained by the thermodynamic stability of spherical structures.

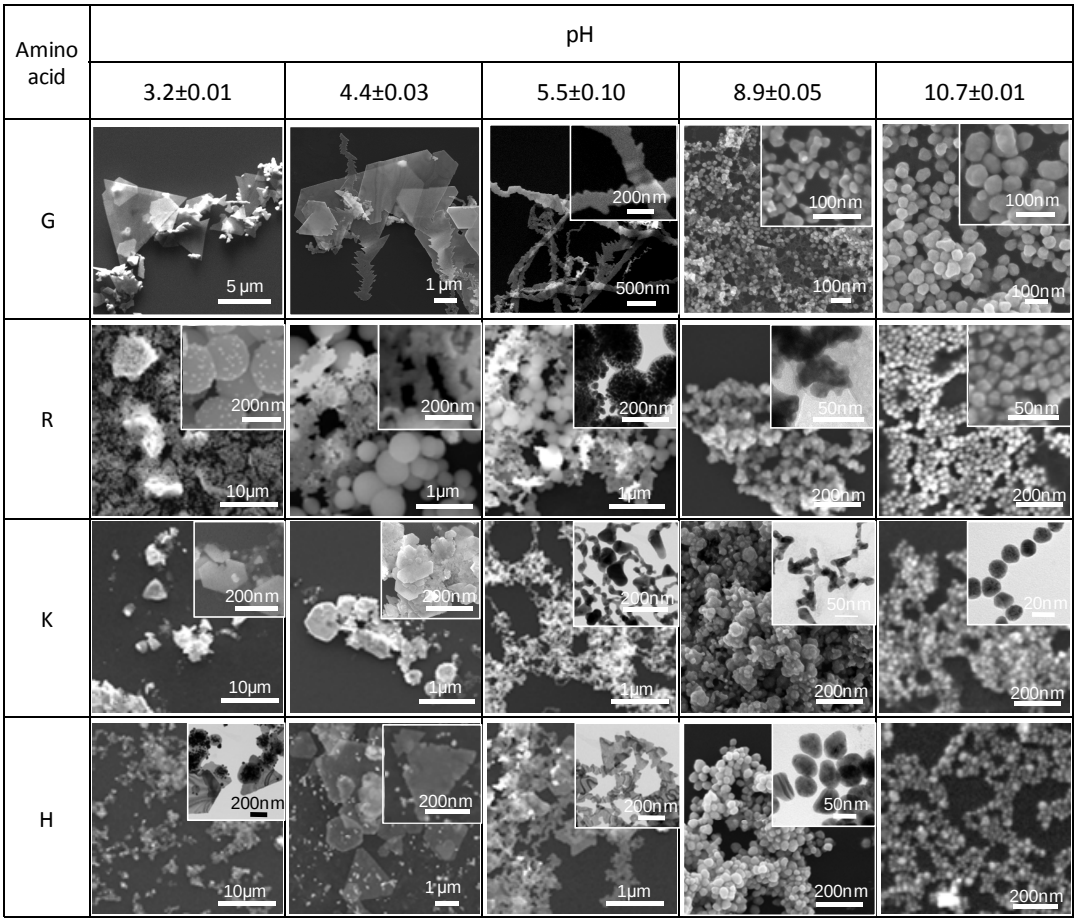

Figure 4.20 Tabulated SEM images and TEM images of gold nanostructures synthesized with 0.18mM amine amino acids in 0.5mM $HAuCl_4$ at different initial pH for three days at 37°C.

The amounts of synthesized gold for amine amino acids were much larger than any other groups of amino acids (figure 4.21). The amount of synthesized gold reached the maximum value in the range near pH 5.0. Compared to the ratio of the amount of synthesized gold to initial concentration of gold of glycine which was 57%, the ratios of

arginine, lysine and histidine are 85, 94 and 99% at pH 5.1, 5.4 and 5.0, respectively. The reduction of gold ions increased up to 42% due to the amine functional groups. The amount of synthesized gold dramatically decreased near pH 9.0 for arginine and lysine, and pH 7.0 for histidine.

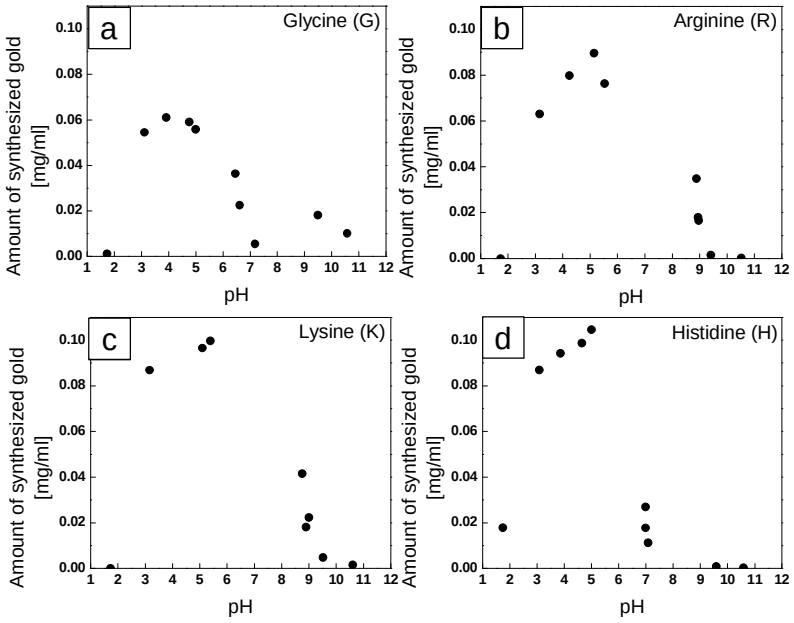

Figure 4.21 The total amount of synthesized gold after three days of incubation carried out with 0.5mM $HAuCl_4$ + 0.18mM amine amino acids at 37°C for different initial pH.

4.3.1.6. Sulfur-containing Functional Group

The colors of suspensions for cysteine were red at pH 3.0, brown colors at pH 3.8 and 4.8, dark red color at pH 6.9 and transparent at pH 10.5 (figure 4.22). For methionine, the colors of the suspensions were colorless with shiny gold products at pH 3.0, light brown at pH 3.8, light green color at 4.8, dark purple at pH 6.9 and light pink at pH 10.5. The

color transitions of cysteine showed significant differences from glycine whereas methionine shows similar colors to the suspensions of glycine.

Amino acid	pH				
	3.0±0.00	3.8±0.11	4.8±0.13	6.9±0.22	10.5±0.08
G	colorless				
C					
M	colorless				

Figure 4.22 The photographs of as-synthesized gold nanostructures dispersed in water. The gold nanostructures were synthesized by incubation of 0.5mM $HAuCl_4$ + 0.18mM sulfur-containing amino acids at pH 3.0±0.00, 3.8±0.11, 4.8±0.13, 6.9±0.22 and 10.5±0.08 for 3days at 37°C.

At pH 3.0, the UV-Vis spectra of nanostructures synthesized with cysteine shows a broad band at 552nm (figure 4.23). A broad band located at 558nm which is in a similar shape as the spectra for pH 3.0 was observed for the gold nanostructures synthesized with cysteine at pH 3.8. Structures synthesized with methionine were unable to analyze due to low intensity of absorbance at pH 3.0 and 3.8. The UV-Vis spectra of cysteine at pH 4.8 show a clean band at 553nm and a broad band centered at 801nm which might be a longitudinal SPR band for an anisotropic structures. Structures synthesized with methionine at pH 4.8 showed SPR bands located at 595 and 963 nm as a transverse and longitudinal SPR bands. At pH 6.9, methionine shows a single band at 531nm which is a clear indication of the existence of spherical nanoparticles, and cysteine shows a

broadening SPR bands at 534nm which might be the optical properties of irregular-shaped or aggregated nanoparticles. The UV-Vis spectra were not observable for the structures synthesized at pH 10.5.

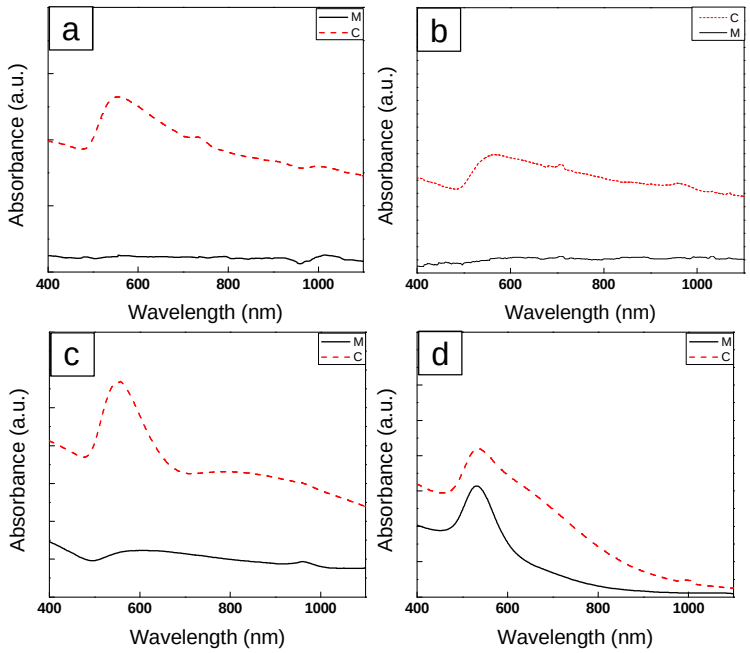

Figure 4.23 UV-Vis spectra of the gold nanostructures synthesized at pH 3.0±0.00 (a), 3.8±0.11 (b), 4.8±0.13 (c), and 6.9±0.22 (d) in 0.5mM $HAuCl_4$ with 0.18mM of each sulfur-containing amino acid for three days at 37°C.

The SEM and TEM images tabulated in figure 4.24 show the distinctive differences of the structures synthesized by cysteine and glycine. Nanoplatelet structures were synthesized by using methionine at pH 3.0 and 3.8, and the sizes of nanoplatelets were observed to be smaller at pH 3.8 than those at pH 3.0. A mixture of nanoparticles and nanokite structures were observed at pH 4.8, and uniform spherical nanoparticles were observed at pH 6.9 and 10.5 for methionine. On the contrary, cysteine showed a formation of faceted nanoparticle structures and spherical nanoparticles at pH 3.0 and 3.8.

Elongated particles structures resembling tadpole structures were observed at pH 4.8 with cysteine, and spherical nanoparticles were synthesized at pH 6.9. Nanoparticles embedded in aggregated organic structure were observed at pH 10.5 using cysteine. Cysteine and methionine contain a thiol group and a thiol ether connected to a methyl group, respectively, as their side chains. Thiol group on cysteine has strong binding properties with gold[18,19], and for the reason, cysteine has been proposed as an effective stabilizer and capping agent for gold nanoparticles[20,21]. Due to such excellent binding properties, cysteine might completely adsorb on the gold nanostructures hindering further growth of the crystal. In fact, Lan and coworkers were able to synthesized serrate nanoribbon structures, which were often observed with glycine and other aliphatic amino acids, with 0.02mM of cysteine[5]. This indicates that smart adjustments of the concentrations of cysteine might lead to synthesizing various kinds of structures that have been demonstrated with other amino acids. On the contrary, methionine behaves like the simple monoamino monocarboxylic acids in a hydroxychloroaurate solution, which differs its properties from cysteine[22]. Thus, structural changes by methionine were not as dramatic as those by cysteine which might be due to no direct interaction of sulfur group with gold. The shape of side chain which affects the shape-directing of crystal growth[15] and the polarizability of the molecules might resulted the structural differences of gold nanostructures synthesized by methionine at pH 3.8 and 4.8 from those of glycine.

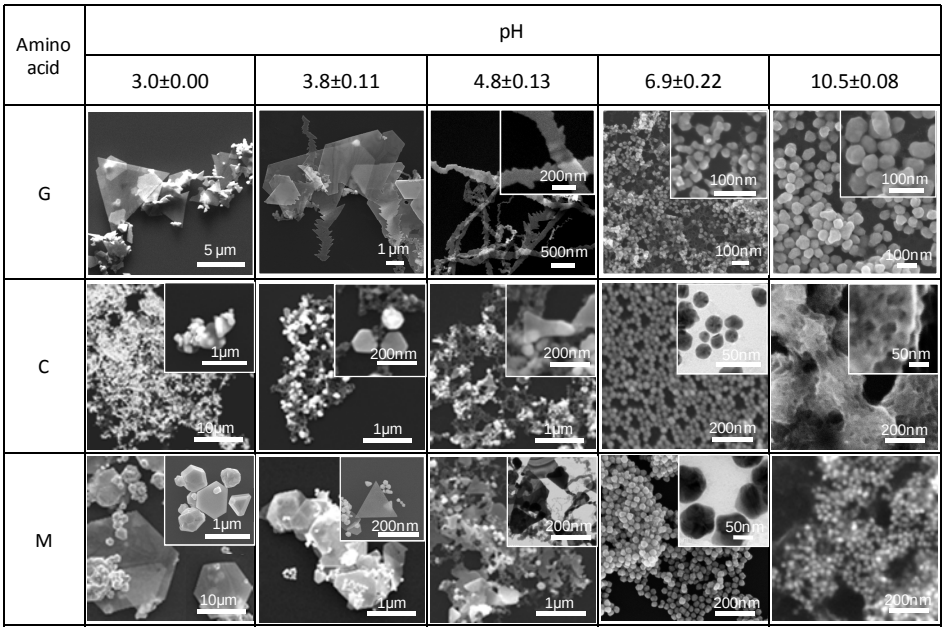

Figure 4.24 Tabulated SEM images and TEM images of gold nanostructures synthesized with 0.18mM sulfur-containing amino acids in 0.5mM $HAuCl_4$ at different initial pH for three days at 37°C.

The maximum amount of synthesized gold shown in figure 4.25 was observed at the pH of 4.7 and 4.9 for cysteine and methionine, respectively. Cysteine and methionine reduced 98% of the gold ions during the synthesis process at pH 4.7 and 4.9 which is 41% higher than that of glycine. In spite of large structural differences of the synthesized structures, the reduction behavior of cysteine and methionine are very similar to each other.

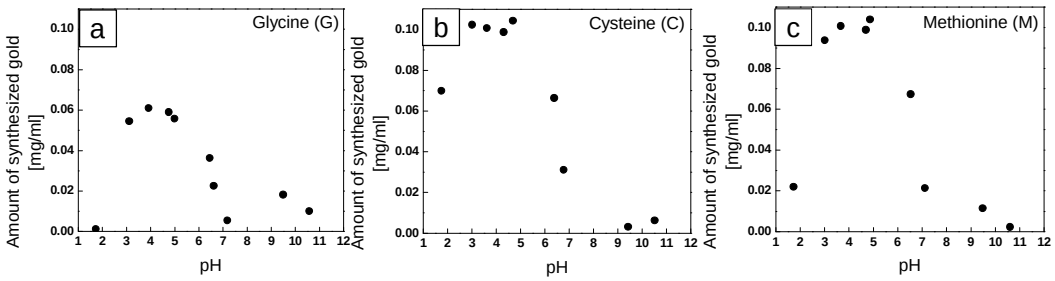

Figure 4.25 The total amount of synthesized gold after three days of incubation carried out with 0.5mM $HAuCl_4$ + 0.18mM sulfur-containing amino acids at 37°C for different initial pH.

4.3.1.7. General Structural, Reductive and Optical Trends

The structural, optical and reductive observations of gold nanostructures, which were synthesized with amino acids containing various side chains, showed that there were considerable changes on the synthesized structures and synthesis processes due to the differences of side chains. The distinctive structural and reductive differences were tabulated in table 4.3. As glycine has been considered as the control material, the structures synthesized with glycine at different ranges of pH were considered as control structures to compare the structural changes due to the side chains of other amino acids.

The structures synthesized in the pH range near 3.0, where $AuCl_4^-$ is predominantly presented, were mostly in nanoplatelet structures irrespective of the sizes. Arginine and lysine which contain amine terminal groups as side chains showed formation of significantly different structures from other amino acids forming spherical and irregular structures in the pH range of 3.0~5.0.

Amino acids in aliphatic, cyclic, carboxyl, amide and hydroxyl groups formed nanoribbon structures in the range of pH 4.0 and 5.0 with variations of the observed thicknesses. However, aromatic, amine and sulfur-containing groups showed the most

structural variations at pH 4.0 and 5.0 compared to glycine. Among aromatic group, phenol and indole group side chains of tryptophan and tyrosine resulted formation of small nanoplatelets at pH 4.0 and tadpole at pH 5.0 in which the structures could be found at pH 3.0 and 4.0 for other amino acids and, similarly, histidine, cysteine and methionine also form nanoplatelets at pH near 4.0. In the studies of glycine-mediated synthesis of gold nanostructures, the formation of nanoplatelets was related to $AuCl_4^-$ complexes. However the formation of nanoplatelets were difficult to be confirm in the range of pH where only $AuCl_4^-$ existed due to the lower reactivity of glycine and $AuCl_4^-$ species at low pH. Interestingly, tryptophan, tyrosine, histidine, cysteine and methionine have considerably higher reduction capability of $AuCl_4^-$ than other amino acids even at $AuCl_4^-$-rich pH region (pH<2) indicating higher reactivity of those amino acids with $AuCl_4^-$ compared to the other amino acids showing nearly zero reduction at the same pH range (figure 4.17, 21, 25).

The gold nanoparticles synthesized in the range of pH 7.0~11.0 showed high similarities for most of the amino acids except cysteine at pH 10.5. Nanoparticles with minor structural variations were observed for all twenty amino acids at pH 7.0 and uniform spherical nanoparticles were synthesized at pH above 10.0. This might indicate that the nanoparticle formation is more related to the hydrolyzed species of gold complexes and basic pH condition rather than to the chemical structures of side chains.

Table 4.3 Tabulated structural and reductive properties of gold nanostructures synthesized using amino acids.

Functional group	Amino acid		Structural resemblence ~pH3.0	~pH4.0	~pH5.0	~pH7.0	~pH10.0	Yield of max. reduction rate (%)	Reduction rate at basic condition
	Glycine	**G**	**Nanoplatelet**	**Nanokite**	**Nanoribbon**	**Irregular nanoparticle**	**Uniform nanoparticle**	**57**	**SI****
Aliphatic	Alanine	A	S*	SD*	S	S	S	51	N**
	Valine	V	S	S	S	S	S	55	I**
	Leucine	L	S	S	S	S	S	49	I
	Isoleucine	I	S	S	S	S	S	52	N
Cyclic	Proline	P	S	S	S	S	S	64	I
Carboxyl	Aspartic acid	D	S	SD	SD	S	S	81	N
	Glutamic acid	E	S	S	S	S	S	59	N
Amide	Asparagine	N	S	SD	SD	S	S	94	N
	Glutamine	Q	S	S	S	S	S	54	N
Hydroxyl	Serine	S	S	SD	S	S	S	75	I
	Threonine	T	SD	SD	SD	S	S	69	I
Aromatic	Phenylalanine	F	S	SD	SD	S	S	72	I
	Tryptophan	W	SD	VD*	VD	S	S	99	SI
	Tyrosine	Y	SD	VD	VD	S	S	99	SI
Amine	Arginine	R	VD	VD	VD	S	S	85	N
	Lysine	K	VD	VD	VD	SD	S	94	N
	Histidine	H	SD	VD	S	S	S	99	N
Sulfur-containing	Cysteine	C	SD	VD	VD	S	VD	98	N
	Methionine	M	S	VD	SD	S	S	98	N

* S: similar, SD: slightly different, VD: very different
** SI: slightly increased, I: increased, N: no increases

The reduction behavior of twenty amino acids commonly shows the maximum amount of synthesized gold in the pH range of 4.7~5.3 in which $Au(OH)_2Cl_2^-$ is predominantly presented. The maximum amount of synthesized gold for aliphatic amino acids show smaller variations compared to the other groups of amino acids. Previously, in the studies on oxidation of amino acids by chloroaurate, the kinetics and mechanism for the reduction of hydroxychloroaurate complexes through complexing with glycine and alanine were demonstrated[23,24]. The reaction rate of alanine with hydroxychloroaurate complexes were slower than it of glycine which might relate to smaller amount of synthesized gold for alanine than glycine for the synthesis of gold nanostructures. Similarly, addition of aliphatic group as a side chain on amino acids could have effects on

the reaction rate of hydroxychloroaurate complexes thereby lower the reduction rate of gold.

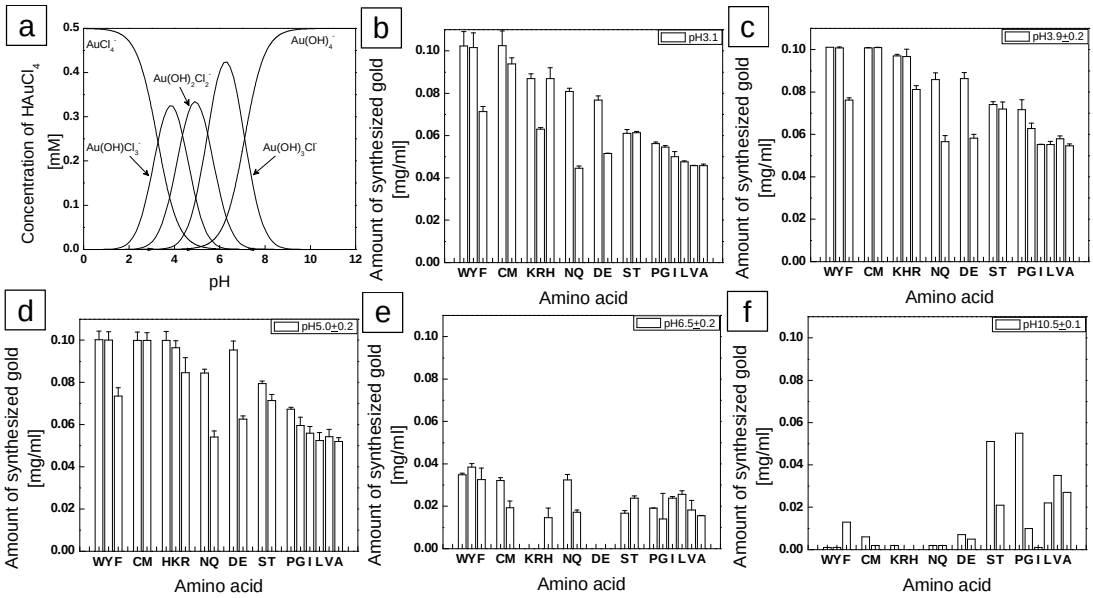

Figure 4.26 Diagram of predominant hydroxychloroaurate complexes with respect to pH in 0.5mM $HAuCl_4$ (a). The amount of synthesized gold of twenty amino acids organized based on the ranges of pH near 3.1 (b), 3.9 (c), 5.0 (d), 6.5 (e) and 10.5 (f).

The amounts of synthesized gold for twenty amino acids are organized by the reaction pH in figure 4.26 with a predominant diagram of hydroxychloroaurate complex in 0.5mM $HAuCl_4$ at 37°C. In general, the amino acids with cyclic, hydroxyl, aromatic, amine and sulfur-containing functional groups showed large amount of synthesized gold; however, only four amino acids hydroxyl amino acids and phenylalanine resembled the structures of glycine in this range of pH. Aspartic acid and asparagine exhibit large numbers for the maximum amount of synthesized gold (pH 4.0~5.0) while sharing high resemblance with the structures synthesized with glycine. The maximum reduction rate of

glutamic acid and glutamine dramatically decreased compared to the aspartic acid and asparagine with the same terminal group as side chain ascribing the suppression of the function of terminal carboxyl and amide groups in glutamic acid and glutamine due to the increased length of carbon chains.

Nearly half of the amino acids showed increased amount of synthesized gold in the range of pH above 9.0. Glycine, tryptophan and tyrosine showed slight increase in basic conditions where as valine, leucine, proline, serine, threonine and phenylalanine showed large increment of the amount of synthesized gold in the same pH range. Such increase in basic conditions can be observed in the amino acids with aromatic rings, cyclic ring and aliphatic chain with methyl terminal groups.

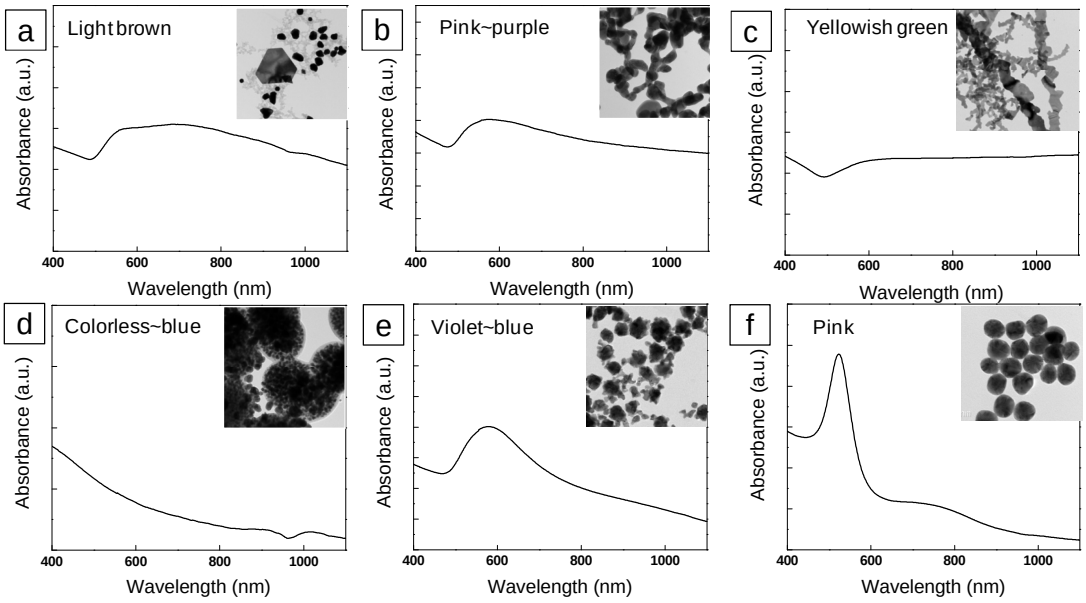

Figure 4.27 The general shapes of UV-Vis spectra for various kinds of gold nanostructures synthesized using amino acids.

The general shapes of UV-Vis spectra of gold nanostructures observed in the range of pH 5.0~ 10.7 are organized in figure 4.27. Mixture of small nanoplatelets and

nanoparticles shows multiple SPR bands in broad ranges of wavelengths as shown in figure 4.27a. The UV-Vis spectra of anisotropic structures like the inset of figure 4.27b present SPR bands between 500~600nm similar to those of non-uniform nanoparticles; however the band is broader than it of nanoparticles and the absorbance at high wavelength region does not decrease as it does for nanoparticles. Nanoribbon shows a transverse band between 500~600nm and a continuous increase of absorbance toward NIR region could be observed which might indicate appearance of longitudinal band in larger wavelength (figure 4.27c). Spherical structures containing small nanoparticles in size of 10~50nm present a SPR band near 400nm and the absorbance continuously decreases as the wavelength increases (figure 4.27d). Nanoparticles in irregular shape or with wide size distribution show a broad band in the range of 520~580nm (figure 4.27e). A sharp band located near 520nm represents the nature of uniform gold nanoparticles (figure 4.27f).

4.3.2 The Effect of Chloride Concentration

The addition of excessive amount of chloride into $HAuCl_4$ solution causes replacements of OH^- in the gold complexes with Cl^-, thereby the numbers of chloride (x) in $Au(OH)_{4-x}Cl_x^-$ increases up to 4 depending on the amount of chloride and the pH of the solution[25]. The effect of the speciation of gold complexes was demonstrated using glycine in chapter3. The shift of speciation of gold complexes toward higher pH region by addition of 0.5M NaCl was theoretically estimated (figure 4.1) and the gold nanostructures synthesized at different pH showed the same structural features with

coincidence of gold complex species. The trend of the amount of synthesized gold measured at wide ranges of pH which revealed the maximum value for $Au(OH)_2Cl_2^-$ also showed a shift to the ranges of higher pH where $Au(OH)_2Cl_2^-$ was predominant. Herein, the changes on the trends of reductive behavior of gold are demonstrated by comparing the amount of synthesized gold by each amino acid at different pH.

The amounts of synthesized gold are plotted for twenty amino acids are organized based on the ranges of pH in figure 4.28. Compared to the predominant diagram in figure 4.27a with no excess amount of chloride, the curves of hydroxychloroaurate complex species are shifted to the direction of higher pH in figure 4.28a. Without addition of excessive chloride in 0.5mM $HAuCl_4$, $AuCl_4^-$ is predominant species in pH 3.0, $Au(OH)Cl_3^-$ in pH 4.0, $Au(OH)_2Cl_2^-$ in pH 5.0, $Au(OH)_3Cl^-$ in pH 6.5 and $Au(OH)_4^-$ in pH above 10. With addition of 0.5M NaCl, the predominant species until pH 5.0 becomes $AuCl_4^-$ and $Au(OH)Cl_3^-$, $Au(OH)_2Cl_2^-$, $Au(OH)_3Cl^-$ and $Au(OH)_4^-$ are predominantly presented at pH 6.0, 7.0, 8.5 and the ranges above 11.0. In figure 4.28c, the amount of synthesized gold is much smaller than those observed in figure 4.27c without addition of 0.5M NaCl indicating the decreased amount of reduction rate due to the shift of speciation. The reactivity of tryptophan, tyrosine, cysteine, methionine and histidine with $AuCl_4^-$ at pH 3.3 are higher than any other amino acids, which is similar to the general reductive trend observed previously. The amounts of synthesized gold for twenty amino acids continued to increase and reached the maximum values at pH 7.4 where $Au(OH)_2Cl_2^-$ existed predominantly. The maximum amount of synthesized gold appeared at the same speciation of hydroxychloroaurate ascribing that the speciation of

hydroxychloroaurate plays more important role to determine the reductive behavior of amino acids than the absolute values of pH.

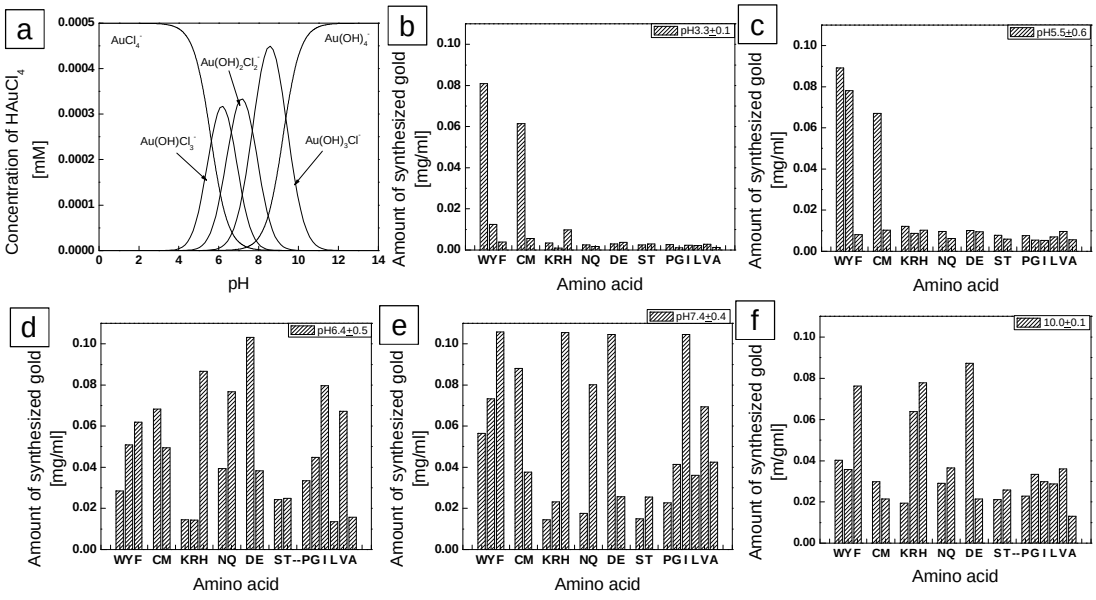

Figure 4.28 Diagram of predominant hydroxychloroaurate complexes with respect to pH in 0.5mM $HAuCl_4$ + 0.5M NaCl (a). The amount of synthesized gold of twenty amino acids organized based on the ranges of pH near 3.3 (b), 5.5 (c), 6.4 (d), 7.4 (e) and 10.0 (f).

4.4 Conclusions

The effects of the side chains of natural amino acids on the synthesis of gold nanostructures were demonstrated by using glycine as a control material which does not contain any side chains. Amino acids in aliphatic and cyclic functional group hardly resulted in significant differences in the characteristics of synthesized gold nanostructures. The colors of suspensions and the UV-Vis spectra of gold nanostructures synthesized with aliphatic and cyclic amino acids showed similar properties with minute variations. Carboxyl and amide amino acids formed gold nanostructures which were structurally similar to those synthesized with glycine; however the maximum amount of synthesized gold for aspartic acid and asparagine at pH 5.0 was approximately 24~37% higher than it for glycine. Hydroxyl amino acids also formed gold nanostructures similar to the products of glycine with small structural variations and showed 12~18% higher values for the maximum amount of synthesized gold compared to glycine. Aromatic, amine and sulfur-containing group formed gold nanostructures with the largest structural differences and maximum amount of synthesized gold.

The reason for structural variations on the formation of gold nanostructures has not been clearly demonstrated; however, the results of structural and optical characterization show that the gold nanostructures synthesized at pH 3.0 are dominantly nanoplatelets and nanoparticles are synthesized irrespective of the kind of amino acids at the ranges of pH above 6.5. The structural changes due to the differences of side chains are sensitively observed in the pH range of 4.0~5.0 where the maximum amount of synthesized gold can be observed for all of the amino acids. Such sensitive changes might be due to the

changes in chemical structures in the side chains resulting in different shape-directing properties for crystal growth.

The effect of chloride concentration on the reductive behavior of hydroxychloroaurate by amino acids was demonstrated to correlate the speciation of hydroxychloroaurate to the amount of synthesized gold by amino acids. The results showed that the maximum amount of synthesized gold appears in the region of predominant $Au(OH)_2Cl_2^-$ species irrespective of the absolute pH values.

4.5 References

(1) Shao, Y.; Jin, Y.; Dong, S. *Chemical Communications* **2004**, 1104-1105.
(2) Tan, Y. N.; Lee, J. Y.; Wang, D. I. C. *The Journal of Physical Chemistry C* **2008**, *112*, 5463-5470.
(3) Bhargava, S. K.; Booth, J. M.; Agrawal, S.; Coloe, P.; Kar, G. *Langmuir* **2005**, *21*, 5949-5956.
(4) Mandal, S.; Selvakannan, P.; Phadtare, S.; Pasricha, R.; Sastry, M. *Journal of Chemical Sciences* **2002**, *114*, 513-520.
(5) Huang, L.; Zhang, Y.; Guo, Z.; Gu, N. *Chinese Science Bulletin* **2009**, *54*, 1626-1629.
(6) Nechayev, Y. A.; Nikolenko, G. V. *Geochemistry International* **1986**, *23*, 32-37.
(7) Lim, B.; Camargo, P. H. C.; Xia, Y. *Langmuir* **2008**, *24*, 10437-10442.
(8) Swami, A.; Kumar, A.; Selvakannan, P. R.; Mandal, S.; Pasricha, R.; Sastry, M. *Chemistry of Materials* **2003**, *15*, 17-19.
(9) Zhao, N.; Wei, Y.; Sun, N.; Chen, Q.; Bai, J.; Zhou, L.; Qin, Y.; Li, M.; Qi, L. *Langmuir* **2008**, *24*, 991-998.
(10) Pei, L. H.; Mori, K.; Adachi, M. *Langmuir* **2004**, *20*, 7837-7843.
(11) Murphy, C. J.; San, T. K.; Gole, A. M.; Orendorff, C. J.; Gao, J. X.; Gou, L.; Hunyadi, S. E.; Li, T. *Journal of Physical Chemistry B* **2005**, *109*, 13857-13870.
(12) Huang, X.; El-Sayed, I. H.; Qian, W.; El-Sayed, M. A. *Journal of the American Chemical Society* **2006**, *128*, 2115-2120.
(13) Nikoobakht, B.; El-Sayed, M. A. *Chemistry of Materials* **2003**, *15*, 1957-1962.
(14) Kan, C.; Wang, G.; Zhu, X.; Li, C.; Cao, B. *Applied Physics Letters* **2006**, *88*, 071904-3.
(15) Polavarapu, L.; Xu, Q.-H. *Nanotechnology* **2008**, *19*, 075601.
(16) Wangoo, N.; Bhasin, K. K.; Mehta, S. K.; Suri, C. R. *Journal of Colloid and Interface Science* **2008**, *323*, 247-254.
(17) Barbu-Tudoran, L.; Tomoaia, G.; Horovitz, O.; Mocanu, A.; Tomoaia-Cotisel, M., 2008; p 2293-2297.
(18) Kuhnle, A.; Linderoth, T. R.; Hammer, B.; Molina, L. M.; Schunack, M.; Besenbacher, F., 2003; p 553-COLL.
(19) Li, Q. W.; Gao, H.; Wang, Y. M.; Luo, G. A.; Ma, J. *Electroanalysis* **2001**, *13*, 1342-1346.
(20) Sarangi, S. N.; Hussain, A. M. P.; Sahu, S. N. *Applied Physics Letters* **2009**, *95*, 073109 (3 pp.)-073109 (3 pp.).
(21) Petean, I.; Tomoaia, G.; Horovitz, O.; Mocanu, A.; Tomoaia-Cotisel, M., 2008; p 2289-2292.
(22) Farooq, O.; Ahmad, N. *Journal of Electroanalytical Chemistry* **1974**, *53*, 457-460.
(23) Zou, J.; Guo, Z. J.; Parkinson, J. A.; Chen, Y.; Sadler, P. J. *Chemical Communications* **1999**, 1359-1360.
(24) Sen, P. K.; Gani, N.; Midya, J. K.; Pal, B. *International Journal of Chemical Kinetics* **2009**, *41*, 473-482.

(25) Murphy, P. J.; LaGrange, M. S. *Geochimica Et Cosmochimica Acta* **1998**, *62*, 3515-3526.

Chapter 5: Conclusions and Future Outlook

5.1 Conclusions

This thesis has been made with an effort to contribute to envision 1) fabrication processes of nanodevices with automatically assembled nano-scaled circuit components of electrically improved properties and 2) green synthetic processes of nanostructures which surpass conventional processes in structural controllability by taking biological routes. Selective nature of complementary DNA has directed self-assembly of multi-segmented nanowires across two electrodes without any physical assistance. Electrical properties of assembled nanowires showed ohmic contact indicating negligible current blockage effects by the layers of DNA. The gas sensing properties of multi-segmented nanowires demonstrates the stability of DNA-assisted assembled nanowires as an electrical and functional component in nanodevices.

Amino acids showed comparable reducing and capping ability to conventional reducing and capping agents forming various nanostructures of nanoplatelets, nanokites, nanoribbons and nanoparticles. The effect of the speciation of gold complex as a consequence of changes in pH, excessive amounts of chloride, and concentration of $HAuCl_4$ on the structural architectures was demonstrated in a bio-synthetic process using glycine. Gold nanoplatelets were synthesized in the solvent condition where $AuCl_4^-$ was predominant, and nanokites and nanoribbons were synthesized in the solvent of predominant species for $Au(OH)Cl_3^-$ and $Au(OH)_2Cl_2^-$, respectively. Gold nanoparticles were synthesized in the solutions of predominant $Au(OH)_3Cl^-$ and $Au(OH)_4^-$. Similar trends were observed for the synthesis process using the other

amino acids with different functional group as side chains. Overall, the structural changes were more sensitive toward the changes of pH than the differences of chemical structures of side chains indicating dominant role of gold complex speciation for the shape determination of gold nanostructures. A few exceptions of amino acids containing amine, aromatic and sulfur-containing functional groups as side chains were observed showing the significant effect of amine, aromatic and thiol groups on the synthesis process. Reduction behavior of gold complexes by amino acids showed general trends of reaching the highest amount of synthesized gold in the region of predominant $Au(OH)Cl_3^-$ and $Au(OH)_2Cl_2^-$ species, and it gradually decreased as the gold complexes were more hydrolyzed. Additional side chains increased the reduction rate of gold in general except the case of aliphatic functional groups.

Gold nanoplatelets, nanokites and nanoribbons synthesized with amino acids were single crystalline grown along (111) plane. Electron transport properties of single crystalline nanoribbons showed significant decrease of resistivity which was lower by an order of magnitude than polycrystalline counterparts. Gold nanoparticles array aligned in AC electric field presented non-metallic behavior for temperature coefficient of resistivity showing 2.49eV of activation energy. Rapid reversible room temperature H_2S gas sensing properties were demonstrated using AC aligned gold nanoparticle arrays which are more favorable to lower concentration detections.

5.2 Future Outlook

For actual application of DNA-assisted assembly to automatic self-assembly of nano-components in electronic circuits, there are still large numbers of obstacles to overcome for achieving high spatial precision. Spatially controlled functionalization of ssDNA on a

substrate to direct limited numbers of nanowires onto the desired sites, and control of directionality of assembled nanowires are important to truly leave the assembly process to the nature of biorecognition. Soft lithography and dip-pen nanolithography to pattern a substrate with ssDNA might be useful techniques for spatial control of assembled nanowires. Assistance of magnetic field or electric field might improve the directionality of assembled nanowires while maintaining the selective attachment of nanowires on the surface with complementary DNA.

Green processes might be dominant in many industries in the near future for rapid growth of environmental concerns and tremendous amount of developments going on for green processes. Amino acid-mediated synthesis shows the potentials of biological materials for creating various kinds of gold nanostructures without physical and chemical assistance. The mystique of shape control for gold nanostructures was dominantly on the speciation of gold complexes rather than on the unique properties of each amino acid. This encourages exploring new materials for biological synthesis with careful understandings on the solvent system.

Significantly low resistivity of single crystalline gold compared to polycrystalline counterpart showed that electron scattering on the grain boundaries are the major contribution to increase resistivity of metals in nanometer scale. Use of single crystalline gold nanostructures in integrated circuits will dramatically lower the required applied potentials for electronic devices which is one of the major challenges the current technology has faced. In vision of advanced fabrication processes to create single

crystalline nanostructures on circuits, it will be a worth venture to grow single crystalline nanostructures using amino acid containing metal solvent similarly to the principle of electroless deposition.